

Virginia Commonwealth University
VCU Scholars Compass

Theses and Dissertations | Graduate School

2018

Elucidation of Substrate Binding Interactions for Human Organic Cation Transporters 1 (SLC22A1) and 2 (SLC22A2) Using In Silico Homology Modeling in Conjunction with In Vitro Site-Directed Mutagenesis and Kinetic Analysis

Raymond E. Lai
Virginia Commonwealth University

Follow this and additional works at: https://scholarscompass.vcu.edu/etd

 Part of the Medicinal and Pharmaceutical Chemistry Commons, Other Pharmacy and Pharmaceutical Sciences Commons, and the Pharmaceutics and Drug Design Commons

© The Author

Downloaded from
https://scholarscompass.vcu.edu/etd/5593

This Dissertation is brought to you for free and open access by the Graduate School at VCU Scholars Compass. It has been accepted for inclusion in Theses and Dissertations by an authorized administrator of VCU Scholars Compass. For more information, please contact libcompass@vcu.edu.

© Raymond Lai, 2018
All Rights Reserved

ELUCIDATION OF SUBSTRATE BINDING INTERACTIONS FOR HUMAN ORGANIC CATION TRANSPORTERS 1 (SLC22A1) AND 2 (SLC22A2) USING IN SILICO HOMOLOGY MODELING IN CONJUNCTION WITH IN VITRO SITE-DIRECTED MUTAGENESIS AND KINETIC ANALYSIS

A Dissertation submitted in partial fulfillment of the requirements for the degree of

Doctor of Philosophy at Virginia Commonwealth University

by

Raymond Eugene Lai

Bachelor of Science, College of William and Mary, Williamsburg, Virginia, USA

Master of Science, Virginia Commonwealth University, Richmond, Virginia, USA

Doctor of Pharmacy; Virginia Commonwealth University, Richmond, Virginia, USA

Director: Douglas H. Sweet, Ph.D.

Professor, Chair

Department of Pharmaceutics, School of Pharmacy

Virginia Commonwealth University

Richmond, Virginia

August, 2018

ACKNOWLEDGMENTS

My long and arduous academic journey toward the completion of my dissertation project and ultimately the achievement of my PhD would not have come to fruition without the support, guidance, and encouragement from a number of incredible people.

First and foremost, I would like to thank my research advisor, Dr. Douglas Sweet, for instilling into me not only the knowledge of conducting cutting-edge pharmaceutical research, but also the confidence in me as I a grew as a scientist during my time working in his lab. His unwavering passion for research, teaching, and service at VCU is nothing short of inspiring. He provided me the opportunity, resources, and unparalleled guidance in steering me toward success as I navigated through numerous hurdles while completing my research.

A significant amount of praise also goes out to my dissertation committee members, Dr. Keith Ellis, Dr. Phillip Gerk, Dr. Adam VanWert, and Dr. Jürgen Venitz, for offering their time and effort in helping me complete my project as well as challenging me to think critically. Much thanks should also be given to Dr. Philip Mosier of the Department of Medicinal Chemistry for his major contributions in teaching and guiding me through the computationally intensive molecular modeling work that played an integral role in my research. I would also like to acknowledge Dr. MaryPeace McRae and Dr. Frances White for their generosity in lending their fluorescent and confocal microscopes to help us with our cell imaging studies.

Additionally, I would like to recognize all the VCU School of Pharmacy faculty for their efforts teaching and coordinating the challenging courses that I endured and completed as part of the graduate curriculum. Much thanks should also be offered to the administrative staff, especially Keyetta Tate, Laura Georgiadis, and Shakim Craft, for their tireless commitment and attention to detail that have resulted in a smoothly run department.

A big thank you goes out to all my fellow lab colleagues, Dr. Aditi Mulgaonkar, Dr. Li Wang, Dr. Christine Farthing, Dr. Xiaolei Pan, Dr. Hebing Liu, and Christopher Jay, all of whom have been extremely supportive and helpful during my time at VCU.

I would finally like to express my infinite gratitude to all my friends, family, and loving wife, Caroline, who have offered me continuous support, faith, and love through the course of everything I have been able to accomplish.

TABLE OF CONTENTS

ACKNOWLEDGMENTS..... ii

TABLE OF CONTENTS..... iii

LIST OF TABLES..... vi

LIST OF FIGURES.....viii

ABBREVIATIONS..... x

ABSTRACT..... xiv

CHAPTERS

1. OVERVIEW OF EXPRESSION AND FUNCTION OF ORGANIC CATION AND ANION TRANSPORTERS.....1

1.A SOLUTE CARRIER 22 TRANSPORTER FAMILY.....1

1.B MAJOR ORGANIC CATION AND ANION TRANSPORTERS.....8

1.C CURRENT SCOPE OF MOLECULAR MODELING.....20

2. RESEARCH OBJECTIVES AND SPECIFIC AIMS.....30

2.A RESEARCH OBJECTIVES AND HYPOTHESIS.....30

2.B SPECIFIC AIMS TO ADDRESS HYPOTHESIS.....30

3. IDENTIFYING STRUCTURE ELEMENTS OF HUMAN ORGANIC CATION TRANSPORTER 2 (SC22A2) MEDIATING SUBSTRATE TRANSPORTER INTERACTIONS.....33

3.A INTRODUCTION 33

3.B MATERIAL AND METHODS.....36

3.B.1 Chemicals and reagents.....36

3.B.2 Homology modeling and docking studies..... 37

3.B.3 Bacterial transformation.....40

3.B.4 Point mutation of plasmid DNA…… 40

3.B.5 Cell line transfection and maintenance……... 44

3.B.6 Cell accumulation assays ……..44

3.B.7 Genomic DNA integration confirmation…..……...46

3.B.8 Cell harvest for immunoblotting…… 46

3.B.9 SDS-PAGE and Immunoblotting…….. 47

3.B.10 Immunocytochemistry……...48

3.B.11 Green fluorescent protein (GFP) plasmid construction……48

3.B.12 Microscopic imaging……...49

3.B.13 Statistics……..49

3.C RESULTS…… 50

3.C.1 Identification of a hOCT2 model…… 50

3.C.2 Identifying amino acid residues important for MPP^+ hOCT2 interaction…… 56

3.C.3 Substitution of hOCT2 amino acid residues in putative binding pocket……...62

3.C.4 Critical amino acid confirmation through kinetic assays…… 69

3.C.5 Genomic integration of non-functional hOCT2 mutant constructs...73

3.C.6 Immunodetection of non-functional hOCT2 mutants…….. 73

3.C.7 Membrane targeting of hOCT2-GFP fusion construct……..…… 74

3.D DISCUSSION…….. 81

4. IDENTIFYING STRUCTURAL ELEMENTS OF HUMAN ORGANIC CATION TRANSPORTER 1 (SLC22A1) MEDIATING SUBSTRATE-TRANSPORTER INTERACTIONS…… 88

4.A INTRODUCTION……88

4.B MATERIAL AND METHODS…… 92

4.B.1 Chemicals and reagents…… 92

4.B.2 Homology modeling and docking studies……92

4.B.3 Bacterial transformation…….. 95

4.B.4 Point mutation of plasmid DNA……..95

4.B.5 Cell line transfection and maintenance.……99

4.B.6 Cell accumulation assays……... 99

4.B.7 Genomic DNA integration confirmation……..… 101

4.B. 8 Green Fluorescent Protein (GFP) plasmid construction…….101

4.B.9 Microscopic imaging…… 102

4.B.10 Statistics…… 102

4.C RESULTS…….. 103

4.C.1 Identification of a hOCT1 model……..103

4.C.2 Identifying amino acid residues important for MPP^+ hOCT1 interaction…….. 109

4.C.3 Substitution of hOCT1 amino acid residues in putative binding pocket…… 116

4.C.4 Critical amino acid confirmation through kinetic assays……..123

4.C.5 Genomic integration of non-functional hOCT1 mutant constructs. 127

4.C.6 Membrane targeting of hOCT1-GFP fusion construct.…… 127

4.D. DISCUSSION……... 132

5. COMPARISON OF SUBSTRATE BINDING INTERACTIONS BETWEEN HUMAN ORGANIC CATION TRANSPORTERS 1, 2, AND 3…….. 139

LITERATURE CITED…….. 148

VITA…… 162

LIST OF TABLES

Table 1.1 Example compound interactions associated with SLC22 transporters…… 12

Table 1.2 Clinical concentrations of example compounds…….. 15

Table 1.3 Absolute native tissue protein expression levels for human SLC22 transporters…… 17

Table 1.4. Summary of the SLC family homology model template recommendations…24

Table 1.5 Summary of critical residues discovered through initial OCT modeling studies…….. 27

Table 3.1 Primers for hOCT2 site directed mutagenesis…… 42

Table 3.2 Summary of hOCT2 model evaluation scores…….. 53

Table 3.3 hOCT2 docking interaction summary…… 59

Table 3.4 Summary of hOCT2 residue substitutions…… 65

Table 3.5 hOCT2-MPP^+ interaction based conservative substitutions……... 66

Table 3.6 hOCT2-MPP^+ interaction based non-conservative substitutions……... 67

Table 3.7 Summary of K_m estimates for hOCT2 constructs…… 72

Table 4.1 Primers for hOCT1 site directed mutagenesis…… 97

Table 4.2 Summary of hOCT1 mutant evaluation scores……..106

Table 4.3 hOCT1 docking interaction summary……...112

Table 4.4 Summary of hOCT1 residue substitutions……..119

Table 4.5 hOCT1 MPP^+ interaction based conservative substitutions…… 120

Table 4.6 hOCT1-MPP^+ interaction based non-conservative substitutions…… 121

Table 4.7 Summary of K_m estimates for hOCT1 constructs……..126

Table 5.1 hOCT1 substrate docking summary…… 143

Table 5.2 hOCT2 substrate docking summary…… 144

Table 5.3 hOCT3 substrate docking summary…… 145

LIST OF FIGURES

Figure 1.1 Prominent human SLC22 family members expressed in intestine, kidney, and liver……..4

Figure 1.2 Predicted secondary structure of SLC22 transporters……5

Figure 1.3 Model depicting driving forces for SLC22 family members……6

Figure 3.1 Chemical structures of compounds docked into hOCT2 homology models.. 39

Figure 3.2 Sequence alignment of PiPT and hOCT2……... 52

Figure 3.3 hOCT2 homology model…… 54

Figure 3.4 Ramachandran plot for hOCT2 homology model…….. 55

Figure 3.5 3-D rendering of putative binding pocket of hOCT2 with docked MPP^+…….57

Figure 3.6 Structure of hOCT2 with MPP^+ docked……58

Figure 3.7 Known hOCT2 substrates docked into hOCT2 homology model…… 61

Figure 3.8 pcDNA3/hOCT2 vector map……..63

Figure 3.9 Suggested guidance for amino acid residue conservative substitution……..64

Figure 3.10 Representative sequencing chromatogram for hOCT2 mutants…..……..68

Figure 3.11 Functional screen of CHO-hOCT2 wild type and mutant expressing cell lines…….. 70

Figure 3.12 Representative dose response curves for wild type and mutant hOCT2….71

Figure 3.13 PCR analysis of genomic DNA isolated from hOCT2 cell lines……75

Figure 3.14 Western blot of CHO cell lysates probing for hOCT2…… 76

Figure 3.15 Immunocytochemistry of CHO-hOCT2……..77

Figure 3.16 pEGFP-C1/hOCT2 fusion protein vector map……..……... 78

Figure 3.17 Expression patterns of pEGFP-C1/hOCT2……...79

Figure 3.18 Expression of pEGFP-C3/rOct2 in MDCK cells…… 80

Figure 4.1 Chemical structures of compounds docked into hOCT1 homology models.. 94

Figure 4.2 Sequence alignment of PiPT and hOCT1…….. 105

Figure 4.3 hOCT1 homology model…….. 107

Figure 4.4 Ramachandran plot for hOCT1 homology model…… 108

Figure 4.5 3-D rendering of putative binding pocket of hOCT1 with docked MPP^+….. 110

Figure 4.6 Structure of hOCT1 with MPP^+ docked…….. 111

Figure 4.7 Known hOCT1 substrates docked into hOCT1 homology model……..115

Figure 4.8 pcDNA3/hOCT1 vector map…… 117

Figure 4.9 Suggested guidance for amino acid residue conservative substitution…… 118

Figure 4.10 Representative sequencing chromatogram for hOCT1 mutants……..…… 122

Figure 4.11 Functional screen of CHO-hOCT1 wild type and mutant expressing cell lines…… 124

Figure 4.12 Representative dose response curves for wild type and mutant hOCT1.. 125

Figure 4.13 PCR analysis of genomic DNA isolated from hOCT1 cell lines…….. 128

Figure 4.14 pEGFP-C1/hOCT1 GFP fusion vector map……..…. 129

Figure 4.15 Expression patterns of pEGFP-C1/hOCT1……. 130

Figure 4.16 Expression of pEGFP-C3/rOct2 in MDCK cells……... 131

ABBREVIATIONS

2-D	2-dimensional
3-D	3-dimensional
5-HT	Serotonin
AdiC	Amino acid antiporter
ANOVA	Analysis of variance
AP	Alkaline phosphatase
$ASBT_{NM}$	Apical sodium-dependent bile acid transporter
AUC	Area under the curve
ATPase	Adenosine 5'-triphosphatase
BLAST	Basic local alignment search tool
BSA	Bovine serum albumin
cDNA	Complementary DNA
CHO	Chinese hamster ovary
C_{max}	Maximum plasma concentration
CNS	Central nervous system
DAPI	4’,6-diamidino-2-phenylindol
DDI	Drug-drug interaction
DMEM/F12	Dulbecco's Modified Eagle's Medium/F12
DNA	Deoxyribonucleic acid
DOPE	Discrete optimized protein energy
E. coli	Escherichia coli

EDTA	Ethylene-diamine-tetra-acetic acid
EMA	European Medicines Agency
EV	Empty vector
FBS	Fetal bovine serum
FDA	Food and Drug Administration
FITC	Fluorescein isothiocyanate
G418	Geneticin
GlpT	Glycerol-3-phosphate transporter
GOLD	Genetic optimized ligand docking
GFP	Green fluorescent protein
H-bond	Hydrogen bond
HCl	Hydrochloride acid
HEK	Human embryonic kidney 293
HEPES	4-(2-hydroxyethyl)-1-piperazineethanesulfonic acid
IC_{50}	Half maximal inhibition concentration
IgG	Immunoglobulin G
kD	Kilodalton
K_i	Inhibitor constant
K_m	Michaelis-Menten constant
LacY	Lactose permease
LB	Luria broth
MATE	Multidrug and toxic compound extrusion transporter
MDCK	Madin-Darby canine kidney

MFS	Major facilitator superfamily
MPP^+	1-methyl-4-phenylpyridinium
mRNA	Messenger RNA
NaCl	Sodium chloride
NaOH	Sodium hydroxide
NBT/BCIP	Nitroblue tetrazolium/5-bromo-4-chloro-3-indolyl phosphate
NMR	Nuclear magnetic resonance
NorM	Bacterial multidrug and toxic compound extrusion transporter
OAT	Organic anion transporter
OCT	Organic cation transporter
OCTN	Novel organic cation transporter
PAGE	Polyacrylamide gel electrophoresis
PC	Phase contrast
PCR	Polymerase chain reaction
PDB	Protein Data Bank
$PepT_{so}$	Peptide transporter
pH	Potential hydrogen
PiPT	*Piriformospora indica* high affinity phosphate transporter
PVDF	Polyvinylidene difluoride
SD	Standard deviation
SE	Standard error
SDS	Sodium dodecyl sulfate
SLC	Solute carrier

TBS	Tris-buffered saline
TE	Tris EDTA
TEA	Tetraethylammonium
TMD	Transmembrane domain
TPA	Tetrapentylammonium
Tris	Tris aminomethane
UniProt	Universal protein resource
URAT	Uric acid transporter
UV	Ultraviolet
vcCNT	Concentrative nucleoside transporter

ABSTRACT

ELUCIDATION OF SUBSTRATE BINDING INTERACTIONS FOR HUMAN ORGANIC CATION TRANSPORTERS 1 (SLC22A1) AND 2 (SLC22A2) USING IN SILICO HOMOLOGY MODELING IN CONJUNCTION WITH IN VITRO SITE-DIRECTED MUTAGENESIS AND KINETIC ANALYSIS

Raymond Eugene Lai

Bachelor of Science, College of William and Mary, Williamsburg, Virginia, USA
Master of Science, Virginia Commonwealth University, Richmond, Virginia, USA
Doctor of Pharmacy; Virginia Commonwealth University, Richmond, Virginia, USA

A Dissertation submitted in partial fulfillment of the requirements for the degree of Doctor of Philosophy at Virginia Commonwealth University

Virginia Commonwealth University, 2018

Major Director: Douglas H. Sweet, Ph.D.
Professor, Chair

Department of Pharmaceutics, School of Pharmacy

The organic cation transporters (OCTs) play a critical role in the absorption, distribution and elimination of many drugs, hormones, herbal medicines, and environmental toxins. Given the broad substrate specificity of OCTs, they fall victim to the high susceptibility for contributing to harmful drug-drug interactions. Further defining how human (h)OCTs mechanistically bind to its broad array of substrates will provide significant insight to the understanding and prediction of drug-drug interactions in polypharmacy patients and the advancement of future rational drug design for

therapeutics targeting OCTs. The goal of the current study was to elucidate the critical amino acid residues for transporter-substrate binding interactions on human (h)OCT1 and 2 utilizing *in silico* molecular modeling techniques (homology modeling and automated docking), as well as *in vitro* mutagenesis and kinetic transport experiments.

Three-dimensional homology models were generated for hOCT1 and 2 using *Piriformospora indica* phosphate transporter (PiPT) serving as template. A putative binding pocket was identified and used to dock the prototypical substrate MPP^+. Docking studies revealed five residues for each transporter (hOCT1 and hOCT2) that may be critical for substrate-transporter interactions. The *in silico* data was used to guide subsequent *in vitro* site-directed mutagenesis and kinetic analysis. Four hOCT1 mutants (Gln241Lys, Thr245Lys, Tyr361Ala, and Glu447Lys) and three hOCT2 mutants (Gln242Lys, Tyr362Phe, and Tyr362Ala) showed complete loss of MPP^+ transporter activity. Decreased affinity for MPP^+ was observed for Phe244Ser and Thr245Ser in hOCT1, and Tyr245Ala in hOCT2. All amino acid residues highlighted in the *in vitro* experiments may be potentially critical for substrate-transporter interactions particularly Tyr361, Phe244 and Thr245 in hOCT1; and Tyr362 and Tyr245 in hOCT2. Docking of known structurally divergent hOCT1 and hOCT2 substrates revealed similar binding interactions as that identified for MPP^+, albeit with some unique residues, suggesting the presence of a large central cavity within both transporters.

Through the combination of *in silico* and *in vitro* experiments, a putative binding pocket was defined and several residues important for substrate-transporter interaction were identified and verified for hOCT1 and hOCT2. Further defining how OCTs biochemically interact with their broad array of substrates will provide significant insight

to the understanding and prediction of drug-drug interactions in polypharmacy patients and the advancement of future rational drug design for therapeutics targeting OCT1 and OCT2.

CHAPTER 1

OVERVIEW OF EXPRESSION AND FUNCTION OF ORGANIC CATION AND ANION TRANSPORTERS

Adapted from manuscript published in *Journal of Food and Drug Analysis*. (2018) 2: S45-S60 [1]

1.A SOLUTE CARRIER 22 TRANSPORTER FAMILY

Almost a quarter century has passed since the cloning of the first member of what is now recognized as the Solute Carrier 22 (SLC22) organic cation/anion/zwitterion transporter family. Currently, the Human Genome Organization Gene Nomenclature Committee recognizes some 50 SLC families (http://www.genenames.org/cgi-bin/genefamilies/set/752) with the SLC22 family containing 23 proposed members. The SLC22 family includes the organic anion transporters (OATs), organic cation transporters (OCTs) and organic cation/carnitine transporters (OCTNs) [2]. Eight members are extensively understood in terms of transport function, substrate specificity and driving forces; OCT1 (*SLC22A1*), OCT2 (*SLC22A2*), OCT3 (*SLC22A3*), OAT1 (*SLC22A6*), OAT2 (*SLC22A7*), OAT3 (*SLC22A8*), OAT4 (*SLC22A11*) and urate transporter 1 (URAT1, *SLC22A12*). While SLC22 family members are expressed in virtually every barrier membrane within the human body (including the blood-testis barrier, blood-brain barrier, blood-cerebrospinal fluid barrier, and various CNS cell types), expression and function in kidney, liver and intestine has received the most attention (Figure 1.1).

Structurally, members of the SLC22 family are proposed to have 12 membrane-spanning alpha helical domains, a large extracellular glycosylated loop between transmembrane domains (TMD) 1 and 2, a large intracellular loop between TMDs 6 and 7, and intracellular N and C-terminal domains [3] (predicted secondary structure of SLC22 family transporters shown in Figure 1.2). Within the large loop between the first and second TMDs, three N-linked glycosylation sites are present which are proposed to serve a variety of functions including protein stabilization, intracellular trafficking, and extracellular protease protection [4]. Six sulfhydryl groups (conserved cysteine residues) are also present which are theorized as mediators for forming ionic salt bridges which help stabilize the three dimensional loop structure critical for transporter oligomerization [3–5]. SLC22 family transporters are known to be polyspecific, in other words, they have the ability to translocate a variety of structurally diverse small molecules and can be inhibited by numerous other compounds [6–9]. Transporters within a given subtype commonly share a similar group of preferred substrates and inhibitors, as well as their mechanism of transport.

OCT and OAT substrates cover a wide array of chemical structures and classes including pharmacological agents (*e.g.*, morphine, tamoxifen, metformin, cimetidine, penicillin G, furosemide, adefovir, cidofovir, indomethacin), neurotransmitters and their metabolites (*e.g.*, dopamine, serotonin, homovanillic acid), hormones (*e.g.,* prostaglandins, estrone sulfate), environmental toxins/pollutants (*e.g.*, paraquat, 1-methyl-4-phenylpyridinium, ochratoxin A) and active components found in herbal preparations (*e.g.,* lithospermic acid, rosmarinic acid, rhein).

Experiments with renal membrane vesicles, tissue slices and intact tubules demonstrated that the inside negative membrane potential of a cell drives the uptake (cellular entry) of organic cations [10]. That is, cellular entry of organic cations mediated by SLC22 family members involves facilitated diffusion, which is 'powered' by the membrane potential difference and chemical gradient (Figure 1.3). The driving force for cellular exit mediated by this transport system was found to be a three-step process ending in organic cation/proton (H^+) exchange [10]. Initially, Na^+/K^+-ATPase directly hydrolyzes ATP and pumps Na^+ out of the cell to establish an inwardly directed Na^+ gradient, which is subsequently used by Na^+/H^+ exchanger 3 to establish an inwardly directed H^+ gradient, that ultimately serves to power cellular exit of organic cations via an organic cation/H^+ antiporter (Figure 1.3).

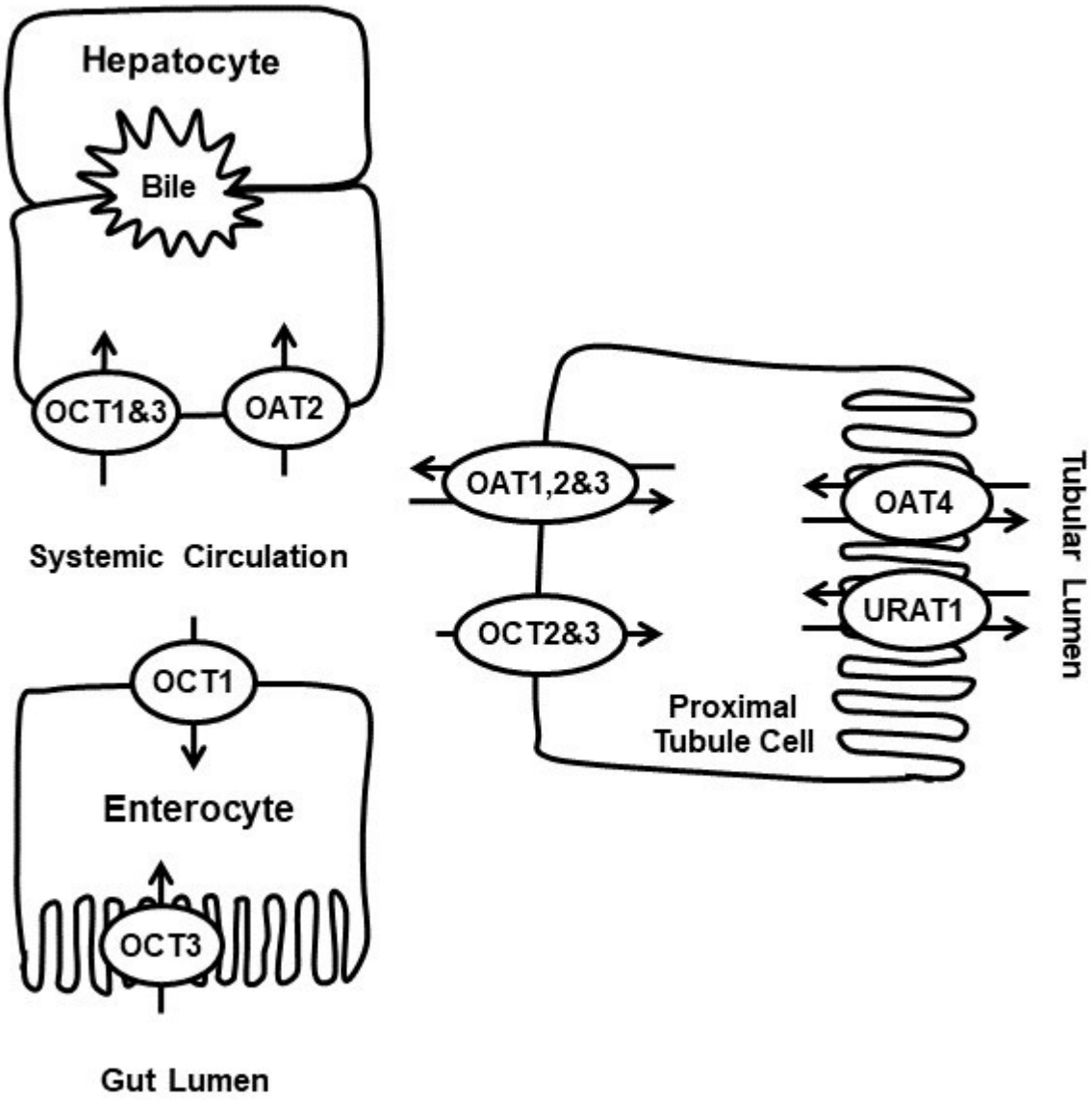


Figure 1.1 Prominent human SLC22 family members expressed in intestine, kidney and liver.

Representative depictions of a human enterocyte, hepatocyte and renal proximal tubular cell indicating SLC22 transporters expressed in each tissue and their plasma membrane localization.

Figure taken from reference [1].

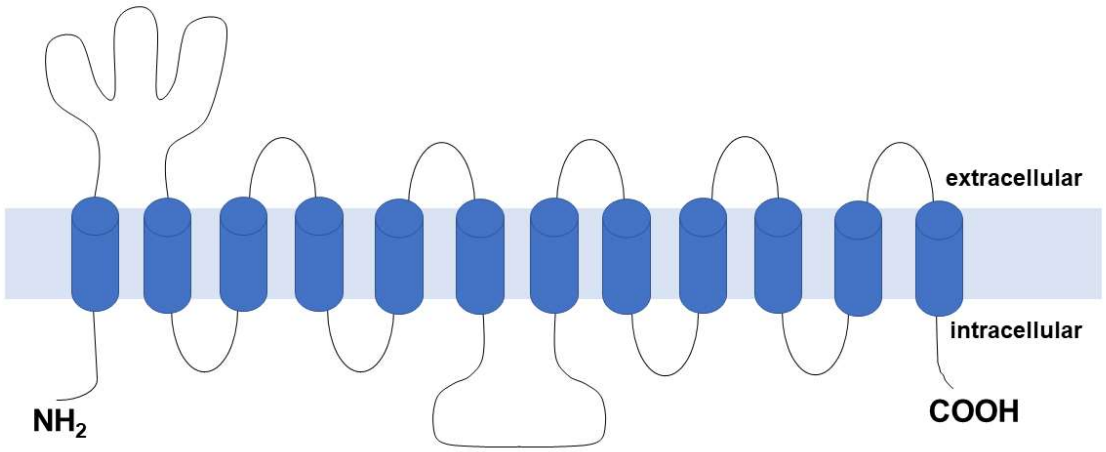


Figure 1.2 Predicted secondary structure of SLC22 transporters.

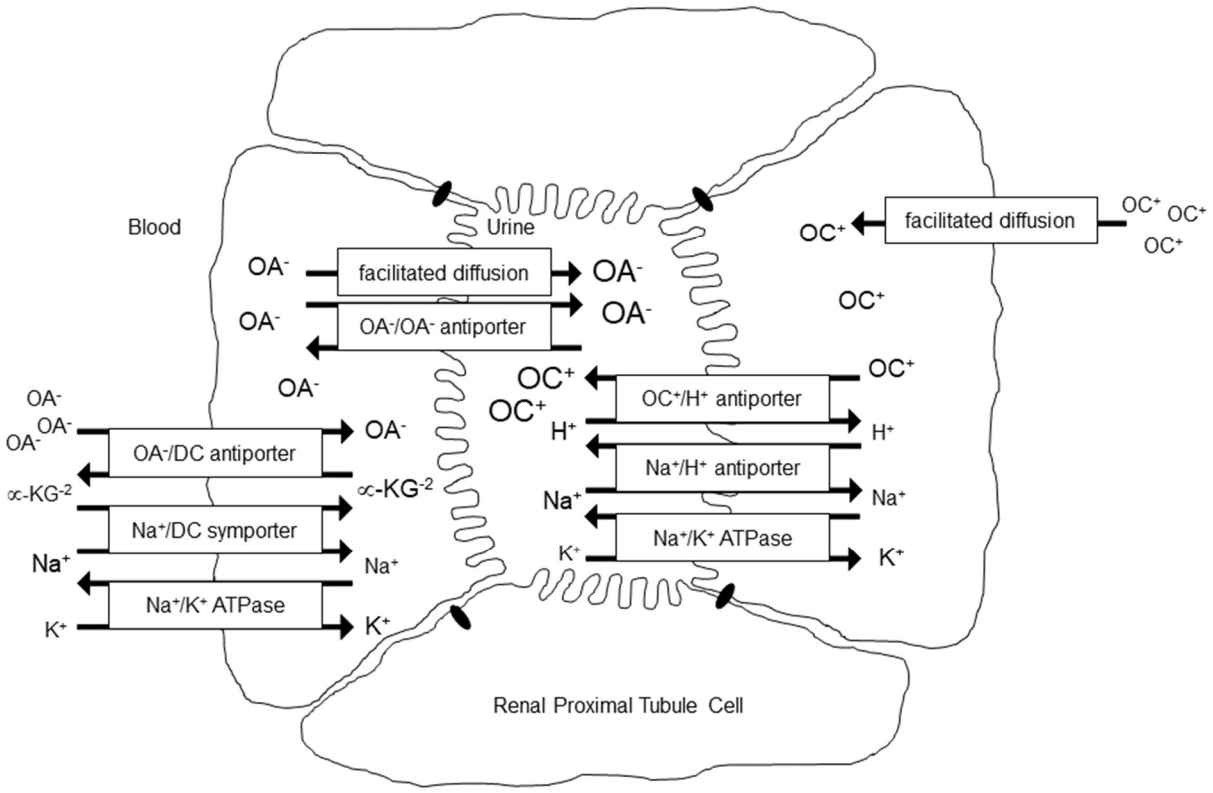


Figure 1.3 Model depicting driving forces for SLC22 family members.

Mechanisms/driving forces utilized for cellular entry and exit on the 'classical' organic cation and organic anion transport systems, using renal proximal tubule cell as an example.

Figure taken from reference [1].

For organic anions, cellular entry mediated by SLC22 family members requires energy input to drive their movement against the membrane potential (Figure 2). Experiments utilizing the above-mentioned systems demonstrated that uptake was coupled to established ion gradients (*e.g.*, Na^+, α-ketoglutarate) and not to direct ATP hydrolysis [10]. That is, cellular entry of organic anions mediated by SLC22 family members is driven by a three step process (similar to exit of organic cations) in which Na^+/K^+-ATPase establishes the inwardly directed Na^+ gradient, the Na^+/dicarboxylate symporter 3 utilizes the movement of Na^+ ions down their concentration gradient (into the cell) to power entry of α–ketoglutarate into the cell (maintaining an outwardly directed gradient) and, finally, an organic anion/dicarboxylate antiporter mediates organic anion uptake in exchange for α–ketoglutarate [10]. Evidence supports cellular exit via this transport system occurring either by facilitated diffusion (using the membrane potential as driving force) or anion exchange (antiport) [10].

A brief synopsis of the discovery of the well-characterized family members is presented below, for additional detail see [11–14]. For the purposes of this dissertation, subsequent discussion and experimental focus will be on human OCT1, OCT2, and OCT3.

1.B MAJOR ORGANIC CATION AND ANION TRANSPORTERS

OCT1 (SLC22A1). First isolated from rat kidney in 1994, orthologs have been identified in mouse and human (as well as other species) [15–17]. In humans, OCT1 expression has been conclusively reported in enterocytes and hepatocytes [15,18]. Rat Oct1 transport function correlated with changes in membrane potential, but not proton gradient manipulations, indicating OCT1 is driven by facilitated diffusion [17]. Protein expression in rats was subsequently confirmed by immunocytochemistry in renal proximal tubules and hepatocytes [19,20].

OCT2 (SLC22A2). Isolated in 1996 from rat kidney, orthologs have been identified in mouse and human (as well as other species) [15,21,22]. In humans, significant OCT2 expression has been reported in kidney, as well as in the CNS compartment [15,23–25]. Rat Oct2 transport function was ablated by membrane depolarization or a *trans*-applied proton gradient, indicating it is also driven by facilitated diffusion [26]. Renal expression and basolateral membrane targeting in intact rat proximal tubules was observed [27,28].

OCT3 (SLC22A3). Initially cloned from rat placenta [29], mouse and human orthologs (as well as other species) have been identified [30,31]. OCT3 appears to have the widest tissue distribution among the SLC22 family, including liver, kidney and intestine in humans [24,29,30]. Rat Oct3 function was demonstrated to be sensitive to changes in membrane potential indicating that it also is a facilitated diffusion carrier [29].

OAT1 (SLC22A6). Isolated in 1997 from rat kidney [32,33], orthologs have been identified in mouse and human (as well as additional species) [34–36]. OAT1 is expressed in kidney of all three species, but not in intestine or liver [25,33–35]. Renal expression and basolateral membrane targeting in isolated proximal tubules and human and rat

kidney was observed [37–39]. Mechanistic examination of rat Oct1 transport function demonstrated it is an organic anion/dicarboxylate exchanger [33].

OAT2 (SLC22A7). OAT2 was initially cloned from rat liver [40] and human and murine orthologs have been isolated [41,42]. Expression of OAT2 in kidney and liver, but not intestine, has been detected in mouse, rat and human [43,58,60,61]. OAT2-mediated uptake was characterized as being insensitive to *trans*-stimulation by dicarboxylates leading to the interpretation it likely operates via facilitated diffusion [45]. However, mechanistically, this would be inconsistent with its postulated role as an uptake carrier.

OAT3 (SLC22A8). OAT3 was first isolated from rat [46] with mouse and human (as well as other species) orthologs identified [47,48]. OAT3 expression has been observed in human kidney, but not liver or intestine [47]. Hepatic expression was reported in rats, but not mice [44,48]. Immunohistochemistry yielded signal for OAT3 in rat and human renal proximal tubules [37,38]. Exploration of OAT3 transport energetics identified Na^+-dependent *trans*-stimulation by glutarate indicating that it is driven by organic anion/dicarboxylate exchange [49].

OAT4 (SLC22A11). OAT4 was discovered in human kidney and placenta [25,50]. No additional orthologs or tissues of expression have been identified. Immunodetection in proximal tubules has been observed [51]. However, OAT4's precise mechanism of action remains unclear as it has been reported to be a facilitated-diffusion carrier [50], an organic anion/dicarboxylate exchanger [52], and a urate/OH^- exchanger [53].

URAT1 (SLC22A12). Originally isolated from mouse kidney, with rat and human orthologs subsequently identified [54–56]. Expression of URAT1 appears to be kidney

specific [55,56]. Characterization of URAT1-mediated transport indicated it functions as an organic anion/urate exchanger, however, tested dicarboxylates failed to inhibit [55,56].

Three key factors needed to most accurately define each individual SLC22 transporter's contribution to the transepithelial flux of substrate molecules in each tissue are (i) individual transporter affinities for each compound, *i.e.,* K_m, K_i, IC_{50}, (ii) the concentration of each compound in the systemic circulation, and (iii) absolute SLC22 protein expression levels in each tissue, ideally in both normal and disease states. Robust affinity data are relatively easy to come by using *in vitro* expression systems of which a great deal already exists (Table 1.1). Limited clinical systemic concentration information is available in the literature (Table 1.2), however, interpretation of these data should be approached with caution at this time due to the use of non-standardized dosage forms and inconsistent amounts of individual compounds administered in each study. Thus, more formalized clinical studies that administer actual marketed products are required to obtain relevant, product-specific (unbound) C_{max} values for each compound. Within this framework, organ-specific SLC22 protein expression data will further enhance our ability to accurately predict their impact on the absorption/flux of drugs, herbal supplement components and endogenous compounds. Toward this end, advances in liquid chromatography/tandem mass spectrometry methodology have begun to yield preliminary data regarding 'normal' human transporter expression levels in native cell membranes (summarized for SLC22 transporters in Table 1.3).

Future studies quantifying transporter expression levels in patients suffering from acute and chronic disease appear essential (*e.g.* renal or hepatic failure), as recent studies using rat models of ischemia/reperfusion injury and chronic renal failure have

demonstrated dramatic changes in SLC22 transporter expression levels. A common theme to all of these studies was a significant (~50-85%) downregulation of Oat1 and Oat3, and in one instance Oct2, protein expression in rat kidney as determined by immunoblotting [57–62]. When examined, this downregulation of SLC22 expression correlated with decreased renal clearance of Oat1 and Oat3 substrates [57,58,61]. For example, in the ischemia/reperfusion model, significant accumulation of endogenous indoxyl sulfate in the systemic circulation was observed beginning at 6 hours post injury and the concentration of administered famotidine (20 mg/kg), a substrate for both OCTs and OATs, was significantly elevated compared to control rats [58,59]. Thus, quantifying transporter protein levels under conditions of organ dysfunction/insufficiency should substantially improve modeling and prediction of compound distribution in such patients.

Table 1.1 Example compound interactions associated with SLC22 transporters.

Perpetrator	Victim substrate[b]	Transporter[c]	Cell Type[d]	Kinetics (μM)			Reference
				K_m	IC_{50}	K_i	
Aloe-emodin	6-CF	hOAT1	MDCK		2.29		[63]
	6-CF	hOAT3	HEK293		5.37		[63]
Chrysophanol	6-CF	hOAT1	MDCK		>10		[63]
	6-CF	hOAT3	HEK293		>10		[63]
Cisplatin		hOCT2	HEK293	11			[64]
CMPF[a]		hOAT1	HEK293	141			[65]
		hOAT3	HEK293	27			[65]
Diclofenac	Adefovir	hOAT1	CHO		4		[66]
Diflunisal	Adefovir	hOAT1	CHO		0.85		[66]
Emodin	6-CF	hOAT1	MDCK		0.61		[63]
	6-CF	hOAT3	HEK293		1.22		[63]
Ethambutol	MPP^+	hOCT1	HEK293		93		[67]
	MPP^+	hOCT2	HEK293		254		[67]
	MPP+	hOCT3	HEK293		4100		[67]
Etodolac	Adefovir	hOAT1	CHO		50		[66]
Flurbiprofen	Adefovir	hOAT1	CHO		1.5		[66]
Gallic acid	PAH	hOAT1	CHO		1.2	1.1	[68]
	ES	hOAT3	HEK293		9	8.4	[68]
Ibuprofen	Adefovir	hOAT1	CHO		8		[66]
Indomethacin	Adefovir	hOAT1	CHO		3		[66]
Indoxyl sulfate		hOAT1	HEK293	21			[65]
		hOAT3	HEK293	263			[65]
Ketoprofen	Adefovir	hOAT1	CHO		1.3		[66]
Lithospermic acid	PAH	hOAT1	CHO			20.8	[69]
	ES	hOAT3	HEK293			0.59	[69]

	PAH	mOat1	CHO			14.9	[69]
	ES	mOat3	CHO			31.1	[69]
Nadolol		hOCT2	HEK293	122			[70]
Naproxen	Adefovir	hOAT1	CHO		5.8		[66]
p-cresyl sulfate		hOAT1	HEK293	128			[71]
		hOAT3	HEK293	>5000			[71]
Phenacetin	Adefovir	hOAT1	CHO		200		[66]
Physcion	6-CF	hOAT1	MDCK		> 10		[63]
	6-CF	hOAT3	HEK293		> 10		[63]
Piroxicam	Adefovir	hOAT1	CHO		20.5		[66]
Rhein	6-CF	hOAT1	MDCK		0.23		[63]
	6-CF	hOAT3	HEK293		0.08		[63]
	PAH	hOAT1	CHO		0.077	0.072	[72]
	ES	hOAT3	CHO		0.008	0.008	[72]
	ES	hOAT4	CHO		>100	>100	[72]
	PAH	mOat1	CHO			0.198	[72]
	ES	mOat3	CHO			0.216	[72]
Rosmarinic acid	PAH	hOAT1	CHO			0.35	[69]
	ES	hOAT3	HEK293			0.55	[69]
	PAH	mOat1	CHO			5.5	[69]
	ES	mOat3	CHO			4.3	[69]
Rosuvastatin	ES	hOAT3	*Xenopus* oocytes	7.4	25.7		[73]
Salvianolic acid A	PAH	hOAT1	CHO			5.6	[69]
	ES	hOAT3	HEK293			0.16	[69]
	PAH	mOat1	CHO			4.9	[69]
	ES	mOat3	CHO			21.3	[69]

Salvianolic acid B	PAH	hOAT1	CHO		22.2	[69]
	ES	hOAT3	HEK293		19.8	[69]
	PAH	mOat1	CHO		236	[69]
	ES	mOat3	CHO		845	[69]
Tanshinol	PAH	hOAT1	CHO		40.4	[69]
	ES	hOAT3	HEK293		8.6	[69]
	PAH	mOat1	CHO		136	[69]
	ES	mOat3	CHO		1940	[69]
Ursolic Acid	ES	hOAT3	HEK293	19		[74]

[a] CMPF, 3-carboxy-4-methyl-5-propyl-2-furanpropanoic acid

[b] 6-CF, 6-Carboxyfluorescein; PAH, *p*-aminohippurate; ES, estrone sulfate

[c] h, human; m, murine

[d] MDCK, Madin-Darby canine kidney; HEK293, human embryonic kidney; CHO, Chinese hamster ovary

Table taken from reference [1]

Table 1.2 Clinical concentrations of example compounds.

Compound	Mean C_{max} (μM)[a]	Route of Administration	Dose	Species	Reference
Aloe-emodin	0.29	PO	1.25 mg/kg[b]	Rat	[75]
Cisplatin	0.02-0.03	IV	80 mg/m^2	Human	[76]
Chrysophanol	4.7	PO	1.25 mg/kg[b]	Rat	[75]
CMPF[c]	24.8	-	-	Human	[77]
Diclofenac	6.6	PO	100 mg	Human	[78]
Diflunisal	247.8	PO	500 mg	Human	[79]
Emodin	0.14	PO	1.25 mg/kg[b]	Rat	[75]
Ethambutol	22, 4.8-26.9	PO	25 mg/kg, 400 mg	Human	[80], [81]
Etodolac	26.1-57.1	PO	50 mg/kg	Rat	[82]
Flurbiprofen	172.3	PO	100 mg	Human	[83]
Gallic acid	0.55	PO	400 mg/kg (40 μg)[d]	Human	[84]
Ibuprofen	208.4-282.1	PO	800 mg	Human	[85]
Indomethicin	3.9-6.7	PO	40 mg, 50 mg	Human	[86]
Indoxyl Sulfate	2.5	-	-	Human	[87]
Ketoprofen	13.8-17.8	PO	100 mg	Human	[88]
Lithospermic Acid	55.7	IV	10 mL/kg (0.3 mg/kg)[e]	Rat	[89]
Nadolol	0.17	PO	30 mg	Human	[90]
Naproxen	187.1	PO	220 mg	Human	[91]
p-cresyl sulfate	425.1	-	-	Human	[87]
Phenacetin	12.5	PO	900 mg	Human	[92]
Physcion	1.7	PO	1.25 mg/kg[b]	Rat	[75]
Piroxicam	1.3	PO	20 mg	Human	[93]
Rhein	0.54, 2.6	PO	1.25 mg/kg[c], 6 g/kg[f]	Rat	[75], [94]
Rosmarinic acid	317.2	PO	20 g/kg (0.391 mg/g)[g]	Rat	[95]

	516.2	IV	10 mL/kg (1.86 mg/kg)[e]	Rat	[89]
Rosuvastatin	0.012-0.076	PO	20 mg	Human	[96]
Salvianolic acid A	0.28	PO	15 g/kg (37.9 mg/kg)[h]	Rat	[97]
	66.7	IV	10 mL/kg (0.33 mg/kg)[e]	Rat	[89]
Salvianolic acid B	0.14	PO	15 g/kg (15 mg/kg)[h]	Rat	[97]
	237.9	IV	10 mL/kg (1.714 mg/kg)[e]	Rat	[89]
Tanshinol	781.7	PO	20 g/kg (0.743 mg/g)[g]	Rat	[95]
Ursolic acid	2	PO	0.1 g/kg[i]	Rat	[98]

[a] Converted to μM from original study
[b] Semen Cassiae extract
[c] CMPF, 3-carboxy-4-methyl-5-propyl-2-furanpropanoic acid
[d] Mang-Guo-Zhi-Ke tablet, value in parenthesis represents amount of compound quantified in dosage form
[e] Danshen injection, value in parenthesis represents amount of compound quantified in dosage form
[f] Rhubarb extract
[g] Denshen-Chuanxiong-Honghua extract; value in parenthesis represents amount of compound quantified in dosage form
[h] Jitai tablet; value in parenthesis represents amount of compound quantified in dosage form
[i] Folium Eriobotryae effective fraction

Table taken from reference [1]

Table 1.3 Absolute native tissue protein expression levels for human SLC22 transporters.

Transporter	Kidney[a]	Liver[a]	Intestine[a]	Reference
OAT1	5.33±1.88	NE[b]	NE[b]	[25]
OAT2	0.93±0.32	1.91±0.58	NE[b]	[25], [99]
OAT3	3.50±1.55	NE[b]	NE[b]	[25]
OAT4	0.52±0.23	NE[b]	NE[b]	[25]
OCT1	NE[b]	7.35 ± 3.26, 4.45 ± 1.89	0.50[c]	[99], [100], [101]
OCT2	7.42±2.84	NE[b]	NE[b]	[25]
OCT3	NR[d]	NR[d]	0.10[c]	[101]

[a] Data are presented as pmol/mg protein ± SD
[b] NE = not expressed in this tissue in humans
[c] Values estimated from Figure 4 in reference [101], expressed in ileum only
[d] NR = not reported

Table taken from reference [1]

Human OCT1, OCT2, and OCT3 share overlapping substrate specificity, which may be due to a number of factors including having significant sequence similarity (70% identical) and similar two-dimensional structure (12 membrane spanning alpha helices) [6]. Strong evidence has shown OCTs bind to hundreds of clinically important compounds, and as a result of this polyspecificity, their function impacts the pharmacokinetic and dynamic effects associated with commonly prescribed medications (*e.g.* cimetidine, metformin), as well as complications arising from drug-drug interactions (DDI) [102]. Clinical studies have shown a 1.2-1.7 fold increase in metformin AUC and an overall decrease in its renal elimination when co-administered with the OCT2 inhibitors cimetidine, trimethoprim, or lansoprazole [103–105]. Similarly, *in vivo* studies in rats found altered pharmacokinetics and decreased elimination of cationic medications were associated with downregulation of OCT2 [106,107]. Additional clinical studies have shown that OCT1 genetic polymorphisms can also contribute to variations in patient response to metformin, particularly its efficacy and distribution [108,109]. Finally, studies utilizing OCT3 knockout mice found decreased bioavailability and decreased elimination of orally administered metformin [110,111]. Thus, all three OCT paralogs may differentially impact the overall pharmacokinetics and efficacy of metformin according to their tissue expression and polarity of membrane targeting (Figure 1.1).

By virtue of where they are expressed, OCTs have clearly exhibited a strong presence in potentiating pharmacokinetic properties of numerous drugs and DDIs. Major regulatory agencies, including the U.S. Food and Drug Administration (FDA) and European Medicines Agency (EMA), through their guidances strongly suggest the importance of *in vitro* testing of new drug candidates to determine their renal elimination

and drug-drug interaction potential, specifically emphasizing their interaction likelihood with the SLC22 members OCT2, OAT1, and OAT3 [112,113]. From recent discussions within the International Transporter Consortium, OCT1, is an emerging clinically important transporter that soon could be included in the guidances due to an increasing number of studies showing strong associations between OCT1 polymorphisms and pharmacokinetic and pharmacodynamic drug effects [114–119]. As such, conducting additional pharmacogenomic studies may be strongly advised for new drugs that are substrates of OCT1, particularly those with narrow therapeutic windows. It would not be surprising to soon see OCT3 added to this list as well.

Despite this broad evidence supporting the significance of the role of OCT1, OCT2, and OCT3 in the translocation of scores of endogenous and exogenous compounds, little to nothing is known regarding the biochemical nature of the interactions between known substrates/inhibitors and the transporters. In order to establish a strong predictive model for DDIs and optimize drug delivery while minimizing harmful side effects for novel drug candidates in the pharmaceutical pipeline, identifying the three-dimensional structure, substrate-binding pocket, as well as the critical amino acid residues involved in OCT-substrate interactions is paramount [120]. The most direct method to achieve this overall objective is through the utilization of x-ray crystallography. However, to date, only a limited number of membrane bound proteins have been successfully crystallized, none of which includes any members of the SLC22 family [121]. Therefore, it is of utmost importance to resort to alternative approaches. To that end, the construction and application of homology models that are based on the experimentally determined high resolution structure of related proteins has served as a promising option for characterizing

transporter structural properties, substrate-transporter interactions, and mechanisms of substrate translocation [121–123].

1.C CURRENT SCOPE OF MOLECULAR MODELING

Initial attempts to understand the nature of transporter-substrate interactions for organic cation transporters were initially performed on rat Oct1 and Oct2 [124,125]. Preliminary knowledge of secondary structure derived from hydropathy sequence analysis was used in conjunction with identified evolutionarily conserved amino acid regions and amino acid physicochemical properties, in order to identify potential critical regions for ligand binding [124,125]. Since OCT ligands carry a positive charge, acidic amino acids in these regions were targeted. For example, the aspartic acid at position 475, located in TMD 11, which is conserved in OCTs, but not OATs, was subjected to mutagenesis resulting in changes in rat (r)Oct1 transport activity and suggesting its potential significance as an important binding site [124]. Follow up studies were performed to determine the amino acids responsible for the higher affinity of the steroid hormone, corticosterone, for rOct2 compared with rOct1 [126,127]. Through a series of mutations involving the exchange of amino acids between the two paralogs and the measurement of different transporter properties, amino acids that may be critical for substrate-transporter interactions were identified (Table 1.5) [125]. Thus, what specifically distinguishes the OCT paralogs in terms of substrate affinity and/or specificity may be related to amino acid differences in these critical regions.

Despite some apparent success utilizing 2-D models as the basis for establishing potential critical binding residues, a significant limitation was the inability to determine the binding pockets for substrate-transporter interaction. This limitation can be addressed

through the use of more advanced technologies such as X-ray crystallography and NMR. However, these methods also have their own limitations such as requiring pure sample preparations in concentrations significantly higher than how much they normally appear in their natural system. For using NMR to determine protein structure, there also exists the hurdle of size limitation, with current technology only being able to process protein masses up to 15 kD [128]. Nevertheless, obtaining such structural knowledge can be extremely useful for designing effective and safe therapeutic medications [122], understanding disease caused by protein polymorphisms [129], as well as optimizing the process of elucidating the biochemical interactions of proteins [128].

Comparative or homology modeling has gained traction in bridging the gap between sequence and structural space, as it allows investigators to obtain a reasonable prediction of the tertiary structure for proteins that are difficult to crystallize or for which structure determination via experimental methods like NMR is not feasible. Homology modeling relies on the basis that two proteins that are evolutionarily similar in sequence also exhibit analogous structures [130]. The protein with the known structure serves as the template for the construction of a model for the protein for which the tertiary structure is not known. According to Protein Data Bank [131], the repository of experimental structures, the total number of experimental protein structures available to date has reached 83,975, however, the rate at which structures are solved experimentally is still outpaced by the rate at which new proteins are discovered [132]. This fact adds enhanced emphasis to the importance of utilizing homology modeling as a technique that can assist in the drug discovery process by aiding the study of the biochemical basis of ligand-protein interactions, providing novel insight to processes impacting substrate specificity,

as well as elucidating structure-function relationships [122]. The degree of structural insight provided by homology modeling relies heavily on the degree of sequence similarity between the template and target protein [133]. In general, models derived by sequence identities > 30% are deemed homologous and presumed to share a common 3-D structure based on their evolutionary divergence [134]. Models based on sequence identities of 25-50% are considered sufficient for informing site-directed mutagenesis experiments, and those >50% are considered reliable for structure-based drug design, while sequence identities below 15% are considered suspect for structural modeling [134]. The basic steps for homology modeling includes the following: template selection, template-target alignment, model building, and model evaluation [135]. This process has more recently been coupled with molecular docking in order to optimize models for protein-ligand interaction studies as well as structure-based drug design [136].

Template selection begins through the utilization of a sequence search program (*e.g.* BLAST). Interestingly, although sharing >40% sequence similarity is considered a reasonable template for most target proteins, many SLC family members share the same secondary structure (same number of folds) in spite of their low overall sequence similarity (~10%) [137]. Next, the template and target protein sequences are aligned based on their evolutionarily conserved regions by the commonly used program ClustalX [138]. Sources of dissimilarity may be due to the presence of large exposed loops between transmembrane domains. For optimal homology modeling, especially for challenging targets like SLC22s, it is thus important to visually inspect the results, remove such loop sequences, and perform any necessary manual adjustments to minimize the gaps in the sequence [135]. Once the template-target alignment is generated, 3-D model

building is initiated based on the template protein structure. The frequently used program, MODELLER (University of California at San Francisco, San Francisco, CA) [139], depends on satisfaction of spatial and stereochemical constraints derived from the template structure guided by the template-target alignment [123]. The top ranked models are then subjected to careful visual inspection to refine errors caused by target-template sequence divergence of the top-ranked models and validated using a variety of different methods. Such validation methods include the evaluation of stereochemical properties (*e.g.* PROCHECK) [140] and the environment of each amino acid in the model with respect to the environment found in experimentally determined structures (*e.g.* Z-DOPE) [141]. Membrane transporters in general pose several challenges for homology modeling given their diverse transmembrane secondary structure profiles and their relatively low sequence identities/similarities to related solved crystal structures [135].

Table 1.4. Summary of the SLC family homology model template recommendations[a].

Family	Template transporter	
	Name	**Function**
SLC7	AdiC	Amino acid antiporter
SLC10	$ASBT_{NM}$	Apical sodium-dependent bile acid transporter
SLC15	$PepT_{SO}$	Peptide transporter
SLC22	High-affinity phosphate importer PiPT	Organic cation/anion/zwitterion transporters
SLC28	vcCNT	Concentrative nucleoside transporter
SLC47	NorM	Multidrug and toxin extrusion (MATE) transporters

[a] Table adapted from reference [142]

Two transporters, derived from *Escherichia coli* (*E. coli*), that were successfully crystallized, lactose permease transporter (LacY, PDB ID: 1PV6) and glycerol-3-phosphate transporter (GlpT, PDB ID: 1PW4) have been used previously to homology model rat Oct1, rabbit Oct1 and Oct2, and human OCT2 [143–146]. Transport activity for MPP^+ and TEA was measured in mutants of 18 consecutive amino acids in TMD 4 of rat Oct1 [143]. The rationale behind the mutation strategy was based on the fact that TMD4 contains amino acids on one side of the presumed alpha helix that are conserved within the three paralogs of OCTs, but not the OATs. The changes observed in transport activity of MPP^+ and TEA identified three amino acid residues (Tyr218, Tyr222, and Thr226) critical in a proposed binding pocket (Table 1.5). Subsequent homology modeling using LacY as template appeared to support this contention [143]. Similarly, in a different study, markedly different affinities for selected substrates between rabbit Oct1 and Oct2 were demonstrated through site directed mutational studies [145]. Glu447 was found to exert a marked influence for substrate selectivity in rabbit Oct2. This result was consistent with a subsequently constructed inward open 3-D homology model derived from GlpT, which showed Glu447 residing in a hydrophilic cleft of the putative docking region of rabbit Oct2 [145,147]. An additional study was conducted showing that substitutions at Cys451 decreased rabbit Oct1 affinity for choline, which was later shown to reside in the choline binding domain of a LacY derived homology model [148]. Another group further studied human OCT2 and tested the interaction potential of several homologous conserved cysteine residues found within TMD 10 and 11 that were theorized to comprise the hydrophilic binding cleft [146]. A 3-D homology model was generated for human OCT2 using GlpT as template to help validate their findings showing that Cys474 serves to form

a transport pathway for the OCT2 substrate TEA [146]. Notably, these studies utilized homology modeling in an attempt to correlate their mutational study results rather than using homology modeling and docking to drive the mutational studies. Amino acid residues deemed critical for substrate-binding resulting from these initial tertiary structure-based modeling studies are summarized in Table 1.5.

Table 1.5 Summary of critical residues discovered through initial OCT modeling studies.

Transporter[a]	Topology Model	Template	Critical residue	Substrate	Reference
rOct1	2-D	-	Asp475 (TMD11)	MPP^+	[124]
rOct1	2-D	-	Ile443, Leu447, Gln448 (TMD 10)	MPP^+, TEA, Corticosterone	[125]
rOct2	2-D	-	Ile443, Tyr447, Glu448 (TMD 10)	MPP^+, TEA, Corticosterone	[125]
rOct1	3-D	LacY	Tyr218, Tyr222, Thre226 (TMD 4)	TEA	[143]
rbOct1	3-D	LacY	Cys451 (TMD 10)	Choline	[144]
rbOct2	3-D	GlpT	Glu447 (TMD 10)	TEA	[145]
hOCT2	3-D	GlpT	Cys474 (TMD 4)	TEA	[146]

[a] r, rat; rb, rabbit; h, human

While in the aforementioned studies, several potentially important amino acids for substrate binding were identified, the relatively low sequence identity of LacY and GlpT with the OCTs (~15%) casts strong doubt as to the exact alignment between the target and template [134]. A recent comprehensive comparative analysis of key SLC member sequences was conducted, resulting in updated recommendations for crystal structure templates in SLC homology modeling [142]. As indicated in Table 1.4, a new protein, *Piriformospora indica* phosphate transporter (PiPT) from the major facilitator superfamily (MFS) that has recently been crystallized is considered as the best available template for OCT homology modeling studies [149]. *Piriformospora indica* is a eukaryotic endophytic fungus that colonizes the roots of several plant species and is involved in enhancing plant growth [149]. PiPT has been recently shown to be a high-affinity transporter responsible for improving phosphate nutrition levels in the host plant [150]. PiPT, like hOCTs, has 12 membrane domain spanning alpha helices [149]. There are specific residues at Tyr328 and Trp320 on TMD 7 of PiPT that are highly conserved in the SLC22 family which suggests a shared substrate-binding mechanism using this helix. PiPT possesses higher sequence identity with OCTs (~21% identical, 40% similar) than LacY and GlpT, thus increasing the confidence for guiding mutagenesis experiments. Furthermore, PiPT is derived from a eukaryotic organism making it evolutionarily more related with the mammalian OCTs compared to LacY and GlpT which are both derived from a prokaryote (*E*. coli). LacY and GlpT were both crystallized in an inward-open state while PiPT was crystallized in the occluded state which adopts a compact helical arrangement around the substrate binding site maximizing the possible interactions between the docked ligand and proposed transporter interaction pocket [147,149,151]. An important feature that

PiPT possesses that is absent in LacY and GlpT is the intracellular loop between TMD 6 and 7 that is also evolutionarily conserved in OCTs.

Therefore, given the aforementioned information, it would seem prudent that homology modeling studies in hOCTs be considered using the most recently crystallized MFS member, PiPT, to elucidate the amino acid residues critical for transporter-substrate binding interactions in human OCT1 and OCT2.

CHAPTER 2

RESEARCH OBJECTIVES AND SPECIFIC AIMS

2.A RESEARCH OBJECTIVES AND HYPOTHESIS

The overarching goal of the current study is to elucidate the critical amino acid residues for transporter-substrate binding interactions on human (h)OCT1 and OCT2 through *in silico* molecular modeling techniques (homology modeling and automated docking), followed by *in vitro* mutagenesis and kinetic transport experiments. Our hypothesis is that through the substitution of hOCT1 and hOCT2 amino acids involved in substrate-transporter interactions, identified by *in silico* homology modeling with *Piriformospora indica* phosphate transporter (PiPT) as template and molecular docking studies, a change in affinity (K_m) of the transporter to its prototypical substrate MPP^+ will be produced.

2.B SPECIFIC AIMS TO ADDRESS HYPOTHESIS

SPECIFIC AIM 1

To identify critical amino acid residues for substrate-binding in hOCT1 and hOCT2

a. An *in-silico* 3-dimensional (3-D) predictive homology model of hOCT1 and hOCT2 will be constructed using *Piriformospora indica* phosphate transporter (PiPT) as the model template.

b. Ligand docking studies will be conducted using the organic cation transporter model substrate 1-methyl-4-phenylpyridinium (MPP^+) to determine the putative substrate binding pocket(s) for hOCT1 and hOCT2.
c. Putative amino acid residues involved in MPP^+ substrate-transporter interaction will be identified.

SPECIFIC AIM 2

To confirm the validity of the predicted critical residues associated with hOCT1 and hOCT2 substrate recognition determined through 3-D homology modeling and ligand docking, a series of steps to examine changes in substrate affinity will be performed including:

a. The introduction of conservative and non-conservative substitutions that alter predicted critical amino acid residues using site-directed mutagenesis.
b. The creation of stably transfected cell lines expressing hOCT1 and hOCT2 mutants.
c. Kinetic analysis to determine the affinity of hOCT1 and hOCT2 mutants for the prototypical substrate MPP^+.
d. Confirming membrane targeting for hOCT1 and hOCT2 mutants with attenuated transport activity (*e.g.* via immunodetection with Western blots or immunocytochemistry).

SPECIFIC AIM 3

To further evaluate the generated *in silico* hOCT1 and hOCT2 models, substrates with disparate structures will be docked to determine the presence of alternative and/or additional critical amino acid residues in the binding pocket(s). This will be evaluated by:

a. Performing additional docking studies using OCT substrates with varying structures (*e.g.* epinephrine, tetrapentylammonium (TPA), serotonin, metformin, cimetidine).
b. Comparisons of proposed critical amino acid residues mediating transporter-substrate interactions across human OCT1, OCT2 (current work) and OCT3 (previous work).

CHAPTER 3

IDENTIFYING STRUCTURAL ELEMENTS OF HUMAN ORGANIC CATION TRANSPORTER 2 (SLC22A2) MEDIATING SUBSTRATE-TRANSPORTER INTERACTIONS

3.A INTRODUCTION

Transporters, which have garnered much interest in the field of clinical pharmacology and pharmaceutics, are extensively expressed throughout the body. They serve a variety of functions that include the uptake and elimination of both endogenous and exogenous compounds. One group of transporters that recognize a broad-spectrum of small organic compounds with positive charge are the organic cation transporters OCT1, OCT2, and OCT3 [6]. These transporters belong to the solute carrier 22 family (SLC22) of the major facilitator superfamily (MFS) and share high sequence homology [6,152]. The OCTs are proposed to have 12 membrane-spanning alpha helical domains, a large extracellular glycosylated loop between transmembrane domains (TMD) 1 and 2, a large intracellular loop between TMDs 6 and 7, and intracellular N- and C-terminal domains.

Due to their expression in intestine, liver, and kidney, the OCTs exert significant impact on the pharmacokinetic and pharmacodynamic effects relating to the safety and efficacy of many common medications, as well as on the resulting complications arising from drug-drug interactions. Both the U.S. Food and Drug Administration (FDA) and European Medicines Agency (EMA) have issued guidance documents recognizing the importance of transporter research in the drug development process [112,113]. The

guidances define circumstances under which new investigational drugs should be evaluated *in vitro* as potential transporter substrates, to project their drug-drug interaction potential, specifically SLC22 family members including OCT2 (*SLC22A2*), OAT1 (*SLC22A6*), and OAT3 (*SLC22A7*) [112]. OCT1 (*SLC22A1*) is an emerging clinically important transporter under consideration for addition to the guidances.

Despite the vast literature base detailing the hundreds of different endogenous and pharmaceutical substrates and inhibitors associated with OCTs, the biochemical nature of their binding interactions has yet to be determined. The approach to better understanding the intricacies of drug transport and ultimately optimizing drug delivery and elimination while reducing toxicity lies in 1) revealing the structural foundations of the substrate binding region(s), 2) understanding how the variety of substrates bind to this(ese) region(s), and 3) how substrate binding contributes to its translocation across membranes [120]. The simplest and most direct approach to achieving this goal is to determine the structure of the transporter-substrate complex through x-ray crystallography. However, to date, no crystal structure of any of the OCTs has been successfully solved. An alternative strategy involves the construction of a homology model using the known crystal structure of a closely related transporter protein. The homology model can then be used to dock substrates *in silico* to identify putative binding pocket(s) and critical residues participating in the binding interactions between substrate and transporter.

Previous homology modeling of rabbit Oct1 and Oct2, and human OCT2 based on the tertiary structure of the lactose permease (LacY) and glycerol-3-phosphate (GlpT) transporters from *E. coli* has been performed [143,146,148,153]. However, it is important

to note that these bacterial transporter templates exhibit extremely low (~15%) sequence identity with mammalian (human) OCTs. Generally, sequence identities of 25-50% are considered necessary to generate models useful for informing site-directed mutagenesis experiments, with sequence identities below 15% considered suspect for structural modeling [134]. Recently, the crystal structure of a more closely related MFS member, the *Piriformospora indica* phosphate transporter (PiPT), has been solved [149]. PiPT exhibits ~21% sequence identity with human OCT1, OCT2, and OCT3, and, therefore, should provide a better template for generating homology models of these transporters.

Thus, in order to elucidate the critical amino acid residues for transporter-substrate binding interactions on hOCT2, a series of *in silico* and *in vitro* experiments were conducted. Initially, a novel 3-D homology model for hOCT2 was developed using the known crystal structure PiPT. The PiPT structure represents the transporter in its occluded state, with endogenous ligand bound. The resulting hOCT2 homology model was then used to dock the prototypical substrate, MPP^+, to identify the binding pocket(s) and potential substrate interacting residues located within it. Next, mutant hOCT2 transporters containing conservative and non-conservative substitutions of interacting residues predicted from the generated model were constructed through site-directed mutagenesis. Subsequently, cell lines stably expressing the individual mutant hOCT2 transporters were established and used to conduct kinetic transport assays (saturation analysis) to determine any changes in transporter function and affinity (K_m) for MPP^+.

3.B MATERIAL AND METHODS

3.B.1 Chemicals and reagents

Tritiated [^{3}H] MPP^+ was purchased from PerkinElmer Life and Analytical Science (Waltham, MA) and unlabeled MPP^+ was obtained from Sigma-Aldrich (St. Louis, MO). Quinine monohydrochloride dihydrate was purchased from Acros Organics (Fair Lawn, NJ). Bio-Rad protein assay dye reagent concentrate was purchased from Bio-Rad Laboratories, Inc. (Hercules, CA). Specific primers for mutation reactions were purchased from Integrated DNA Technologies (IDT; Coralville, IA). QuikChange Lightning Site-Directed Mutagenesis Kit was purchased from Agilent Technologies (Santa Clara, CA). Lipofectamine® 2000 Transfection Reagent and Prolong diamond antifade mountant with DAPI was purchased from ThermoFisher Scientific (Waltham, MA). QIAprep spin miniprep kit and QIAprep spin midiprep kit [154] were purchased from QIAGEN Inc. (Germantown, MD). GoTaq green master mix was purchased from Promega (Madison, WI). Opti-Mem reduced serum and Dulbecco's modified eagle's medium were purchased from Life Technologies (Carlsbad, CA). Abcam plasma membrane protein extraction kit (ab65400) was purchased from Abcam (Cambridge, United Kingdom). Rabbit anti-SLC22A2 polyclonal antibody (GTX46838) was purchased from GeneTex (Irvine, CA), anti-rabbit IgG alkaline phosphatase (AP)-linked antibody (7054S) was purchased from Cell Signaling Technology (Danvers, MA), goat anti-actin polyclonal antibody (SC-1616), donkey anti-goat IgG-AP (sc-2022), goat anti-rabbit IgG- fluorescein isothiocyanate (FITC) (SC-2012), and donkey anti-goat IgG-FITC (SC-2024) were purchased from Santa Cruz Biotechnology (Dallas, TX). Nitro-blue tetrazolium and 5-bromo-4-chloro-3'-

indolyphosphate (NBT/BCIP) and complete mini protease inhibitor cocktail tablets were purchased from Roche Diagnostics (Mannheim, Germany).

3.B.2 Homology modeling and docking studies

The hOCT2 (UniProt ID: O15244) and PiPT (PDB ID: 4J05) sequences were obtained from the Universal Protein Resource (UniProt) and PDB, respectively [131,155]. Protein sequence alignment of PiPT and hOCT2 was performed with ClustalX and followed by sequence curating via loop removal and manual refinement of gaps based on the transmembrane domains observed in the PiPT crystal structure and predicted for hOCT2 using ICM Browser (Molsoft LLC) and Phobius (Stockholm Bioinformatics Center). Amino acid sequence alignment of hOCT2 with the template and subsequent generation of a population of 100 homology models were performed using ClustalX 2.1 and MODELLER v9.17, respectively. Using SYBL-X 2.1, a structural cavity search was conducted for each model to identify putative binding pocket(s). The hOCT2 substrates, MPP^+, epinephrine, serotonin, cimetidine, tetrapentylammonium (TPA) and metformin, and inhibitor, quinine, (Figure 3.1) were sketched and energy-minimized using SYBL-X 2.1 (Tripos Force Field, Gasteiger-Hückle charges distance-dependent dielectric constant = 4.0 D/Å) and docked into each of the 100 models within a 15 Å radius of Trp355 (a residue present within the identified binding pocket) using GOLD Suite 5.5. A favorable model was selected based on the combined MODELLER discrete optimized protein energy (DOPE) score, GOLD docking score, and Ramachandran plot results. The DOPE score, accounting for spherical and finite shape of the native structures, helps to determine the quality of the protein models. The GOLD score evaluates the interactions of the docked substrate within the proposed binding pocket(s). Ramachandran plots were

used to help visualize energetically allowed regions for backbone dihedral angles against amino acid residues in the protein structure. A model with more than 90% of amino acids located in the favorable regions of a Ramachandran plot is generally considered an acceptable model. High resolution images were obtained using PyMOL v1.8.and SYBL-X-2.1.

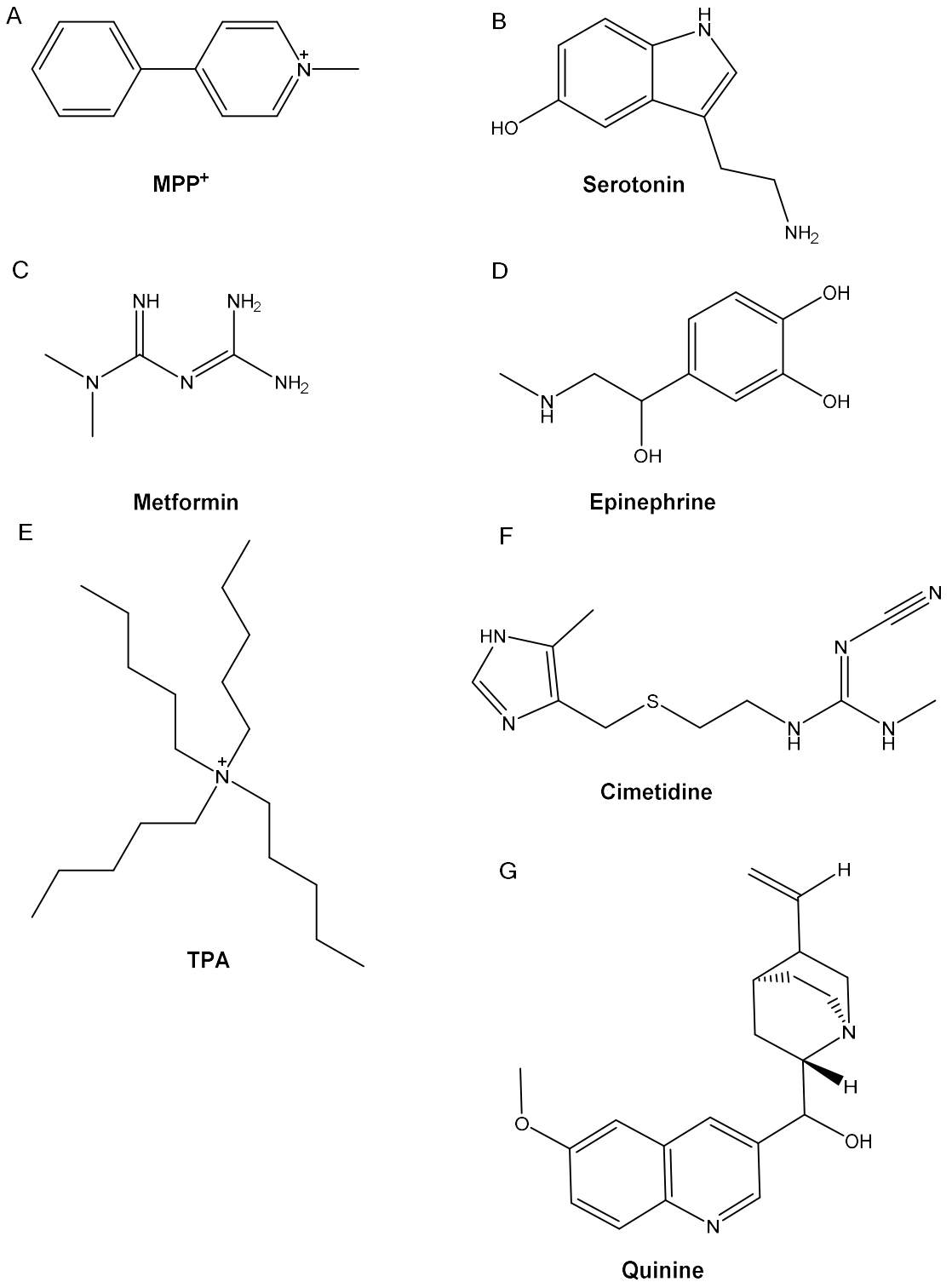


Figure 3.1 Chemical structures of compounds docked into hOCT2 homology models.

3.B.3 Bacterial transformation

Plasmid DNA (pcDNA3-hOCT2) was transformed through the following steps: adding 10 ng of DNA to 50 µL of DH5alpha competent cells, incubating on ice for 30 minutes, and then applying heat shock at 42°C for 20 seconds. The mixture was then added to 950 µL of 37°C preheated LB broth and incubated while shaking (225 rpm) at 37°C for one hour. Afterward, the mixture was plated onto LB agar plates containing ampicillin (0.1 mg/mL) and incubated overnight at 37°C. The following day, colonies were picked and grown overnight (with shaking at 225 rpm) in LB broth with ampicillin (0.1mg/mL) at 37°C. Plasmid DNA extraction was performed using the Qiaprep spin miniprep kit according to the manufacturer's recommendations [154]. Bacterial pellets were resuspended and lysed, followed by the use of spin columns to isolate plasmid DNA and wash/discard any impurities in the flow through. Eluted plasmid DNA from the column was stored at -20°C. Plasmid DNA concentration and purity were determined via UV spectrophotometry.

3.B.4 Point mutation of plasmid DNA

Synthetic oligonucleotide primers containing the desired DNA mutations were designed using the QuikChange Primer Design program (Agilent Technologies) (Table 3.1). Amino acid substitutions were introduced into the hOCT2 coding sequence via site directed mutagenesis (QuikChange Lightning Site-directed Mutagenesis Kit) according to the manufacturer's recommendations. The resulting mutant plasmids were transformed into XL 10-GOLD ultra-competent cells according to the manufacturer's protocol and plated on LB-agar plates with ampicillin (0.1 mg/mL) and incubated overnight at 37°C.

Colonies were picked, purified, and the presence of the desired mutation was then confirmed by DNA sequencing.

Table 3.1 Primers for hOCT2 site directed mutagenesis.

Protein residue	Direction	Mutant oligonucleotide (5'→ 3')
Gln242Glu	Forward	GAA CAG TGG GGA TTT TTT ACG AAG TTG CCT ATA CAG TTG G
	Reverse	CCA ACT GTA TAG GCA ACT TCG TAA AAA ATC CCC ACT GTT C
Gln242Lys	Forward	GAA CAG TGG GGA TTT TTT ACA AAG TTG CCT ATA CAG TTG G
	Reverse	CCA ACT GTA TAG GCA ACT TTG TAA AAA ATC CCC ACT GTT C
Tyr245Phe	Forward	TTT TTA CCA AGT TGC CTT TAC AGT TGG GCT CCT GG
	Reverse	CCA GGA GCC CAA CTG TAA AGG CAA CTT GGT AAA AA
Tyr245Ala	Forward	GAT TTT TTA CCA AGT TGC CGC TAC AGT TGG GCT CCT GGT G
	Reverse	CAC CAG GAG CCC AAC TGT AGC GGC AAC TTG GTA AAA AAT C
Thr246Ser	Forward	TTT ACC AAG TTG CCT ATT CAG TTG GGC TCC TGG T
	Reverse	ACC AGG AGC CCA ACT GAA TAG GCA ACT TGG TAA A
Thr246Lys	Forward	GGA TTT TTT ACC AAG TTG CCT ATA AAG TTG GGC TCC TG
	Reverse	CAG GAG CCC AAC TTT ATA GGC AAC TTG GTA AAA AAT CC
Tyr362Phe	Forward	CAC GAG CTC TGT GCT CTT CCA GGG CCT
	Reverse	AGG CCC TGG AAG AGC ACA GAG CTC GTG
Tyr362Ala	Forward	CAC GAG CTC TGT GCT CGC CCA GGG CCT CAT CAT G

	Reverse	CAT GAT GAG GCC CTG GGC GAG CAC AGA GCT CGT G
Glu448Asp	Forward	GAT CAC AAT GGC CTA TGA TAT AGT CTG CCT GGT CAA T
	Reverse	ATT GAC CAG GCA GAC TAT ATC ATA GGC CAT TGT GAT C
Glu448Ala	Forward	GAT CAC AAT GGC CTA TGC GAT AGT CTG CCT GGT CA
	Reverse	TGA CCA GGC AGA CTA TCG CAT AGG CCA TTG TGA TC

3.B.5 Cell line transfection and maintenance

Mutant transporter expressing CHO cell lines were generated using cationic lipid-based transfection. Briefly, 1µg plasmid DNA was combined with 2 µL Lipofectamine 2000 (Invitrogen), mixed, diluted in 100 µL Opti-MEM (Invitrogen) and applied to CHO cells at 50-60% confluency in 12-well plates (Corning Inc, Corning, NY). Fresh culture medium (DMEM/F12) was applied just prior to the addition of transfection agents. After incubating for 24 hours at 37°C / 5% CO_2, the transfection medium was removed and replaced with fresh medium containing Geneticin (G418; 1 mg/mL) to select for successfully transfected cells for a period of 14-21 days. Cells viable in the presence of G418 were transferred to culture flasks and continued to be maintained under antibiotic selective pressure (250 µg/mL G418).

CHO control, CHO-hOCT2 and CHO-hOCT2 mutant cell lines were maintained in Dulbecco's Modified Eagle's Medium/F12 (DMEM/F12) with 10% FBS, and 1% Penicillin/Streptomycin at 37°C with 5% CO_2 in 25 or 75mm^2 polystyrene flasks. G418 (250µg/mL) was included in the medium for maintaining selective pressure on stably-transfected cell lines. Cells were sub-cultured every 3-4 days and passages 10-40 were used for experiments.

3.B.6 Cell accumulation assays

Mutant functional screening

The procedure for the cell accumulation assay has been described previously [68,69]. Briefly, cells were seeded into 24-well tissue culture plates at a density of 1.5×10^5 cells/well in the absence of antibiotics and cultured for 48 hours. Cells were equilibrated with transport buffer for 10 min (500 µL of Hanks' balanced salt solution containing

10 mM HEPEs, pH 7.4). Equilibration transport buffer was replaced with 400 µL of fresh transport buffer containing 1 µM unlabeled MPP^+ spiked with trace [^{3}H]MPP^+ (0.25 µCi/ml) in the presence or absence of the inhibitor quinine (200 µM). After incubation for 10 minutes, the cells were immediately rinsed 3 times with ice cold transport buffer, lysed with 200 µL 1N NaOH, neutralized with 250 µL 1N HCl and 200 µL 10mM HEPES. The radioactivity in cell lysates was quantified by liquid scintillation counting, and uptake normalized by the total protein content determined by the Bradford method. The intracellular accumulation of substrates was reported as picomoles of substrate per milligram total protein. All uptake data were corrected for background accumulation in corresponding CHO empty vector cells.

Kinetic assays

The Michaelis-Menten constant (K_m) was determined for MPP^+ uptake in each of the generated mutant hOCT2-expressing cell lines via saturation analysis according to our established protocol [156]. The experiment was carried out in the same way as described for the functional screening assay with the exception that the equilibration transport buffer was replaced with 400 µL of fresh transporter buffer containing increasing concentrations (1-200 µM) of unlabeled MPP^+ spiked with [^{3}H]MPP^+ (0.25 µCi/ml) and incubated for a period of 1 minute. After incubation, the cells were immediately rinsed 3 times with ice cold transport buffer and lysed with 1N NaOH, neutralized with 250 µL 1N HCl and 200 µL 20mM HEPES. The K_m estimate, which represents the concentration of substrate at half maximum velocity of the transporter, was calculated using nonlinear regression with the enzyme kinetics model in GraphPad Prism 5.0 (GraphPad Software Inc., San Diego, CA). Individual saturation experiments were repeated at least three times

with duplicate wells and plotted as mean ± SD. K_m estimates were reported as mean ± SE.

3.B.7 Genomic DNA integration confirmation

Cells were suspended in 500 µL lysis buffer [1 M Tris (pH 8.0), 5 M NaCl, 0.5 M EDTA, and 10% SDS] containing proteinase K (0.4 mg/mL) and incubated at 55°C while shaking overnight. Genomic DNA was thoroughly extracted from samples with an equal volume of phenol/chloroform/isoamyl alcohol (25:24:1) after gentle mixing for 10 min, and centrifugation for 10 min at 15,000 g. The upper aqueous phase was carefully collected, isopropanol was added and mixed well, then centrifuged immediately at 15,000 g for 30 min to obtain DNA pellet. The pellet was washed with 70% ethanol, dried, and resuspended with 50 µL TE buffer [10 mM Tris (pH 8.0), and 1 mM EDTA]. Concentration of DNA was determined through UV spectrophotometry. Genomic DNA (2 ng), 2x Go-taq Master Mix (5 µL), as well as 1 µL primer pair mix (T7: 5'- TAATACGACTCACTATAGGG-3; hOCT2-REV: 5'- CCAGTGAGGAAGTGCGTAAG -3') were added together to a final volume of 20 µL and run in a thermocycler: initial denaturation at 95°C for 5 min, followed by 30 cycles of: denaturation at 95°C for 2 min, annealing at 50-52°C for 30 seconds, and elongation at 72°C for 30 seconds. Final elongation step at 72°C for 5 min and held at 4°C. PCR products were loaded into a 1% agarose gel for separation using electrophoresis at 120 V for 60 min and visualized by UV light following ethidium bromide staining.

3.B.8 Cell harvest for immunoblotting

Cell lines were harvested according to the Abcam plasma membrane extraction kit protocol (Abcam, Cambridge, United Kingdom): Briefly, cells were removed by scraping

in phosphate buffered saline (PBS, Gibco/Invitrogen), centrifuged for 5 minutes at 700 x g, washed with ice cold PBS, then resuspended with the homogenization buffer and mixed with a Dounce homogenizer on ice. Afterward, the homogenate was centrifuged at 700 x g for 10 minutes at 4°C. The supernatant was collected and transferred to a new vial and centrifuged at 10,000 x g for 30 minutes at 4°C. Supernatant (cytosolic fraction) was collected and stored at -80°C.

3.B.9 SDS-PAGE and Immunoblotting

The cytosolic and plasma membrane fractions were harvested according to the plasma membrane extraction kit protocol (Abcam). Protein concentration was quantified using the Bradford method. Samples (20 µg) were subjected to sodium dodecyl sulfate-polyacrylamide gel electrophoresis (SDS-PAGE) using the Bio-Rad Mini-PROTEAN system. Samples were separated using 12% polyacrylamide gels at 170V for 1.5 hours and then transferred onto polyvinylidene difluoride (PVDF) membrane (Bio-Rad, Hercules, CA) for 1 hour at 100 mA. Membranes were blocked with 5% BSA in TBST (19 mM Tris base, 137 mM NaCl, 2.7 mM KCl, 0.05% Tween 20, 0.05% sodium azide) for 1 hour. The rabbit anti-OCT2 polyclonal antibody was diluted (1:400) to 2.5 µg/mL in 5% BSA and the blots probed overnight at 4°C with rocking (18 hours). Three 5-minute washes were performed with TBST then alkaline phosphatase conjugated secondary antibody diluted (1:1000) in 5% BSA was added and incubated for 2 hours at room temperature with rocking. Blots were washed three times for 5 minutes with TBST before being developed in 0.1 M Tris, 0.1 M NaCl, 5mM $MgCl_2$ phosphatase buffer (pH 9.4) containing 0.25 mg/ml 5-bromo-4-chloro-3-indolyl phosphate (BCIP, Sigma-Aldrich) and

0.25 mg/ml nitro blue tetrazolium (NBT, Sigma-Aldrich) in the dark. Blots were digitally scanned.

3.B.10 Immunocytochemistry

Cells were prepared for immunostaining by plating 6 x 10^4 cells/ml onto flame sterilized 12 mm cover slips (Fisher Scientific) in 6-well plates (Corning, Inc.) overnight in the absence of antibiotics. Cells (~70% confluent) were washed with PBS, fixed with 4% paraformaldehyde in PBS for 10 minutes, and permeabilized with 0.01% TritonX in PBS. The cells were then washed with 1x PBS followed by blocking with 1% BSA in 1x PBS for 1 hour at room temperature. The rabbit anti-OCT2 primary antibody was diluted (1:100) with 1% BSA in TBST and incubated with the cells at room temperature for 1 hour. Cells were washed three times for 5 minutes with PBS. FITC anti-rabbit secondary antibody was diluted to (1:100) in 1% BSA in TBSTA and applied to the cells for 1 hour at room temperature in the dark. Cells were washed three times for 5 minutes with PBS, placed on slides with DAPI prolong diamond mounting media and imaged with a fluorescence microscope (Olympus I51, Olympus, upper Saucon Township, PA).

3.B.11 Green fluorescent protein (GFP) plasmid construction

To make the hOCT2-GFP fusion construct, the full length hOCT2 cDNA fragment was removed from the isolated library clone, pcDNA3/hOCT2, using the restriction enzymes Kpn I and Xba I. The fragment was gel isolated and ligated into the pEGFP-C1 vector in frame at the carboxyl terminal end of GFP forming the plasmid pEGFP-C1/hOCT2, where “E” denotes “enhanced”. Plasmid construction was performed commercially (GenScript, Picataway, NJ). The lyophilized GFP plasmid construct, was resuspended and diluted in TE pH 8, transformed into DH5-alpha cells and DNA extracted

using the Qiagen miniprep kit. The construct was confirmed by DNA sequencing. Non-functional hOCT2 mutants were reproduced in the hOCT2-GFP construct using the original primers (Table 3.1) and the QuikChange Lightning site-directed mutagenesis kit.

3.B.12 Microscopic imaging

An Olympus IX-70 inverted microscope fit with a 12-bit camera (Olympus, Melville, NY) was used in order to capture phase contrast and fluorescent images. Fluorescent images were taken with two second exposures using a 595 nm dichroic long pass filter (Chroma, Rockingham, VT) illuminated by a mercury arc lamp. The images were processed using Olympus Microsuite v.5. Confocal fluorescent images were obtained at the VCU Microscope Core facility using a Zeiss LSM 710 Axio Observer inverted laser scanning confocal microscope fit with a 63x oil immersion objective. Images were collected by illuminating samples with a blue diode laser at 405 nm. Images were processed using Zeiss ZEN 2 Blue edition software (Oberkochen, Germany).

3.B.13 Statistics

The data plots were presented as means ± SD. Dose response curve (K_m estimate) data were reported as mean ± SE for at least n = 3. K_m estimates were fit based on the equation: $V_0 = V_{max} * [S] / (K_m + [S])$. One-way ANOVA with post-hoc Dunnett's test was used to evaluate differences compared to a single control where indicated. Statistical calculations were performed using Prism 5.0 (GraphPad Software, Inc., San Diego, CA). A difference was deemed statistically significant if $p < 0.05$.

3.C RESULTS

3.C.1 Identification of a hOCT2 model

The hOCT2 peptide sequence (Uniprot ID: O15244) was aligned with the PiPT template sequence (PDB ID: 4J05) (Figure 3.2) as input for the program MODELLER to generate 100 initial hOCT2 homology models. Analysis of the initial 100 models identified a single large cavity in the central region of the transporter as a potential binding pocket. MPP^+ was subsequently docked in this region. After docking MPP^+ into the generated hOCT2 models, the most favorable interaction model was selected based on three main criteria: GOLD docking score, DOPE score, and the total number of clusters.

The genetic optimized ligand docking (GOLD) scoring is essentially a method to quantify which poses generated for a particular ligand are most likely to occur based on the interactions present within the transporter. GOLD scores for the top ten most favorable docked poses of MPP^+ in the binding pocket of the hOCT2 models (ranging from 58.49 to 66.59) were ranked (Table 3.2). Amongst this select group, the top three model's GOLD scores had a difference of 0.77 between them, thus were considered to be virtually identical. The difference between the top and fourth ranked model was increasingly larger (1.61). The discrete optimized protein energy (DOPE) score accounts for the shape of native structures which in turn helps to evaluate the quality of the whole protein structure. The DOPE scores for the top ten models ranged between -48,186 and -47,268 (Table 3.2). Additionally, the number of homology models which contained a given substrate pose (number of clusters) was also accounted for in model selection. The greater the number of models that have a particular substrate pose docked, the higher the likelihood that the specific pose occurs within the binding pocket. Out of the top 10

models, models 30 and 64 had 6 clusters, while the rest had 4 or less. Among the top three ranked GOLD score models, model 64 stood out as having the lowest DOPE score (-48,030; second lowest DOPE score overall) in conjunction with the highest number of clusters (6). Taken together, these three selection criteria indicated model 64 as the most favorable docked model and thus it was selected for subsequent studies. The generated tertiary structure for model 64 with MPP^+ docked in the hypothesized binding pocket is shown in Figure 3.3. The docked hOCT2 model shows MPP^+ residing inside a large central cavity of the 12-membrane spanning alpha helical domains (Figure 3.3).

Ramachandran plots were utilized as a method for determining and visualizing "allowed regions" for the backbone dihedral angles that make up amino acids in the generated model. For the amino acids that made up our selected hOCT2 model, 91.4% were in the most favored regions, 6.1% were in the additionally allowed region, and only 2.4% were in the generously allowed and disallowed regions combined (Figure 3.4). The most favored regions category was > 90%, thus supporting the selected hOCT2 model as acceptable.

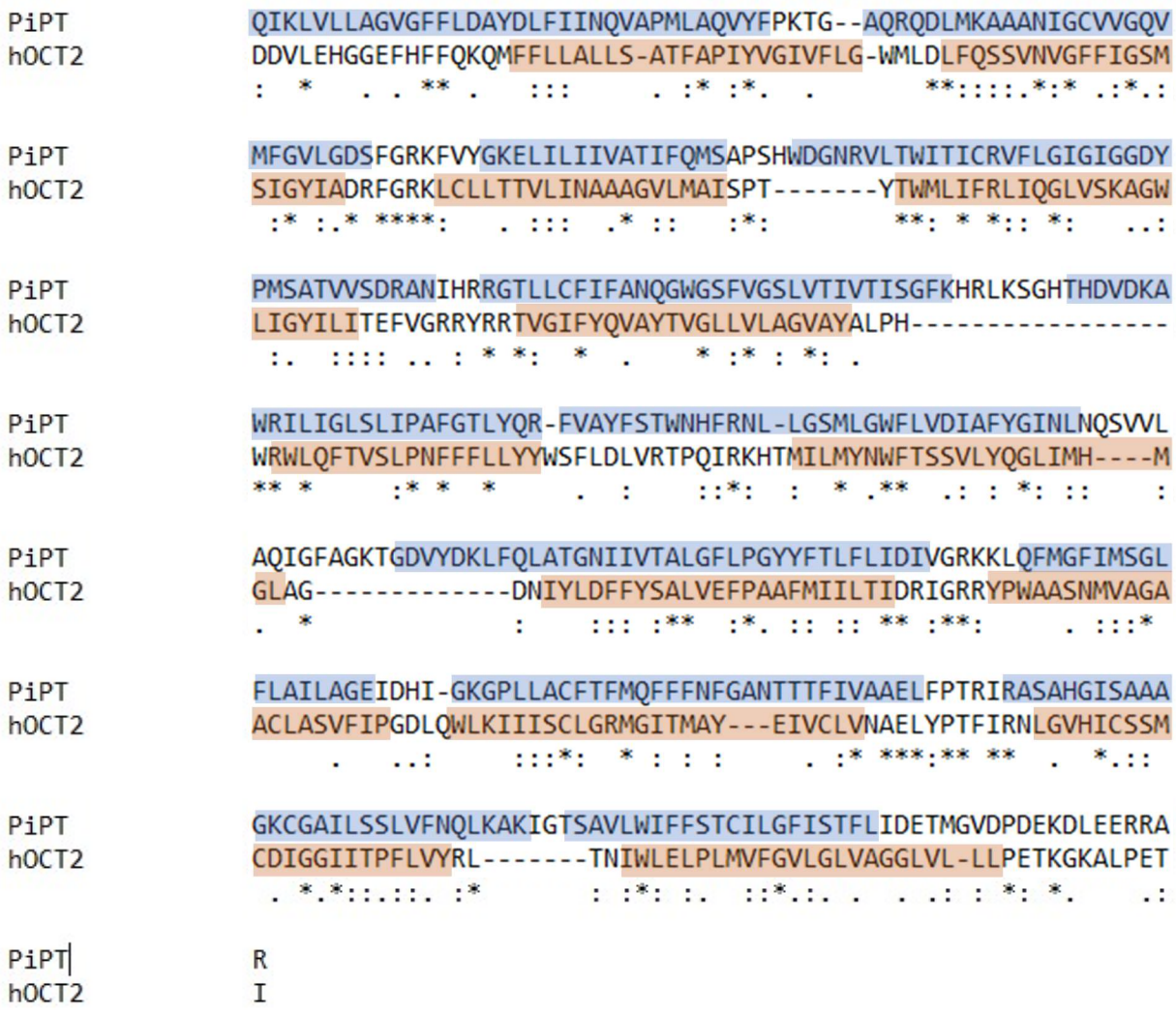


Figure 3.2 Sequence alignment of PiPT and hOCT2.

The alignment was constructed with ClustalX, followed by manually refining gaps based on the transmembrane regions observed in the PiPT crystal structure and predicted for hOCT2 using Phobius, a topology prediction algorithm. Residues forming the large extracellular and intracellular loop between transmembrane domain 1 and 2 and intracellular loop between 6 and 7 of PiPT and hOCT2. The transmembrane domains in the hOCT2 model (red) and PiPT tertiary structure (blue) are highlighted. “*” indicates exact sequence match, “:” indicates high sequence similarity, “.” indicates low sequence similarity

Table 3.2 Summary of hOCT2 model evaluation scores.

GOLD Rank	Model ID	Gold score	DOPE Score	No. of Clusters
1	24	66.59	-47676.04688	2
2	12	66.52	-47487.76953	2
3	64	65.82	-48030.84375	6
4	47	64.98	-47691.90625	3
5	2	64.1	-47665.14453	1
6	30	62.73	-47813.59766	6
7	95	61.53	-47268.98438	4
8	100	60.53	-48186.85547	3
9	55	59.64	-47915.82422	4
10	71	58.49	-47584.00781	1

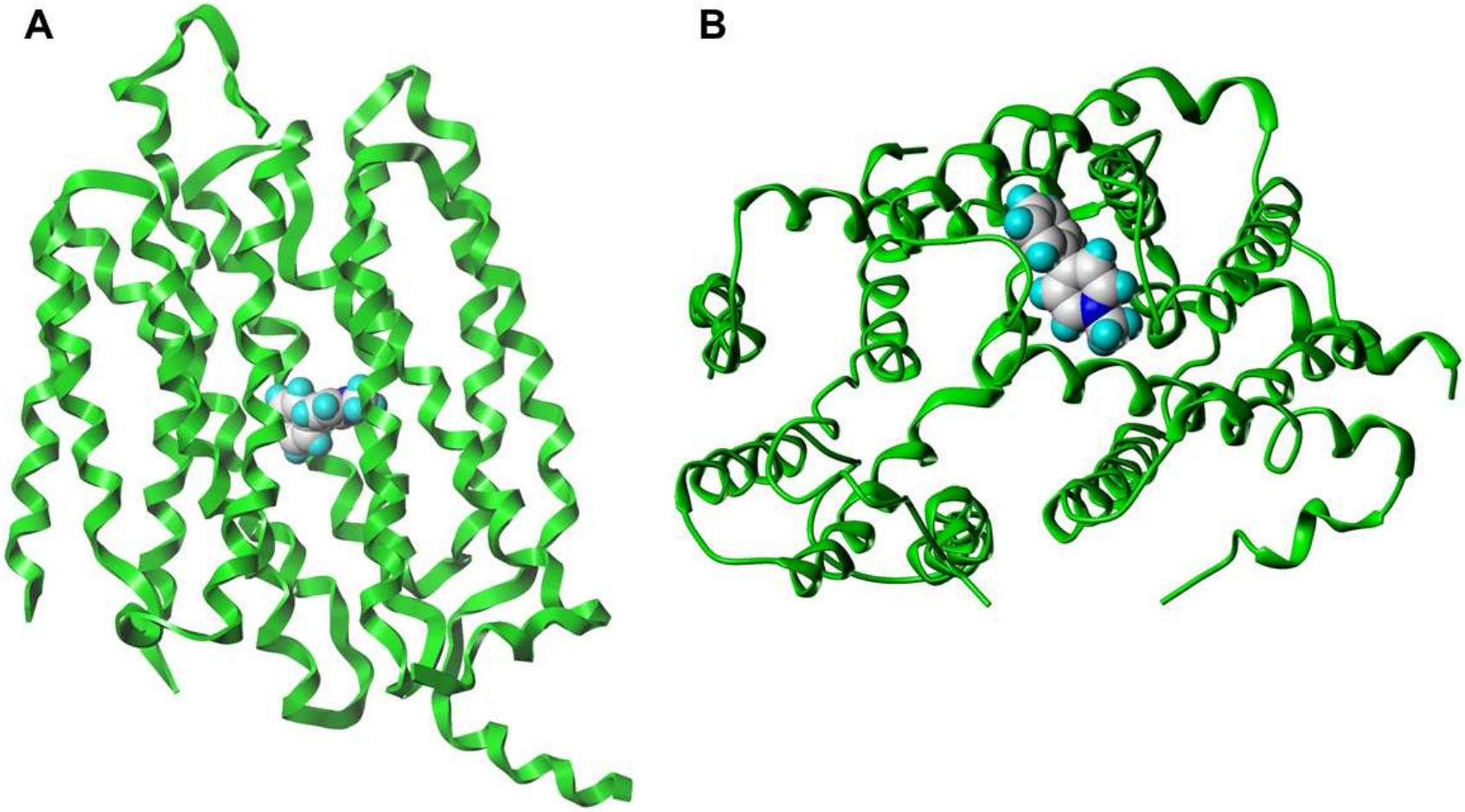


Figure 3.3 hOCT2 homology model.

The generated 3-D molecular structure of hOCT2 (ribbons) is shown with MPP^+ (space-filled) positioned in the putative binding pocket viewed from (A) profile and (B) top-down angles.

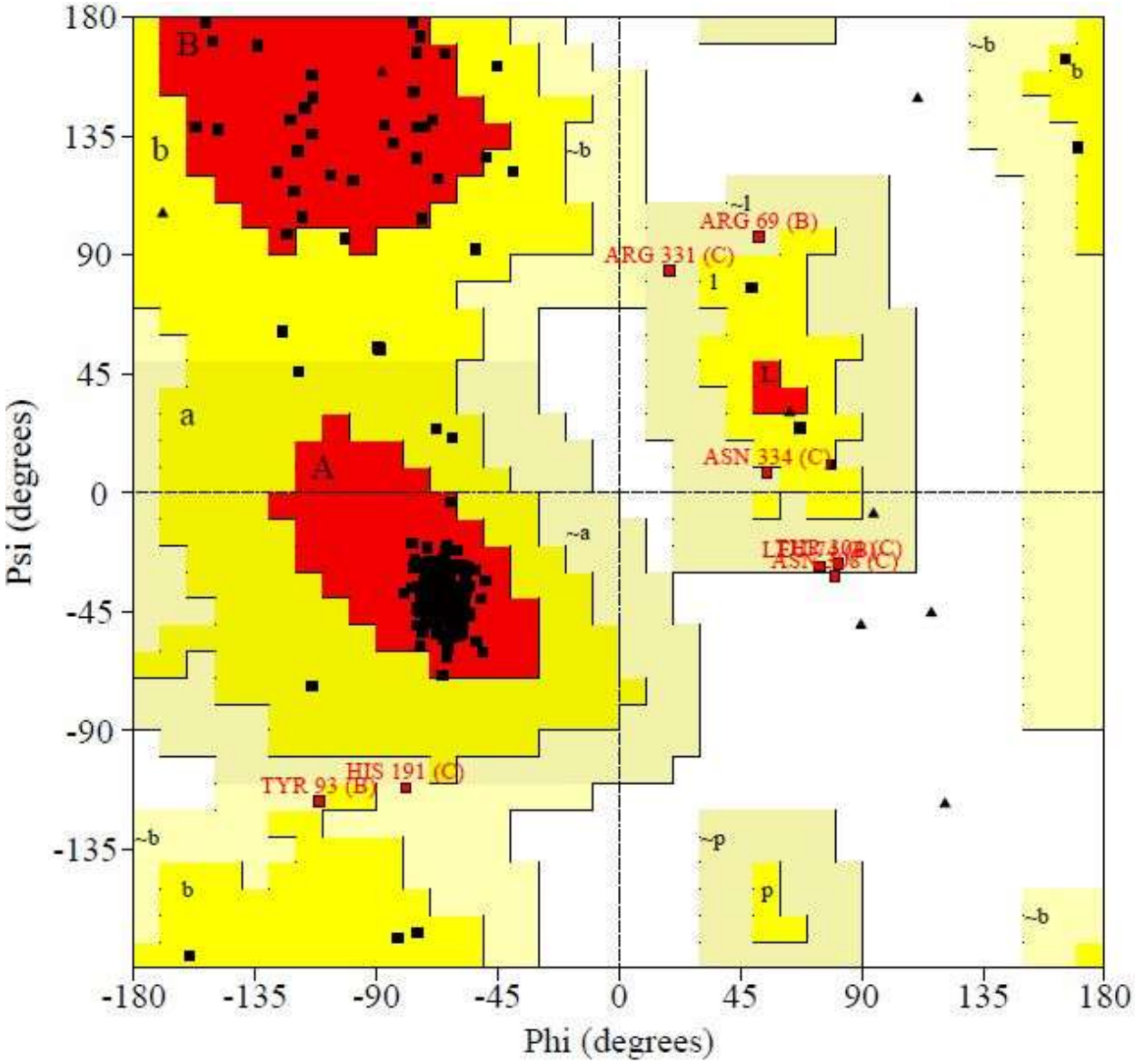


Figure 3.4 Ramachandran plot for hOCT2 homology model.

Phi and psi indicate backbone conformation dihedral angles of amino acid residues, representing the rotations of a polypeptide main chain N-Cα and Cα-C bonds. Amino acids are displayed in different regions: most favored region (red), additional allowed region (yellow), generously allowed region (light yellow), and disallowed region (white). Residues depicted in red squares are in the generously allowed and disallowed regions.

3.C.2 Identifying amino acid residues important for MPP^+ hOCT2 interaction

Several amino acids were identified that made up the binding pocket (within the designated 5 Å radius of the substrate) for docked MPP^+ in the selected hOCT2 model. The identified amino acid residues were found in several different TMDs that came together in the central area forming a large distinct cavity of the transporter—TMD 1: Phe17; TMD 5: Ile239, Gln242, Val243, Tyr245, Thr246, Val247, Leu249; TMD 7: Trp355, Ser358, Ser359, Tyr362, Gln363, Gln387; TMD 8: Gln387, Phe388, Ala391, Ile394; TMD 10: Trp407, Met445, Ala446, Tyr447, Glu448, Val450, Cys451 (Figure 3.5). Within the proposed binding pocket, five amino acids were identified (Gln242, Tyr245, Thr246, Tyr362, and Glu448) as potential candidates critical for transporter-MPP^+ binding interactions. Hydrophobic interactions were found between MPP^+ and amino acid residues Gln242, Thr246, and Glu448, and one of the aromatic rings of MPP^+ was recognized as forming edge-face-pi and pi-stacking interactions with Tyr245 and Tyr362, respectively (Figure 3.6 and Table 3.3).

To further evaluate the generated *in silico* hOCT2 model, known substrates with disparate structures were optimized and docked into the population of 100 models to determine the presence of alternative and/or additional critical amino acid residues in the binding pocket(s). The process involved with selecting the most favorable model for MPP+, was repeated for each docked substrate. Amino acids identified with the greatest overlap across the different docked compounds were Tyr245, Ser358, Tyr362, and Glu448 (Figure 3.7 and Table 3.3). There were several amino acids identified that were also unique to particular compounds including Thr246 for MPP^+; Gln363, Gln387 and Cys451, for serotonin; Cys474 for TPA; and Asp475 for cimetidine.

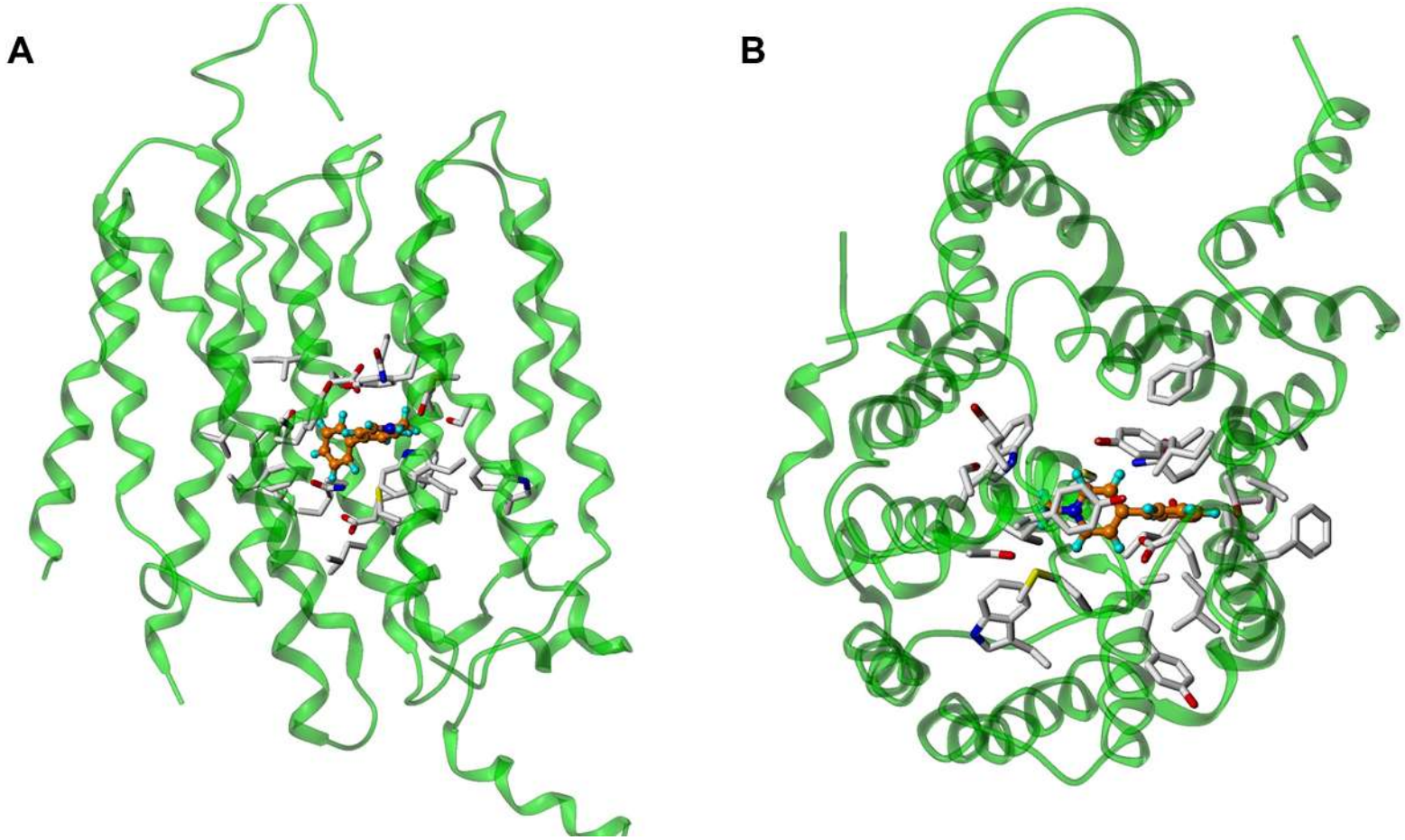


Figure 3.5 3-D rendering of putative binding pocket of hOCT2 with docked MPP^+.

Amino acid side chains (white) comprising the binding pocket surrounding the substrate MPP^+ (orange) is shown viewed from (A) profile and (B) top-down angles.

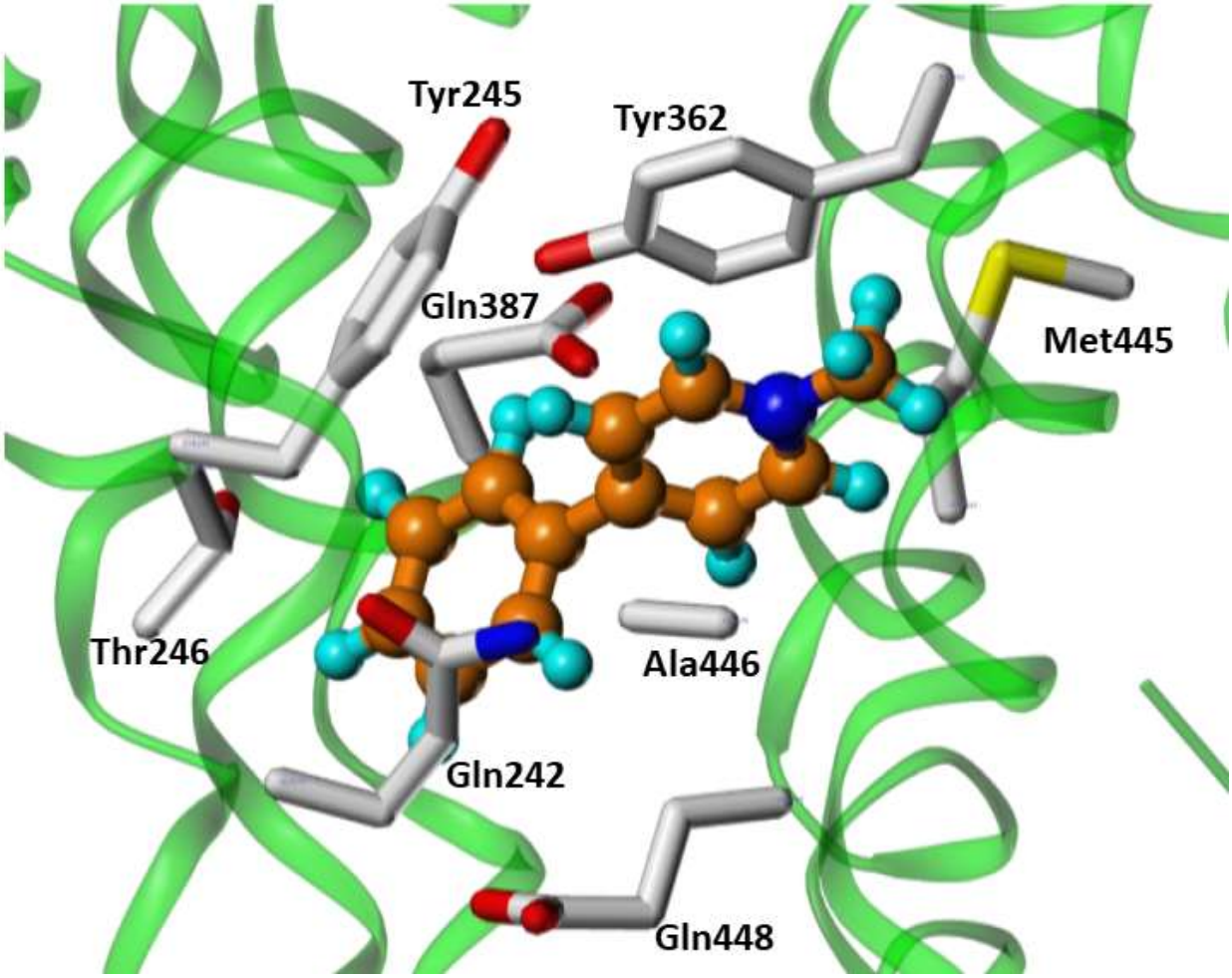


Figure 3.6 Structure of hOCT2 with MPP^+ docked.

The docked substrate (MPP^+, orange) and the amino acids (white side chains) is shown localized in the predicted substrate binding pocket of hOCT2.

Table 3.3 hOCT2 docking interaction summary.

Substrate	Amino Acid	Sequence position	Bond Interaction	TMD
MPP^+	Gln	242	Hydrophobic	5
	Tyr	245	Hydrophobic/Edge-Face Pi	5
	Thr	246	Hydrophobic	5
	Tyr	362	Pi-stack	7
	Glu	448	Hydrophobic	10
Cimetidine	Asn	157	H-bond	2
	Tyr	245	Hydrophobic	5
	Ser	358	H-bond	7
	Tyr	362	Pi-stacking	7
	Glu	448	H-bond (salt bridge)	10
	Asp	475	H-bond (salt bridge)	11
Epinephrine	Tyr	245	Hydrophobic	5
	Ser	358	H-bond	7
	Tyr	362	Pi-stack	7
	Glu	448	H-bond (salt bridge)	10
Metformin	Ser	358	H-bond	7
	Tyr	362	Pi-stack	7
	Glu	448	H-bond (salt bridge)	10
Quinine	Phe	24	Hydrophobic	1
	Asn	157	H-bond (weak)	2

	Phe	160	Hydrophobic	2
	Gln	242	H-bond	5
	Tyr	245	Hydrophobic	5
	Tyr	362	Pi-stacking	7
Serotonin	Tyr	245	Hydrophobic	5
	Ser	358	H-bond	7
	Tyr	362	Pi-stack	7
	Gln	363	H-bond	7
	Glu	387	H-bond (salt bridge)	8
	Glu	448	H-bond (salt bridge)	10
	Cys	451	H-bond	10
TPA	Phe	24	Hydrophobic	1
	Phe	160	Hydrophobic	2
	Tyr	245	Hydrophobic	5
	Cys	474	Hydrophobic	11

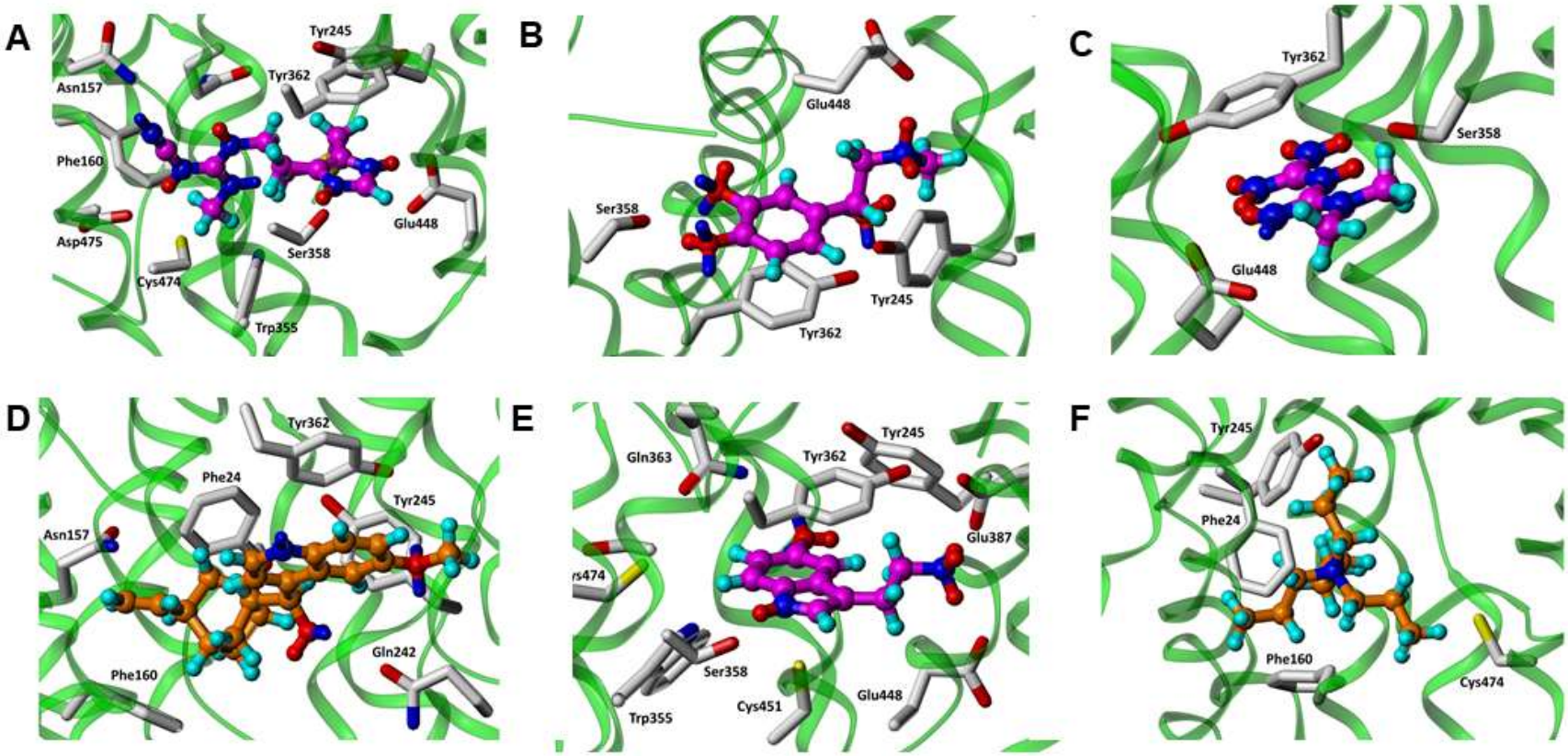


Figure 3.7 Known hOCT2 substrates docked into hOCT2 homology model.

Known hOCT2 substrates (purple or orange) (A) cimetidine, (B) epinephrine, (C) metformin, (D) quinine, (E) serotonin, and (F) TPA, were docked into their respective favorable hOCT2 models. Proposed interactions of interactions are summarized in Table 3.3.

3.C.3 Substitution of hOCT2 amino acid residues in putative binding pocket

We investigated the role of the predicted amino acids in hOCT2-MPP^+ interactions through conservative and non-conservative amino acid substitutions introduced into the hOCT2 coding sequence to evaluate potential changes in hOCT2 function and affinity for MPP^+. The pcDNA3/hOCT2 plasmid vector map is shown in Figure 3.8. The rationale for deciding each conservative and non-conservative amino acid substitution was based on a scheme developed by Bordo *et al.* which categorizes roughly equivalent amino acid residues based on their physicochemical properties of their side chains (Figure 3.9) [157]. Substitutions for residues deemed critical were Gln242Glu, Tyr245Phe, Thr246Ser, Tyr362Phe, and Glu448Asp (conservative); and Gln242Lys, Tyr245Ala, Thre246Lys, Tyr362Ala, and Glu448Ala (non-conservative) (Tables 3.4, 3.5 and 3.6). All hOCT2 mutants were confirmed by DNA sequencing prior to generating stable cell lines. Figure 3.10, depicts a representative DNA-oligonucleotide duplex and sequencing chromatogram in which TAC, coding for Tyr362 in wildtype hOCT2, was changed to TTC, coding for the hOCT2 mutant Tyr362Phe.

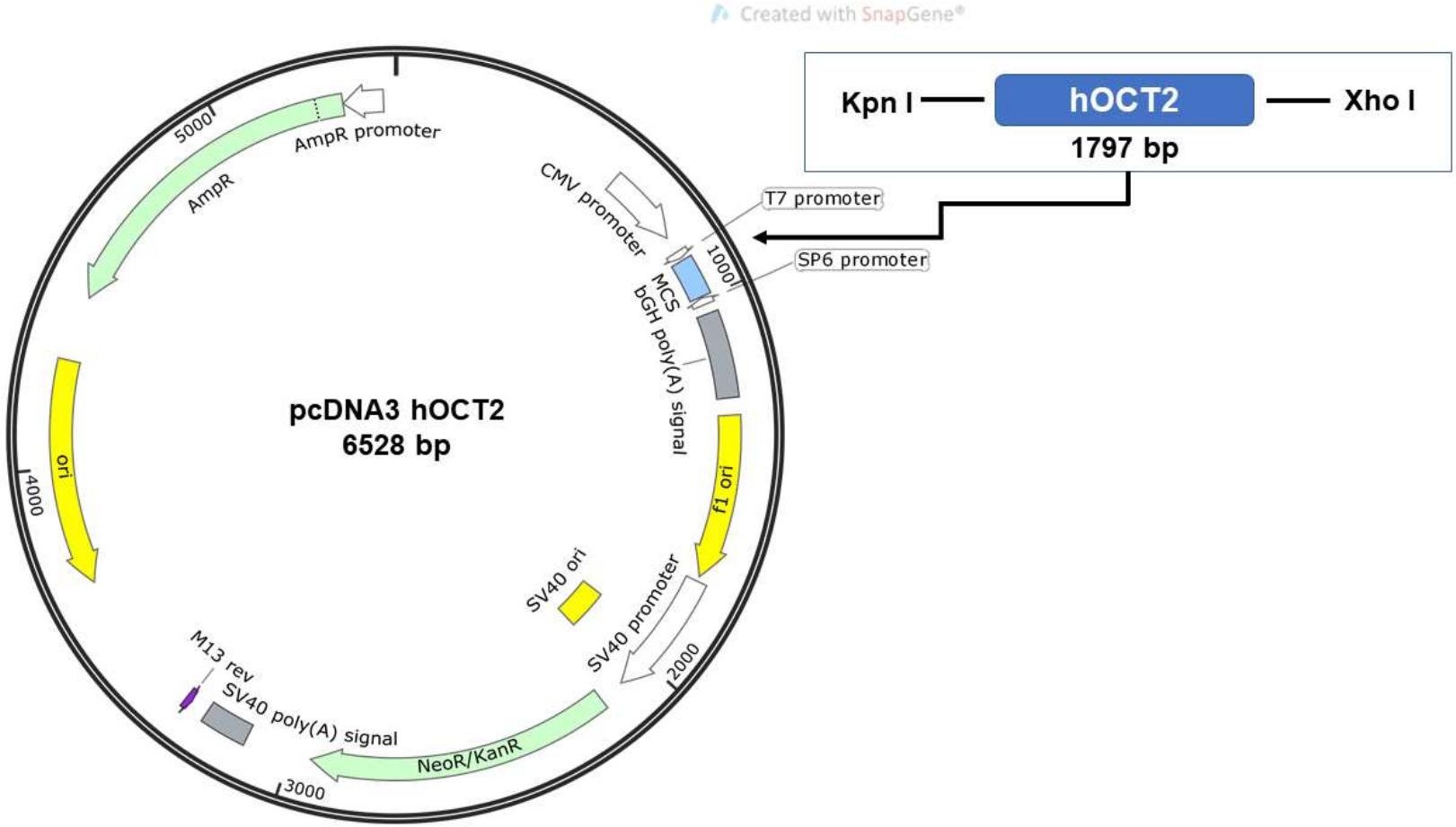


Figure 3.8 pcDNA3/hOCT2 vector map.

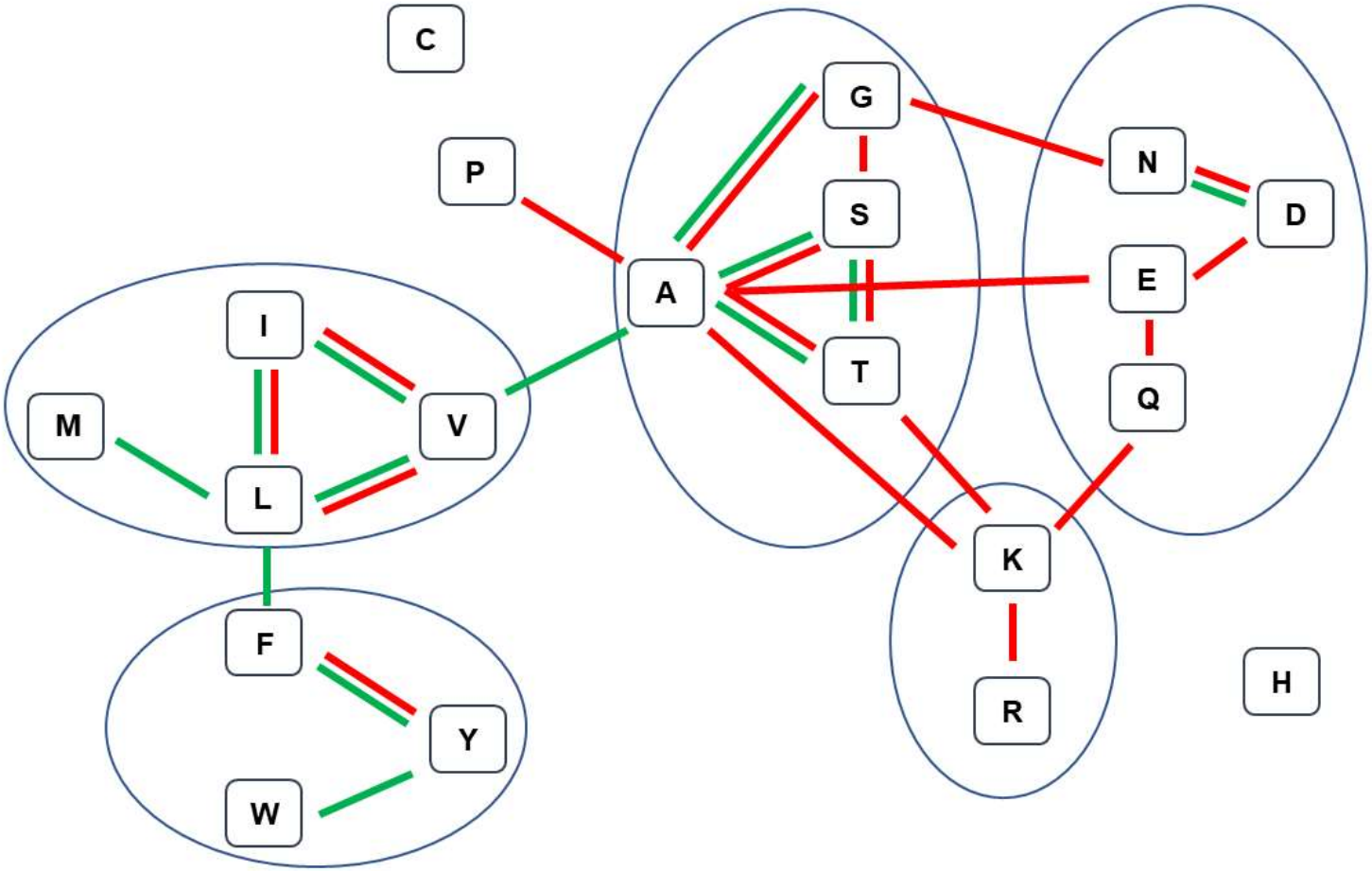


Figure 3.9 Suggested guidance for amino acid residue conservative substitution.

Roughly equivalent amino acid residues categorized based on physiochemical properties into five subgroups.

Diagram is an adapted figure from reference [157]

Table 3.4 Summary of hOCT2 residue substitutions.

	Substitution	
Residue	**Conservative**	**Non-Conservative**
Gln242	Glu	Lys
Tyr245	Phe	Ala
Thr246	Ser	Lys
Tyr362	Phe	Ala
Glu448	Asp	Ala

Table 3.5 hOCT2-MPP$^+$ interaction based conservative substitutions.

Amino Acid	Sequence position	Codon	Mutant Codon	Substitution
Gln	242	CAA	GAA	Gln → Glu
Tyr	245	TAT	TTT	Tyr → Phe
Thr	246	ACA	TCA	Thr → Ser
Tyr	362	TAC	TTC	Tyr → Phe
Glu	448	GAG	GAC	Glu → Asp

Table 3.6 hOCT2-MPP$^+$ interaction based non-conservative substitutions.

Amino Acid	Sequence position	Codon	Mutant Codon	Substitution
Gln	242	CAA	AAA	Gln → Lys
Tyr	245	TAT	GCT	Tyr → Ala
Thr	246	ACA	AAA	Thr → Lys
Tyr	362	TAC	GCC	Tyr → Ala
Glu	448	GAG	GCG	Glu → Ala

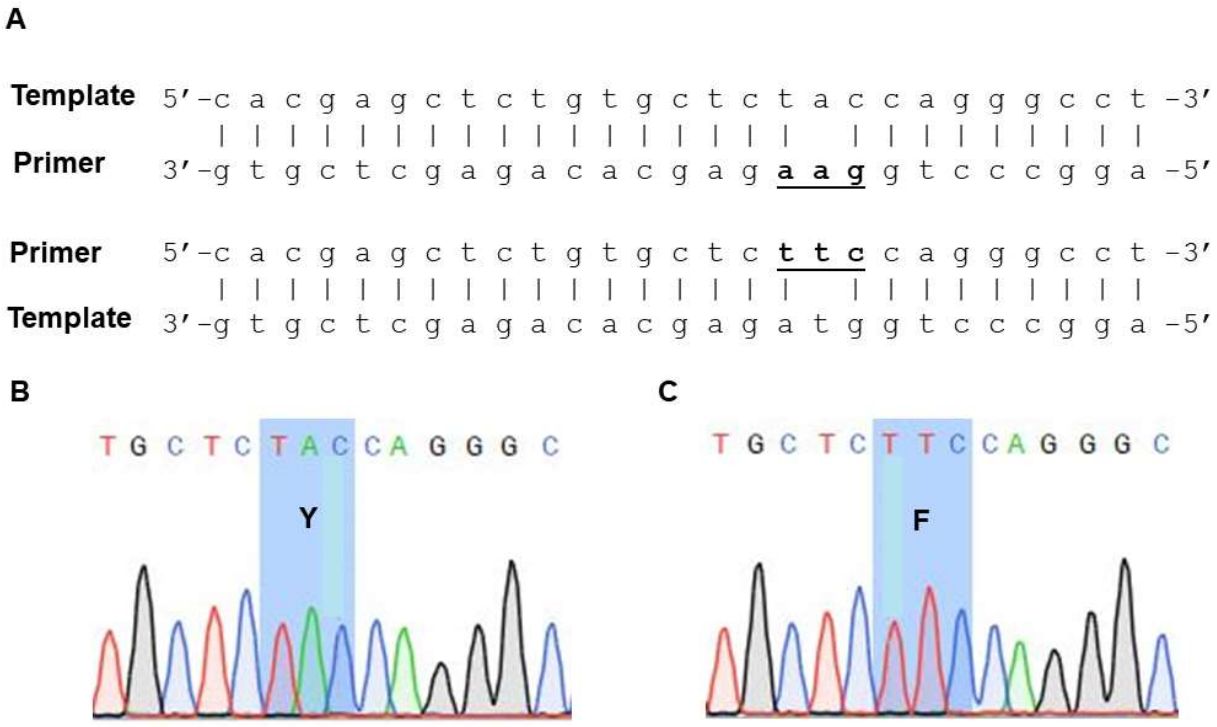


Figure 3.10 Representative sequencing chromatogram for hOCT2 mutants.
(A) DNA template-primer duplex for hOCT2 Y362F. Chromatogram for (B) hOCT2 wildtype and (C) hOCT2 Y362F are shown with triplet codon corresponding to mutation site highlighted.

3.C.4 Critical amino acid confirmation through kinetic assays

In functional screening assays evaluating [^{3}H] MPP^+ transport (Figure 3.11), wild-type hOCT2 demonstrated a 4.5-fold higher uptake of MPP^+ compared to mock expressing (pcDNA3) background control cells (15.7 ± 0.4 pmol mg protein^{-1} 10 min^{-1} vs. 3.5 ± 2.7 pmol mg protein^{-1} 10 min^{-1}). Quinine (200 μM), a known inhibitor for OCTs, virtually abolished hOCT2 mediated MPP^+ transport. Two non-conservative mutants, hOCT2 Glu242Lys and Tyr362Ala, and one conservative mutant, hOCT2 Tyr362Phe, resulted in a complete loss of MPP^+ transport activity (Figure 3.11). All other mutants retained some level of transport activity and were subjected to saturation analysis in order to estimate K_m (Figure 3.12, Table 3.7).

The affinity of MPP^+ determined for wildtype hOCT2 was comparable to values in prior studies (K_m = 19.7 ± 3.4) [158]. When comparing the K_m estimates for hOCT2 mutants against wildtype hOCT2, only the non-conservative substitution Tyr245Ala resulted in a significant change in affinity for MPP^+. The mutants Gln242Glu, Tyr245Phe, Thr246Ser, Thr246Lys, Glu448Asp, Glu448Ala, and Asp475Glu all demonstrated no significant change in affinity for MPP^+.

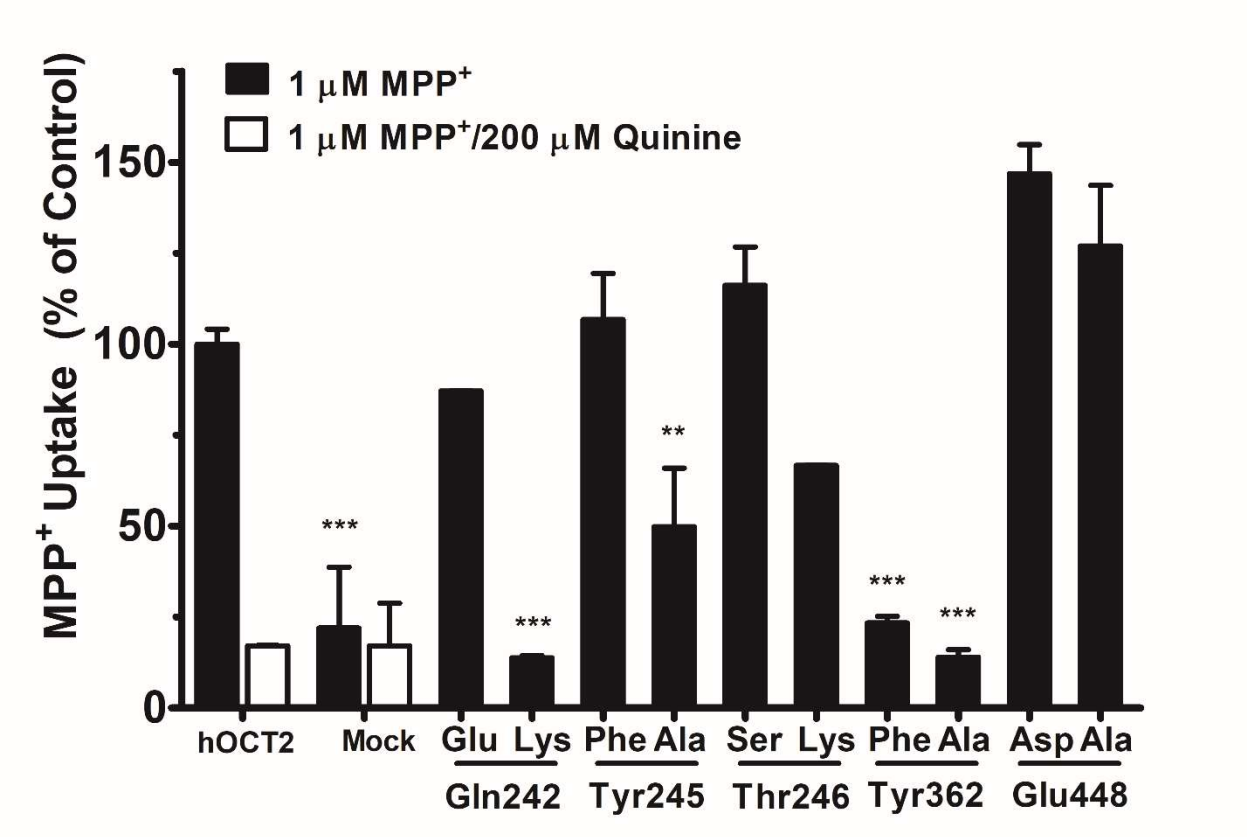


Figure 3.11 Functional screen of CHO-hOCT2 wild type and mutant expressing cell lines.

CHO cells were treated with transport buffer containing 1 μM [^{3}H] MPP$^+$ (0.25 μCi/mL) in the absence or presence of inhibitor (quinine) for 10 min. Conservative and non-conservative mutations appear above original amino acid position. Data shown as duplicate wells ± SD. ** denotes $p<0.01$; *** denotes $p<0.001$; compared against wild type control by one-way ANOVA followed by post-hoc Dunnett's t-test.

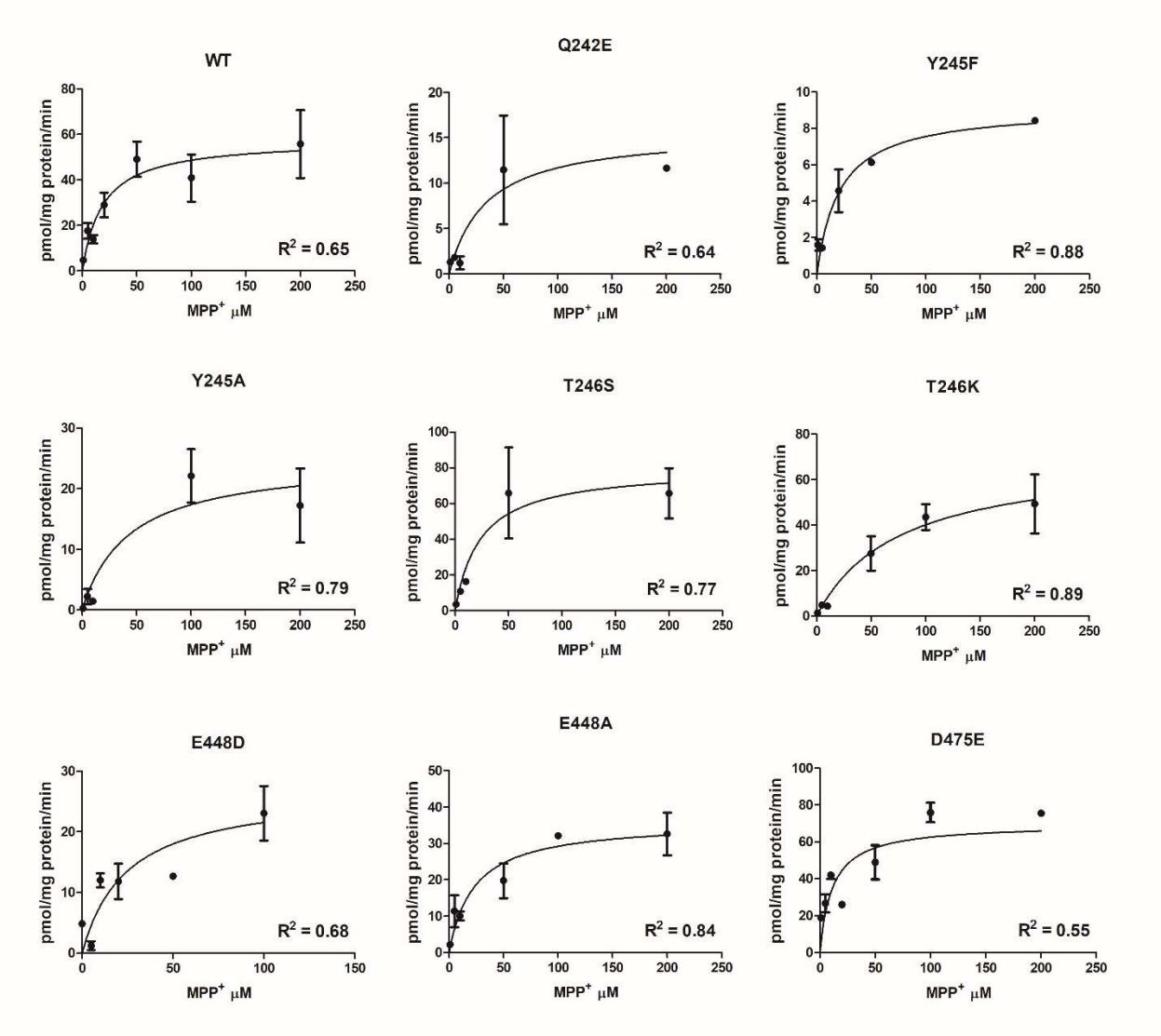


Figure 3.12 Representative dose response curves for wild type and mutant hOCT2.

Michaelis-Menten kinetics of [^{3}H] MPP$^+$ transport (1–200 μM) for hOCT2 and hOCT2 mutants in stably transfected CHO cells.

Table 3.7 Summary of K_m estimates for hOCT2 constructs.

hOCT2 Transporter	K_m (μM)
WT	19.7 ± 3.4
Gln242Glu	31.9 ± 6.2
Tyr245Phe	22 ± 7.5
Tyr245Ala	36.5 ± 5*
Thr246Ser	15.5 ± 2.8
Thr246Lys	27.4 ± 12.3
Glu448Asp	17.9 ± 3.6
Glu448Ala	17.2 ± 3.8
Asp475Glu	13.5 ± 4

Mean K_m estimates acquired from at least 3 experiments ± SE.
* denotes $p < 0.05$ compared against wild type control by one-way ANOVA followed by post-hoc Dunnett's t-test.

3.C.5 Genomic integration of non-functional hOCT2 mutant constructs

To eliminate failed genomic DNA integration as an explanation for the lack of transport activity in non-functional hOCT2 mutants, genomic DNA was extracted and PCR amplified using the primers T7 and hOCT2 REV, that flanked 5' and 3' ends of the hOCT2 coding sequence of the pcDNA3 plasmid (hOCT2 amplicon ~1.8 kb). PCR products of the expected size (~1.8 kb) were obtained for wildtype hOCT2 and all hOCT2 mutants (Gln242Lys, Tyr362Phe, and Tyr362Ala), while no product was observed for negative controls (water and pcDNA3) demonstrating that all hOCT2 plasmids had been successfully integrated (Figure 3.13).

3.C.6 Immunodetection of non-functional hOCT2 mutants

To investigate the translation and membrane targeting for hOCT2 mutants that failed to demonstrate MPP^+ transport, Western blotting was performed on isolated cytoplasmic and plasma membrane fractions from each mutant-expressing cell line using hOCT2 polyclonal antibody (Figure 3.14). Protein bands were observed at the expected position for wildtype hOCT2 (~62 kD), however, a similar band was also seen for CHO empty vector membrane fraction. Detection for β-actin was consistently observed (~43 kD) in all experiments (Figure 3.14).

An alternative method for evaluating membrane targeting of non-functional hOCT2 mutants was pursued. The same antibodies used to probe for hOCT2 in earlier Western blot studies were also used for immunocytochemistry experiments. Cells expressing wildtype pcDNA3/hOCT2 constructs showed strong cytosolic fluorescence for both actin and hOCT2 staining, with no detectable signal in the nucleus (Figure 3.15). Strong

membrane localization, however, was not present in any of the observed cells. Control transfections (lipofectamine only) showed no fluorescent signal (data not shown).

3.C.7 Membrane targeting of hOCT2-GFP fusion construct

The full length hOCT2 cDNA fragment was gel isolated and ligated into vector pEGFP-C1 forming the plasmid pEGFP-C1/hOCT2 containing hOCT2 fused in frame to the carboxyl terminal of GFP (Figure 3.16). CHO cells expressing the hOCT2-GFP fusion construct showed strong fluorescence within the cytosol and lack of signal in the nucleus (Figure 3.17). This pattern is consistent with an intact GFP fusion construct versus expression of “free” GFP. However, no noticeable fluorescence at the plasma membrane was observed. Control transfections (lipofectamine only) showed no fluorescent signal (data not shown). In order to have a reference of the membrane localization of OCTs, MDCK cells stably transfected with a rat Oct2-GFP fusion construct from a previous study were grown and observed [159] (Figure 3.18).

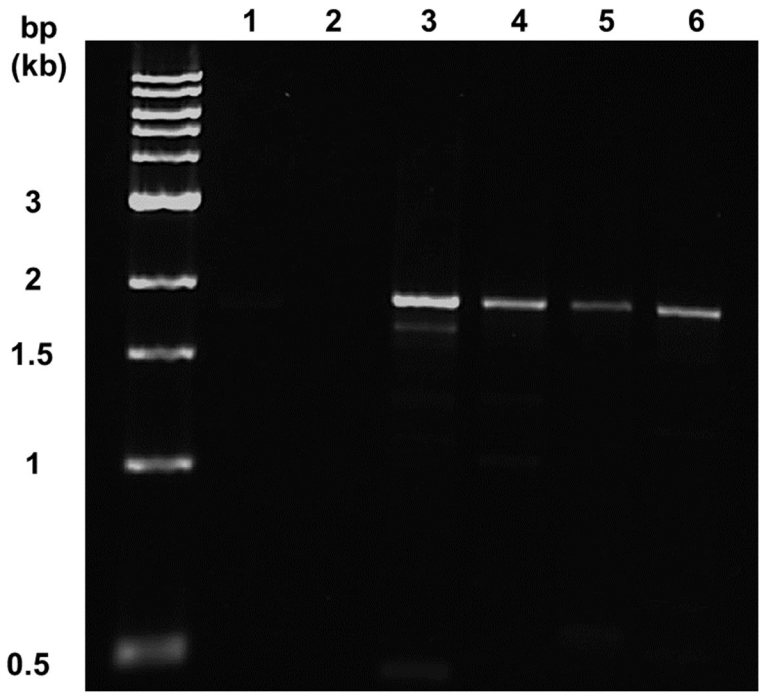


Figure 3.13 PCR analysis of genomic DNA isolated from hOCT2 cell lines.

Confirmation of successful genomic integration of mutant hOCT2 constructs that lacked transport activity. Lanes: (1) water, (2) pcDNA3, (3) hOCT2, (4) hOCT2 Gln242Lys, (5) hOCT2 Tyr362Phe, and (6) hOCT2 Tyr362Ala.

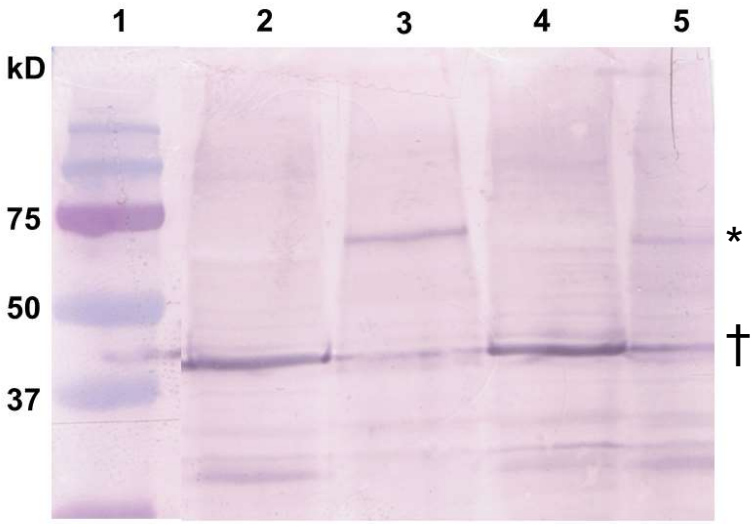


Figure 3.14 Western blot of CHO cell lysates probing for hOCT2.

Lanes: (1) Protein size standard, (2) mock cytosolic fraction, (3) mock membrane fraction, (4) hOCT2 cytosolic fraction, (5) hOCT2 membrane fraction.
†, denotes actin; *, denotes expected hOCT2 size.

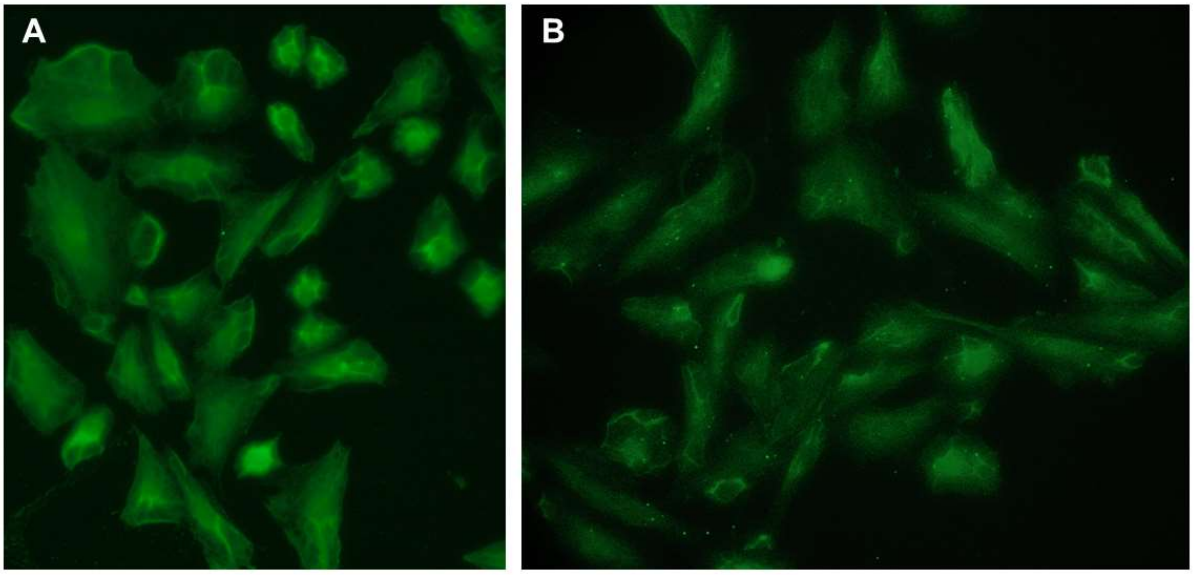


Figure 3.15 Immunocytochemistry of CHO-hOCT2.

CHO cells expressing hOCT2 were probed with anti-actin (A) or anti-hOCT2 (B) antibodies followed by FITC conjugated secondary antibody and observed under fluorescent microscopy (40x magnification).

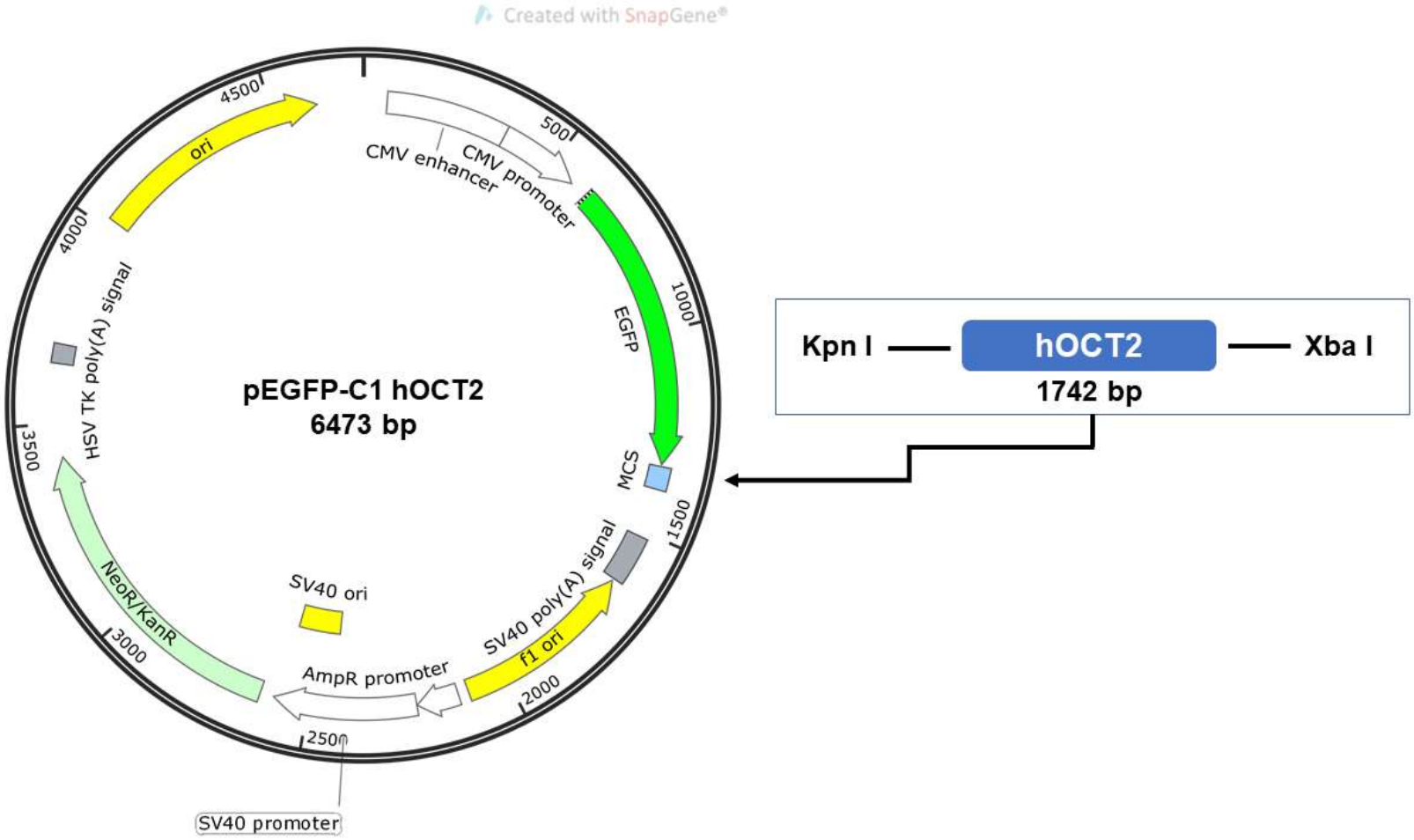


Figure 3.16 pEGFP-C1/hOCT2 fusion protein vector map.

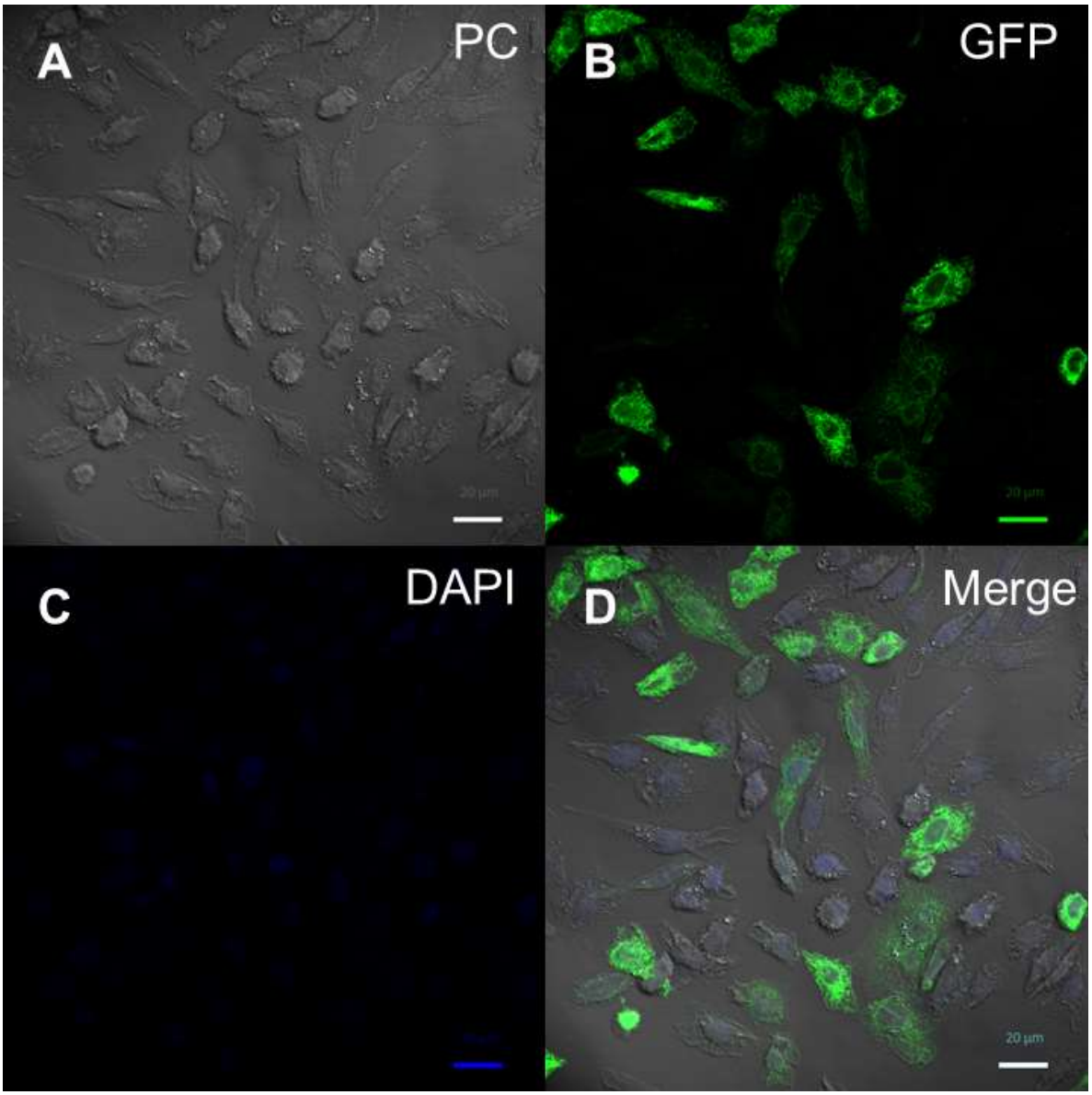


Figure 3.17 Expression patterns of pEGFP-C1/hOCT2.

CHO cells transfected with pEGFP-C1/hOCT2 were fixed, permeabilized, and mounted at 24 hours post transfection then viewed under confocal microscopy: (A) phase contrast, (B) GFP, (C) DAPI, and (D) merge. Scale bar = 20 µm

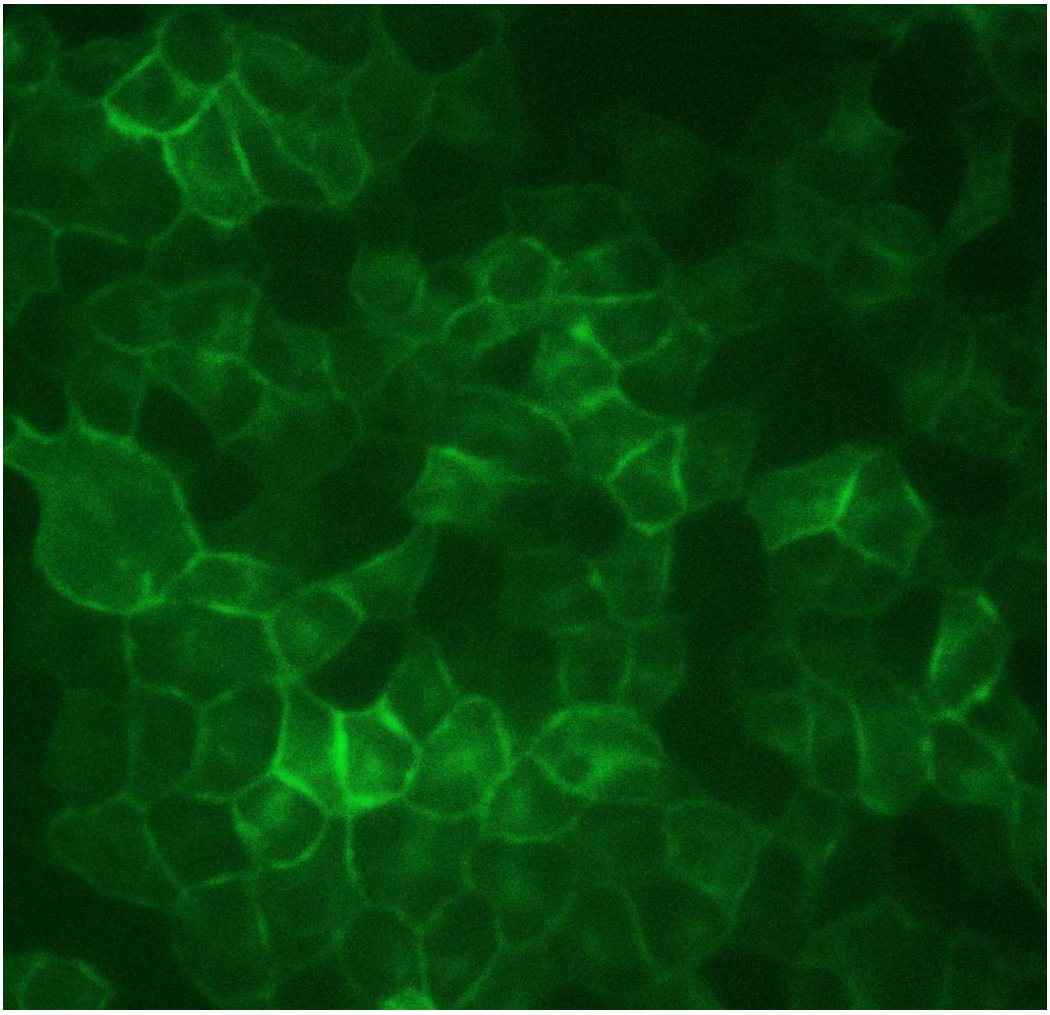


Figure 3.18 Expression of pEGFP-C3/rOct2 in MDCK cells.

MDCK cells stably transfected with pEGFP-C3/rOct2 were thawed, grown in culture for 48 hours, then observed by fluorescence microscopy (40x magnification). Observed cells were used in a study performed in reference [159].

3.D DISCUSSION

The broad structural substrate diversity of the OCTs make them highly susceptible sites for potentially harmful drug-drug interactions. Therefore, an increased understanding of the biochemical nature of the interactions between transporter and substrates could provide a prevailing advantage in improving the prediction of drug interactions involving these membrane transporters. Recently, increased efforts have been devoted towards better understanding the biochemical interactions between transporter and substrate among organic cation transporters [124,125,146,148,153]. Several studies utilized hypothesized 3-D structures of their target transporter (*e.g.* rat Oct1, rabbit Oct1 and Oct2, and hOCT2) in order to confirm experimentally predicted critical residues [143,146,148,153] (Table 1.5 in Chapter 1). These early studies generated homology models of OCTs based on the solved crystal structures of prokaryotic MFS transporters (from *E. coli*). Although the studies provided information on the structural details for OCTs that were previously unknown, the templates they used to generate models (*i.e.* LacY, GlpT) were limited in the fact that they share a low sequence identity with mammalian (human) OCTs (~15%) perhaps due to their prokaryotic origin.

Therefore, in the current study, homology models of the tertiary structure of hOCT2 were generated using the known crystal structure of PiPT serving as the template. PiPT, also a member of the MFS, was chosen as the designated template due to a number of factors including its relative sequence homology to the hOCTs (~21% identical, 40% similar), eukaryotic origin (*Piriformospora indica*), and the fact that it was crystallized in the occluded state. The occluded conformation grants the transporter maximum binding interaction sites for bound ligands. After docking MPP^+ into the generated hOCT2 models,

amino acid residues were identified that formed the putative binding pocket (within a 5 Å radius surrounding the substrate) (Figure 3.5). This approach required that several assumptions be made during the *in silico* model building process including that adequate structural similarity exists between the crystallized tertiary structure of PiPT and hOCT2 and that the presence of water molecules in the occluded binding pocket was negligible and therefore not considered during the docking analysis. All models were generated based on PiPT and the hOCT2 protein sequence with transmembrane domains globally energy minimized.

Amino acid residues deemed "critical" for hOCT2-MPP^+ binding interactions were identified *in silico* based on substrate proximity and interaction types (Table 1.5). Within the proposed binding pocket, hydrophobic interactions were identified between MPP^+ and amino acid residues Gln242, Thr246, and Glu448, and one of the aromatic rings of MPP^+ was found to be involved in edge-face pi and pi-stacking interactions with Tyr245 and Tyr362, respectively. Subsequently, stably transfected CHO cells expressing hOCT2 mutants were established and utilized for a series of *in vitro* kinetic assays to confirm their role in substrate binding. From the functional screening study, transport activity of MPP^+ was absent for both conservative and non-conservative substitutions of Tyr362, and for the non-conservative substitution of Gln242 (Figure 3.11). Because MPP^+ transport was lacking for both conservative and non-conservative substitutions at Tyr362, this suggested that it may be a critical site for substrate binding. This result correlates with the MPP^+ docking data where Tyr362 was predicted to participate in the strongest substrate interaction (pi-pi stacking). However, the loss of transport activity with the conservative phenylalanine substitution, where the only structural difference is a loss of an aromatic

hydroxyl group, suggests that the hydroxyl group in Tyr362 may mediate additional important interactions with other residues within the binding pocket beyond pi-pi stacking with the substrate, thus playing a significant role in forming the structure of the binding pocket. When the hydroxyl is absent, as in the Tyr362Phe mutant, the residue may exist in a different spatial conformation that makes it less accessible for substrate-pi-stacking interactions. For hOCT2 mutants retaining MPP^+ transport function, only Tyr245Ala demonstrated a significant decrease in affinity for the substrate compared to wildtype (Table 3.7). As such, Tyr245 also may be deemed an important site for hOCT2-MPP^+ interaction. To briefly summarize, these initial findings suggest that Gln242, Tyr245, and particularly Tyr362 may be important for hOCT2-MPP^+ interactions within the proposed binding pocket. Tyr362 demonstrates the strongest case for importance considering both its conservative and non-conservative substituted mutants eliminated transporter activity for MPP^+.

There are several explanations for the hOCT2 mutants (Gln242Lys, Tyr362Phe, and Tyr362Ala) that exhibited complete loss of MPP^+ transport activity. The specific amino acid may be a critical residue for transporter-MPP^+ substrate interactions and thus when substituted leads to a complete absence of MPP^+ accumulation. Alternatively, the proposed transporter-binding pocket conformation could be altered as a result of the mutated residue. Another possibility is that transfection was not successful and therefore cDNA integration into the genomic DNA would be absent. Finally, the amino acid could be critical for maintaining the tertiary and quaternary structure of the transporter and when mutated could lead to a misfolded protein that is subsequently degraded rather than trafficking to the cell membrane following translation.

Genomic integration of intact cDNA for hOCT2 mutants was confirmed by PCR and gel electrophoresis (Figure 3.13) which ruled out a failed transfection. In order to confirm that inactive mutant hOCT2 transporters were translated and inserted into the plasma membranes of transfected mammalian cell lines Western blotting was performed. Transporter protein detected in the cell membrane fraction of nonfunctional mutants would suggest that the wildtype amino acid is likely a critical residue for interactions with MPP^+. However, in this study, the polyclonal hOCT2 antibody failed to discriminate between CHO mock and hOCT2 transfected cells (Figure 3.14). Additionally, the antibody did not appear to bind specifically to hOCT2, as signal was detected at the expected position in membranes prepared from CHO mock, as well as from wildtype hOCT1 or hOCT3 expressing cells (data not shown). The consistent detection of a clear, single band for actin ruled out any issues related to assay technique. When hOCT2 was probed in subsequent immunocytochemistry experiments using the same polyclonal hOCT2 antibody, no consistent fluorescent signal localized in the plasma membrane of CHO cells expressing hOCT2 was observed indicating the issue was related to the commercial hOCT2 antibody's lack of specificity. Thus, no conclusions could be drawn from these experiments.

Previous studies successfully demonstrated plasma membrane targeting when the transporter sequence for rOct1 or rOct2 was fused in frame to the C-terminus of GFP and transfected into MDCK cells [159,160]. A similar approach was performed in the current study by fusing the coding sequence of hOCT2 to the C-terminus of GFP to evaluate membrane targeting of non-functional hOCT2 mutants. However, we failed to observe targeting at the plasma membrane in CHO cells transiently transfected with the wildtype

hOCT2-GFP fusion construct. Instead we observed a consistent pattern of fluorescence in the cytosol surrounding the nucleus. The discrepancy in what was observed compared to the prior studies may be due to differences associated with the cell line used (MDCK vs CHO cells). A future study involving the transfection of our pEGFP-hOCT2 fusion construct into MDCK cells should be considered.

In the analysis of docking known substrates with varying structures into the hOCT2 homology models, interacting amino acids were identified to be unique for some substrates and shared for others (Table 3.3). For example, Glu448 was amongst the residues identified that was shared across many substrates including MPP^+, cimetidine, epinephrine, metformin, and serotonin. This residue corresponds to Glu477 in rabbit Oct2, which was identified as being critical for mediating TEA transport and verified by a rabbit Oct2 homology model based on GlpT [153]. Glu447/Glu448, an amino acid with an acidic side chain, may be a critical site for anchoring positively charged substrates under physiological conditions. Cys474, which was identified in a prior study as a critical site for forming a pathway for hOCT2 mediated TEA transport and confirmed through homology models based on the crystallized structure of LacY [146], was also identified in the present study for interacting with TPA. This finding was not too surprising considering the shared quaternary nitrogen-based structural scaffold of TEA and TPA. From these observations, our model suggests that there may be one binding pocket along the central cavity of hOCT2. Within this binding pocket, there may be a core set of amino acids that interact with most substrates, in conjunction with additional substrate-specific amino acids that accommodate structurally diverse (typically larger) substrates. Additional *in vitro* work

involving transporter mutagenesis experiments and subsequent kinetic analysis for each substrate would be necessary to support the preliminary *in silico* findings.

Based on the *in silico* hOCT2 modeling and subsequent *in vitro* kinetic studies, the amino acids most critical for MPP^+ interactions reside in TMDs 5, 7 and 10. Prior studies based on secondary and tertiary structures identified critical interacting residues in TMDs 4, 10, and 11 [124,125,143,146,148,153]. There are a number of factors that could explain this apparent discrepancy. The majority of the prior substrate interaction studies were done with rodent OCTs; thus, species differences could account for the variations of identified residues. Additionally, different substrates were examined; TEA and choline were used in the rat and rabbit studies whereas the focus of the current work was on interactions with MPP^+. As revealed in the analysis of docking diverse substrates in the current study, critical interacting amino acids may be unique to each substrate. This is not a surprising result given the diverse array of structures represented by OCT2 substrates. Finally, for the homology studies that have been performed previously, the templates utilized (LacY and GlpT) were both crystallized in the inward open conformation. Considering that PiPT was crystallized in the occluded state, different amino acids may be exposed to the substrates during *in silico* docking across the two conformation states. It may most likely be a combination of the latter two aspects in that structurally diverse substrates interact with unique sets of amino acids in a “transport channel” and these also vary as the transporter transitions through outward open, occluded, and inward open stages during substrate translocation.

In summary, a homology model for hOCT2 based on an existing crystallized structure of PiPT was successfully generated. Amino acid residues that may be critical

for hOCT2 transporter-substrate interactions along with a proposed binding pocket region were identified based on the selected MPP^+ docked model and were probed *in vitro* through mutagenesis studies. Additionally, a study involving the docking of known substrates into hOCT2 models identified overlapping and additional residues that may mediate transporter binding interactions. The results obtained in our combined *in silico* and *in vitro* study suggests a single binding region present along a central cavity within hOCT2 that shares some similarity with models generated in earlier published work. Future work, particularly confirming successful membrane targeting of non-functional hOCT2 mutants, will be necessary to strengthen our conclusions. Despite this shortcoming, the data acquired in the present study provides a sound foundation for understanding the physiochemical nature of hOCT2-substrate interactions that may ultimately serve to help optimize future rational drug design.

CHAPTER 4

IDENTIFYING STRUCTURAL ELEMENTS OF HUMAN ORGANIC CATION TRANSPORTER 1 (SLC22A1) MEDIATING SUBSTRATE-TRANSPORTER INTERACTIONS

4.A INTRODUCTION

The organic cation transporters (OCTs), OCT1, OCT2, and OCT3, are members of the solute carrier 22 (SLC22) subfamily of the major facilitator superfamily and via facilitated diffusion are responsible for the cellular entry of a variety of structurally diverse small organic molecules typically with positive charge. The OCT paralogs share similarities in their sequence, transmembrane topology, preferred substrates, and mechanism of substrate translocation. Despite these similarities, their sites of expression in the major organ systems vary. In humans, OCT1 and OCT3 both mediate substrate entry into enterocytes (OCT1 and OCT are expressed along the basolateral membrane and brush border, respectively) [1]. OCT1 and OCT3 are expressed along the sinusoidal membrane of hepatocytes in the liver playing a role in the first steps of hepatic elimination for their substrates [6]. In kidney, OCT2 and OCT3 are expressed on the basolateral membrane of proximal convoluted tubules governing the initial process of renal elimination [1]. OCTs have been shown to interact with hundreds of different endogenous and exogenous substrates/inhibitors under physiological conditions which include metabolites (*e.g*. creatine), neurotransmitters (*e.g.* serotonin, dopamine), hormones (*e.g*.

corticosterone), receptor antagonists (*e.g.* cimetidine), and antidiabetics (*e.g.* metformin) [1]. Due to their polyspecific nature and their tissue expression profiles, OCTs play a pivotal role in the absorption and elimination of their substrates impacting their pharmacokinetics and efficacy. As such, there is an increased potential for drug-drug interactions in patients taking concomitant medications.

OCT2, is an important mediator of renal elimination and also a major site for clinically important drug-drug interactions. In turn, OCT2 has been routinely studied during the drug development process and is even included in regulatory guidances (*e.g.* FDA and EMA) as a protein target for the evaluation of new drug entities as substrates/inhibitors [112,113]. OCT1, on the other hand, despite being expressed in the sinusoidal membrane of hepatocytes and potentiating the initial steps of hepatic elimination for hundreds of compounds, has only recently emerged as a “clinically important” transporter. Evidence has been reported highlighting the significance of OCT1 in drug-drug interactions and pharmacogenetic variability [116,161,162]. For example, fenoterol, a widely used narrow therapeutic window anti-asthmatic drug, was shown to have its pharmacokinetics and pharmacodynamics affected by genetic variants of OCT1 [161]. Compared to healthy individuals, OCT1-deficient patients demonstrated a 1.9-fold increase in systemic fenoterol exposure and 1.7-fold decrease in volume of distribution. As a result, heart rate and blood glucose both significantly increased by 1.5-fold, and 3.4-fold, respectively [161]. OCT1 also was shown to mediate hepatic uptake of sumatriptan, a drug used to treat acute migraines [116]. Systemic exposure of sumatriptan was increased by 2.1-fold in OCT1-deficient patients which was comparable to individuals with liver impairment. OCT1 polymorphisms, showed similar pharmacokinetic effects for the

active metabolite of the opiate analgesic tramadol, tropisetron, where systemic exposure was increased by 2-fold in homozygous OCT1 variant carriers [162]. These studies strongly suggest hepatic OCT1 to be a clinically important mediator of pharmacogenetic, pharmacokinetic and pharmacodynamic variability, and potentially drug-drug interactions. For the aforementioned studies, OCT1 serves as the rate limiting step for the transfer of many drugs from the systemic circulation to the liver. As OCT1 governs the hepatic clearance of these compounds, it essentially serves to mediate systemic drug exposure, thus establishes itself from a mechanistic DDI perspective as a potential major determinant of pharmacokinetics and drug clearance [163]. In light of the evidence, members of the International Transporter Consortium have even raised strong suggestions that evaluations of OCT1 be included as part of a rational drug design strategy [163].

Having the 3-D structural information available for hOCT1 is paramount for obtaining a better understanding of transporter-substrate interactions from a physicochemical perspective. However, to date, a crystal structure for any SLC22 family member has yet to be solved. An alternative strategy involves the construction of a homology model using the known crystal structure of a closely related protein (in this case transporter). Earlier studies have used the prokaryotic lactose permease (LacY) and glycerol-3-phosphate (GlpT) transporters as templates for studying the structures of OCT1 and OCT2 in rat, rabbit, and human [124,127,143,145,146,148] (Table 1.5). Despite these efforts identifying a number of amino acid residues that may be critical for OCT-substrate interaction, their models were generated based on templates that were prokaryotic in origin, crystallized in an inward facing conformation, and shared low OCT

sequence similarity (~15%). Additionally, the homology models were generated in order to confirm the spatial orientation of important residues identified *in vitro*, rather than used as a preliminary step for guiding amino acid mutational experimentation.

In the current study, the elucidation of critical amino acid residues for transporter-substrate binding interactions of hOCT1 was conducted by the generation of homology models using the *Piriformospora indica* phosphate transporter (PiPT), a structurally related eukaryotic transporter, as template. The information acquired from the newly constructed model was utilized in order to make predictions and assist in facilitating site directed mutagenesis studies to assess the homology model's validity and to observe any potential changes in transport function and/or affinity (K_m) for its prototypical substrate, MPP^+. Docking studies for hOCT1 were performed for additional known substrates with varying structure in order to more broadly investigate transporter-substrate interaction. Further defining how OCT1 biochemically interacts with its broad array of substrates will provide significant insight to the understanding and prediction of drug-drug interactions in polypharmacy patients and the advancement of future rational drug design for therapeutics targeting OCT1.

4.B MATERIAL AND METHODS

4.B.1 Chemicals and reagents

Tritiated [^{3}H] MPP^+ was purchased from PerkinElmer Life and Analytical Science (Waltham, MA) and unlabeled MPP^+ was obtained from Sigma-Aldrich (St. Louis, MO). Quinine monohydrochloride dihydrate was purchased from Acros Organics (Fair Lawn, NJ). Bio-Rad protein assay dye reagent concentrate was purchased from Bio-Rad Laboratories, Inc. (Hercules, CA). Specific primers for mutation reactions were purchased from Integrated DNA Technologies (IDT; Coralville, IA). QuikChange Lightning Site-Directed Mutagenesis Kit was purchased from Agilent Technologies (Santa Clara, CA). Lipofectamine® 2000 Transfection Reagent and Prolong diamond antifade mountant with DAPI was purchased from ThermoFisher Scientific (Waltham, MA). QIAprep spin miniprep kit and QIAprep spin midiprep kit [154] were purchased from QIAGEN Inc. (Germantown, MD). GoTaq green master mix was purchased from Promega (Madison, WI). Opti-Mem reduced serum and Dulbecco's modified eagle's medium were purchased from Life Technologies (Carlsbad, CA).

4.B.2 Homology modeling and docking studies

The hOCT1 (UniProt ID: O15245) and PiPT (PDB ID: 4J05) sequences were obtained from the Universal Protein Resource (UniProt) and PDB, respectively [131,155]. Protein sequence alignment of PiPT and hOCT1 was performed with ClustalX and followed by sequence curating via loop removal and manual refinement of gaps based on the transmembrane domains observed in the PiPT crystal structure and predicted for hOCT1 using ICM Browser (Molsoft LLC) and Phobius (Stockholm Bioinformatics Center). Amino acid sequence alignment of hOCT1 with the template and subsequent

generation of a population of 100 homology models were performed using ClustalX 2.1 and MODELLER v9.17, respectively. Using SYBL-X 2.1, a structural cavity search was conducted for each model to identify putative binding pocket(s). The hOCT2 substrates, MPP^+, epinephrine, serotonin, cimetidine, tetrapentylammonium (TPA) and metformin, and the hOCT2 inhibitor, quinine, (Figure 4.1) were sketched and energy-minimized using SYBL-X 2.1 (Tripos Force Field, Gasteiger-Hückle charges distance-dependent dielectric constant = 4.0 D/Å) and docked into each of the 100 models within a 15 Å radius of Trp354 (a residue present within the identified binding pocket) using GOLD Suite 5.5. A favorable model was selected based on the combined MODELLER discrete optimized protein energy (DOPE) score, GOLD docking score, and Ramachandran plot results. The DOPE score, accounting for spherical and finite shape of the native structures, helps to determine the quality of the protein models. The GOLD score evaluates the interactions of the docked substrate within the proposed binding pocket(s). Ramachandran plots were used to help visualize energetically allowed regions for backbone dihedral angles against amino acid residues in the protein structure. A model with more than 90% of amino acids located in the favorable regions of a Ramachandran plot is generally considered an acceptable model. High resolution images were obtained using PyMOL v1.8.and SYBL-X-2.1.

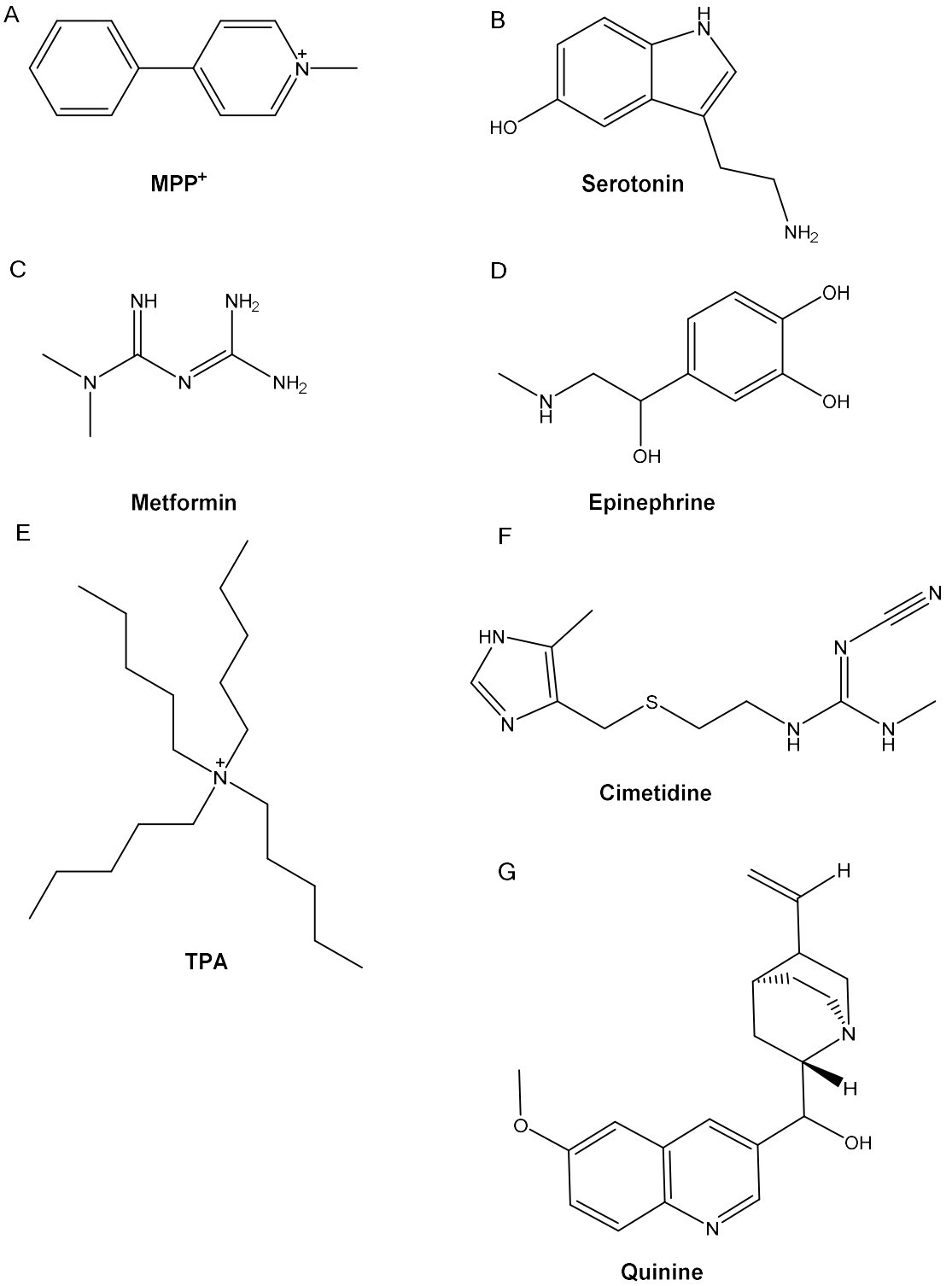


Figure 4.1 Chemical structures of compounds docked into hOCT1 homology models.

4.B.3 Bacterial transformation

Plasmid DNA (pcDNA3-hOCT1) was transformed through the following steps: adding 10 ng of DNA to 50 µL of DH5alpha competent cells, incubating on ice for 30 minutes, and then applying heat shock at 42°C for 20 seconds. The mixture was then added to 950 µL of 37°C preheated LB broth and incubated while shaking (225 rpm) at 37°C for one hour. Afterward, the mixture was plated onto LB agar plates containing ampicillin (0.1 mg/mL) and incubated overnight at 37°C. The following day, colonies were picked and grown overnight (with shaking at 225 rpm) in LB broth with ampicillin (0.1mg/mL) at 37°C. Plasmid DNA extraction was performed using the Qiaprep spin miniprep kit according to the manufacturer's recommendations [154]. Bacterial pellets were resuspended and lysed, followed by the use of spin columns to isolate plasmid DNA and wash/discard any impurities in the flow through. Eluted plasmid DNA from the column was stored at -20°C. Plasmid DNA concentration and purity were determined via UV spectrophotometry.

4.B.4 Point mutation of plasmid DNA

Synthetic oligonucleotide primers containing the desired DNA mutations were designed using the QuikChange Primer Design program (Agilent Technologies) (Table 4.1). Amino acid substitutions were introduced into the hOCT1 coding sequence via site directed mutagenesis (QuikChange Lightning Site-directed Mutagenesis Kit) according to the manufacturer's recommendations. The resulting mutant plasmids were transformed into XL 10-GOLD ultra-competent cells according to the manufacturer's protocol and plated on LB-agar plates with ampicillin (0.1 mg/mL) and incubated overnight at 37°C.

Colonies were picked, purified, and the presence of the desired mutation was then confirmed by DNA sequencing.

Table 4.1 Primers for hOCT1 site directed mutagenesis.

Protein residue	Direction	Mutant oligonucleotide (5' → 3')
Gln241Glu	Forward	CCG TGA AGG CCA TCT CGT ACA TGA TCG CCA C
	Reverse	GTG GCG ATC ATG TAC GAG ATG GCC TTC ACG G
Gln241Lys	Forward	CCG TGA AGG CCA TCT TGT ACA TGA TCG CCA C
	Reverse	GTG GCG ATC ATG TAC AAG ATG GCC TTC ACG G
Phe244Tyr	Forward	CAG CCC CAC CGT GTA GGC CAT CTG GTA
	Reverse	TAC CAG ATG GCC TAC ACG GTG GGG CTG
Phe244Ser	Forward	CAG CCC CAC CGT GGA GGC CAT CTG GTA
	Reverse	TAC CAG ATG GCC TCC ACG GTG GGG CTG
Thr245Ser	Forward	CCA GCC CCA CCG AGA AGG CCA TCT G
	Reverse	CAG ATG GCC TTC TCG GTG GGG CTG G
Thr245Lys	Forward	CAG CCC CAC CTT GAA GGC CAT CTG GTA CAT
	Reverse	ATG TAC CAG ATG GCC TTC AAG GTG GGG CTG
Tyr361Phe	Forward	GAG CCC CTG AAA GAG CAC AGA GTC CGT GA
	Reverse	TCA CGG ACT CTG TGC TCT TTC AGG GGC TC

Tyr361Ala	Forward	CAC GGA CTC TGT GCT CGC TCA GGG GCT CAT CCT G
	Reverse	CAG GAT GAG CCC CTG AGC GAG CAC AGA GTC CGT G
Gln447Glu	Forward	CAC CAG GCA GAT CAT TTC TAT TGC AAT GGT GAT TCC
	Reverse	GGA ATC ACC ATT GCA ATA GAA ATG ATC TGC CTG GTG
Gln447Lys	Forward	TCA CCA GGC AGA TCA TTT TTA TTG CAA TGG TGA TTC CC
	Reverse	GGG AAT CAC CAT TGC AAT AAA AAT GAT CTG CCT GGT GA

4.B.5 Cell line transfection and maintenance

Mutant transporter expressing CHO cell lines were generated using cationic lipid-based transfection. Briefly, 1µg plasmid DNA was combined with 2 µL Lipofectamine 2000 (Invitrogen), mixed, diluted in 100 µL Opti-MEM (Invitrogen) and applied to CHO cells at 50-60% confluency in 12-well plates (Corning Inc, Corning, NY). Fresh culture medium (DMEM/F12) was applied just prior to the addition of transfection agents. After incubating for 24 hours at 37°C / 5% CO_2, the transfection medium was removed and replaced with fresh medium containing geneticin (G418; 1 mg/mL) to select for successfully transfected cells for a period of 14-21 days.

CHO control, CHO-hOCT1 and CHO-hOCT1 mutant cell lines were maintained in Dulbecco's Modified Eagle's Medium/F12 (DMEM/F12) with 10% FBS, and 1% Penicillin/Streptomycin at 37°C with 5% CO2 in 25 or 75mm^2 polystyrene flasks. G418 (250µg/mL) was included in the medium for maintaining selective pressure on stably-transfected cell lines. Cells were sub-cultured every 3-4 days and passages 10-40 were used for experiments.

4.B.6 Cell accumulation assays

Mutant functional screening

The procedure for the cell accumulation assay has been described previously [68,69]. Briefly, cells were seeded into 24-well tissue culture plates at a density of 1.5×10^5 cells/well in the absence of antibiotics and cultured for 48 hours. Cells were equilibrated with transport buffer for 10 min (500 µL of Hanks' balanced salt solution containing 10 mM HEPEs, pH 7.4). Equilibration transport buffer was replaced with 400 µL of fresh transport buffer containing 1 µM unlabeled MPP^+ spiked with trace [^{3}H]MPP^+ (0.25 µCi/ml)

in the presence or absence of the inhibitor quinine (200 μM). After incubation for 10 minutes, the cells were immediately rinsed 3 times with ice cold transport buffer, lysed with 200 μL 1N NaOH, neutralized with 250 μL 1N HCl and 200 μL 10mM HEPES. The radioactivity in cell lysates was quantified by liquid scintillation counting, and uptake normalized by the total protein content determined by the Bradford method. The intracellular accumulation of substrates was reported as picomoles of substrate per milligram total protein. All uptake data were corrected for background accumulation in corresponding CHO empty vector cells.

Kinetic assays

The Michaelis-Menten constant (K_m) was determined for MPP^+ uptake in each of the generated mutant hOCT1-expressing cell lines via saturation analysis according to our established protocol [156]. The experiment was carried out in the same way as described for the functional screening assay with the exception that the equilibration transport buffer was replaced with 400 μL of fresh transporter buffer containing increasing concentrations (1-200 μM) of unlabeled MPP^+ spiked with [^{3}H]MPP^+ (0.25 μCi/ml) and incubated for a period of 1 minute. After incubation, the cells were immediately rinsed 3 times with ice cold transport buffer and lysed with 1N NaOH, neutralized with 250 μL 1N HCl and 200 μL 20mM HEPES. The K_m estimate, which represents the concentration of substrate at half maximum velocity of the transporter, was calculated using nonlinear regression with the enzyme kinetics model in GraphPad Prism 5.0 (GraphPad Software Inc., San Diego, CA). Individual saturation experiments were repeated at least three times with duplicate wells and plotted as mean ± SD. K_m estimates were reported as mean ± SE.

4.B.7 Genomic DNA integration confirmation

Cells were suspended in 500 µL lysis buffer [1 M Tris (pH 8.0), 5 M NaCl, 0.5 M EDTA, and 10% SDS] containing proteinase K (0.4 mg/mL) and incubated at 55°C while shaking overnight. Genomic DNA was thoroughly extracted from samples with an equal volume of phenol/chloroform/isoamyl alcohol (25:24:1) after gentle mixing for 10 min, and centrifugation for 10 min at 15,000 g. The upper aqueous phase was carefully collected, isopropanol was added and mixed well, then centrifuged immediately at 15,000 g for 30 min to obtain DNA pellet. The pellet was washed with 70% ethanol, dried, and resuspended with 50 µL TE buffer [10 mM Tris (pH 8.0), and 1 mM EDTA]. Concentration of DNA was determined through UV spectrophotometry. Genomic DNA (2 ng), 2x Go-taq Master Mix (5 µL), as well as 1 µL primer pair mix (T7: 5'- TAATACGACTCACTATAGGG-3; hOCT1-REV: 5'- TGAAGGCCATCTGGTACATG -3') were added together to a final volume of 20 µL and run in a thermocycler: initial denaturation at 95°C for 5 min, followed by 30 cycles of: denaturation at 95°C for 2 min, annealing at 50-52°C for 30 seconds, and elongation at 72°C for 30 seconds. Final elongation step at 72°C for 5 min and held at 4°C. PCR products were loaded into a 1% agarose gel for separation using electrophoresis at 120 V for 60 min and visualized by UV light following ethidium bromide staining.

4.B.8 Green fluorescent protein (GFP) plasmid construction

To make the hOCT1-GFP fusion construct, the full length hOCT1 cDNA fragment was removed from the isolated library clone, pcDNA3/hOCT1, using the restriction enzymes Kpn I and Xba I. The fragment was gel isolated and ligated into the pEGFP-C1 vector in frame at the carboxyl terminal end of GFP forming the plasmid pEGFP-

C1/hOCT1, where “E” denotes “enhanced”. Plasmid construction was performed commercially (GenScript, Picataway, NJ). The lyophilized GFP plasmid construct, was resuspended and diluted in TE pH 8, transformed into DH5-alpha cells and DNA extracted using the Qiagen miniprep kit. The construct was confirmed by DNA sequencing. Non-functional hOCT1 mutants were reproduced in the hOCT1-GFP construct using the original primers (Table 4.1) and the QuikChange Lightning site-directed mutagenesis kit.

4.B.9 Microscopic imaging

An Olympus IX-70 inverted microscope fit with a 12-bit camera was used to capture phase contrast and fluorescent images (Olympus, Melville, NY). Fluorescent images were taken with two second exposures using a 595 nm dichroic long pass filter (Chroma, Rockingham, VT) illuminated by a mercury arc lamp. The images were processed using Olympus Microsuite v.5. Confocal fluorescent images were obtained at the VCU Microscope Core facility using a Zeiss LSM 710 Axio Observer inverted laser scanning confocal microscope fitted with a 63x oil immersion objective. Images were collected by illuminating samples with a blue diode laser at 405 nm. Images were processed using Zeiss ZEN 2 Blue edition software (Oberkochen, Germany).

4.B.10 Statistics

The data plots were presented as means ± SD. Dose response curve (K_m estimate) data were reported as mean ± SE for at least n = 3. K_m estimates were fit based on the equation: $V_0 = V_{max} * [S] / (K_m + [S])$. One-way ANOVA with post-hoc Dunnett’s test was used to evaluate differences compared to a single control where indicated. Statistical calculations were performed using Prism 5.0 (GraphPad Software, Inc., San Diego, CA). A difference was deemed statistically significant if $p < 0.05$.

4.C RESULTS

4.C.1 Identification of a hOCT1 model

The hOCT1 peptide sequence (Uniprot ID: O15245) was aligned with the PiPT template sequence (PDB ID: 4J05) (Figure 4.2) as input for the program MODELLER to generate 100 initial hOCT1 homology models. Analysis of the initial 100 models identified a single large cavity in the central region of the transporter as a potential binding pocket. MPP^+ was subsequently docked in this region. After docking MPP^+ into the generated hOCT1 models, the most favorable interaction model was selected based on three main criteria: GOLD docking score, DOPE score, and the total number of clusters.

The genetic optimized ligand docking (GOLD) scoring is essentially a method to quantify which poses generated for a particular ligand are most likely to occur based on the interactions present within the transporter. GOLD scores for the top ten most favorable docked poses of MPP^+ in the binding pocket of the hOCT1 models (ranging from 58.52 to 64.5) were ranked (Table 4.2). Amongst this select group, the top four model's GOLD scores had a difference of 1.85 between them, thus were considered to be virtually identical. The difference between the top and fifth ranked model was increasingly larger (2.72). The discrete optimized protein energy (DOPE) score accounts for the shape of native structures which in turn helps to evaluate the quality of the whole protein structure. The DOPE scores for the top ten models ranged between -48,992 and -47,382 (Table 4.2). Additionally, the number of homology models which contained a given substrate pose (number of clusters) was also accounted for in model selection. The greater the number of models that have a particular substrate pose docked, the higher the likelihood that the specific pose occurs within the binding pocket. Out of the top 10

models, models 35 and 47 had the highest number of clusters (12 and 8 clusters, respectively), while the rest had 5 or less. Among the top four ranked GOLD score models, model 35 stood out as having the lowest DOPE score (-48,141; fifth lowest DOPE score overall) in conjunction with the highest number of clusters (12). Taken together, these three selection criteria indicate model 35 as the most favorable docked model and thus it was selected for subsequent studies. The generated tertiary structure for model 35 with MPP^+ docked in the hypothesized binding pocket is shown in Figure 4.3. The docked hOCT1 model shows MPP^+ residing inside a large central cavity of the 12-membrane spanning alpha helical domains.

Ramachandran plots were utilized as a method for determining and visualizing "allowed regions" for the backbone dihedral angles that make up amino acids in the generated model. For the amino acids that made up our selected hOCT1 model, 90.0% were in the most favored regions, 7.3% were in the additionally allowed region, and only 2.7% were in the generously allowed and disallowed regions combined (Figure 4.4). The most favored regions category was considered high enough to support the selected hOCT1 model as acceptable.



Figure 4.2 Sequence alignment of PiPT and hOCT1.

The alignment was constructed with ClustalX, followed by manually refining gaps based on the transmembrane regions observed in the PiPT crystal structure and predicted for hOCT1 using Phobius, a topology prediction algorithm. Residues were truncated for the large extracellular and intracellular loop between transmembrane domain 1 and 2 (TMD 1 and 2) and between TMD 6 and 7 of PiPT and hOCT1, respectively. The transmembrane domains in the hOCT1 model and PiPT tertiary structure are shaded. "*" indicates exact sequence match, ":" indicates high sequence similarity, "." indicates low sequence similarity

Table 4.2 Summary of hOCT1 model evaluation scores.

GOLD Rank	Model ID	GOLD score	DOPE Score	No. of Clusters
1	93	64.5	-47779.43359	5
2	22	63.65	-47533.55859	1
3	35	63.07	-48141.65625	12
4	100	62.65	-48001.56641	3
5	91	61.78	-48538.58984	3
6	47	60.58	-48042.83594	8
7	85	60.31	-47898.90625	1
8	46	60.21	-48336.22656	2
9	80	58.99	-47382.37891	1
10	73	58.85	-48217.75	2

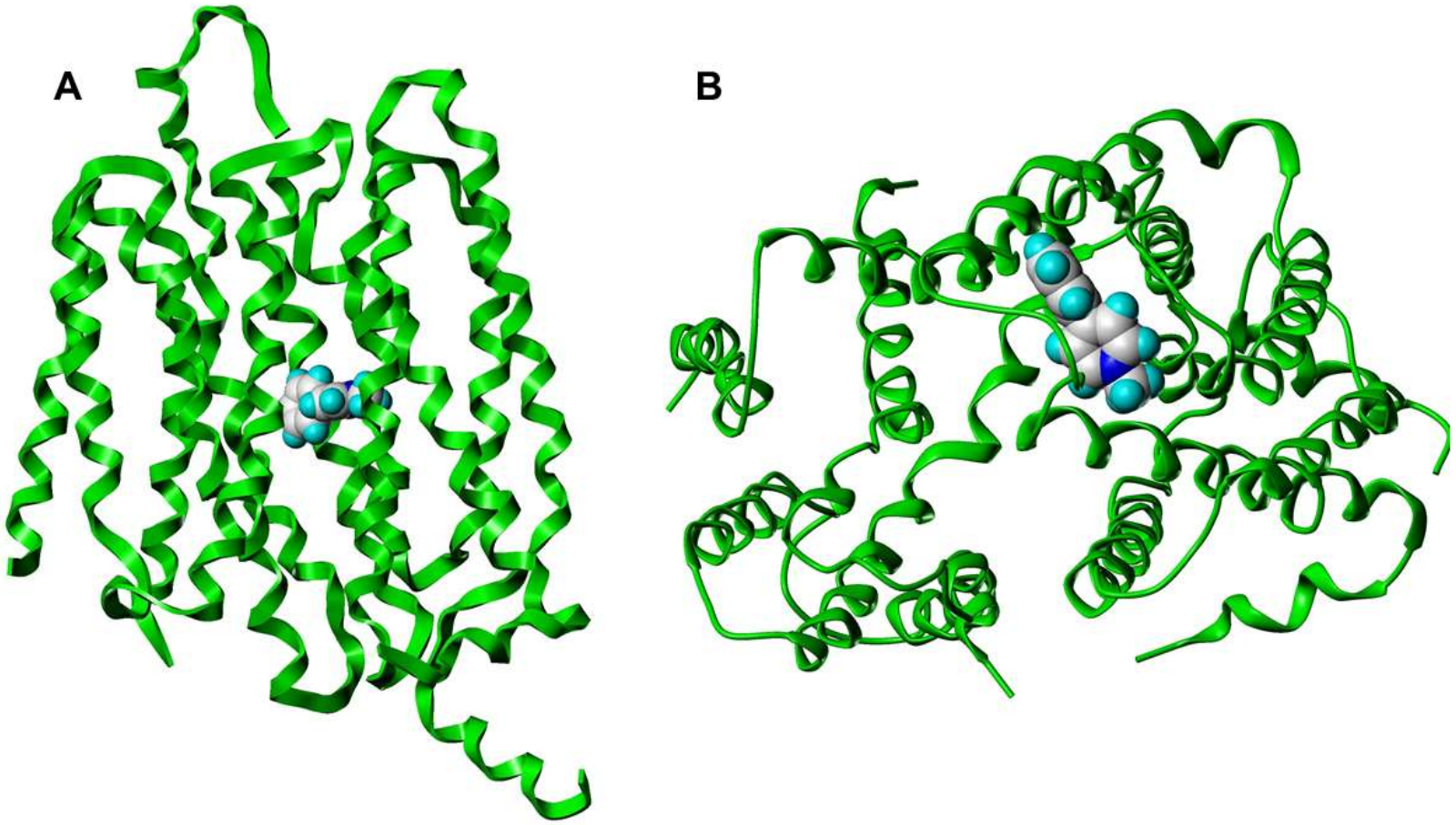


Figure 4.3 hOCT1 homology model.

The generated 3-D molecular structure of hOCT1 (ribbons) is shown with MPP^+ (space-filled) positioned in the putative binding pocket viewed from (A) profile and (B) top-down angles.

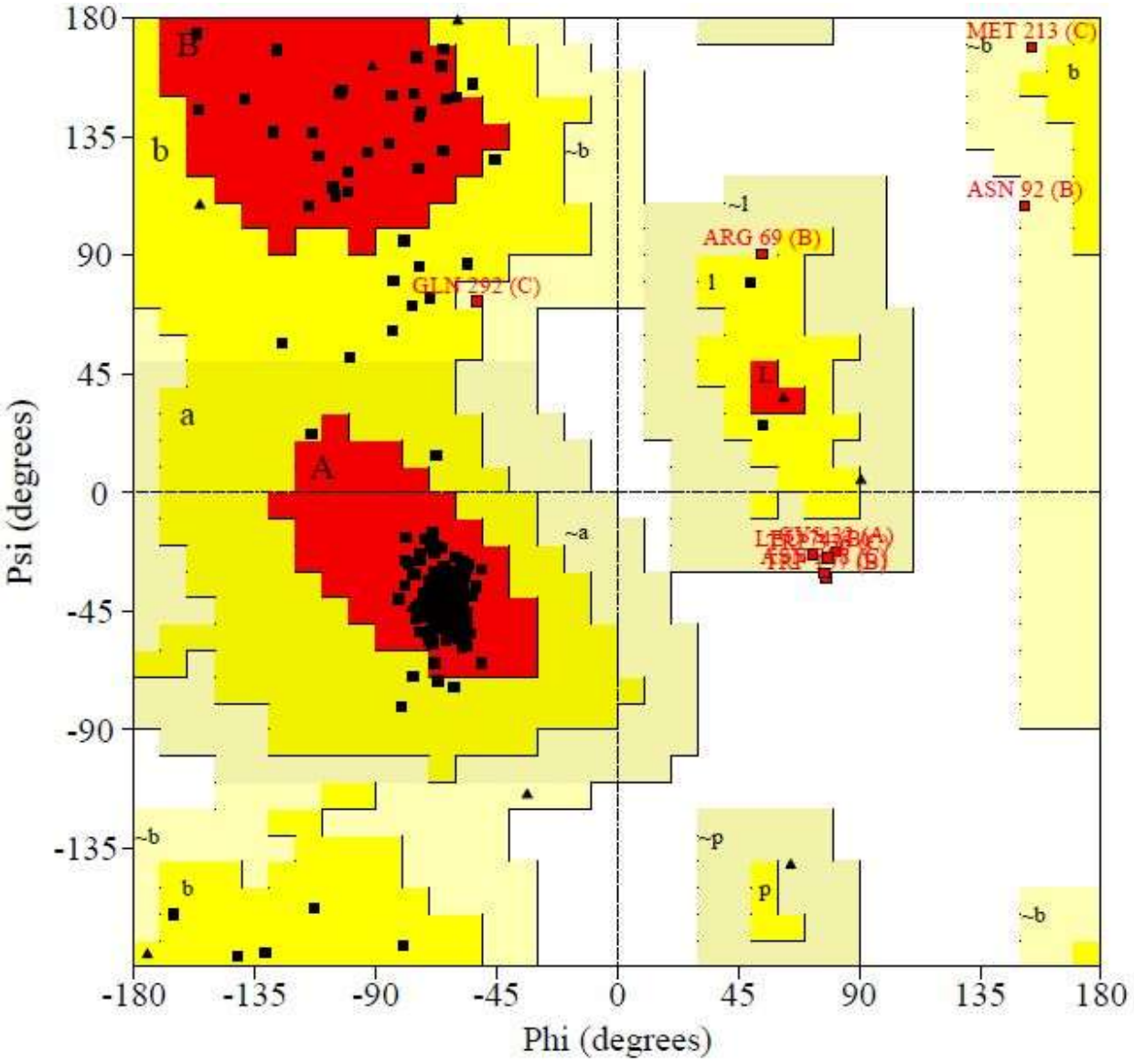


Figure 4.4 Ramachandran plot for hOCT1 homology model.

Phi and psi indicate backbone conformation dihedral angles of amino acid residues, representing the rotations of a polypeptide main chain N-Cα and Cα-C bonds. Amino acids are displayed in different regions: most favored region (red), additional allowed region (yellow), generously allowed region (light yellow), and disallowed region (white). Residues depicted in red squares are in the generously allowed and disallowed regions.

4.C.2 Identifying amino acid residues important for MPP^+ hOCT1 interaction

Several amino acids were identified that made up the binding pocket (within the designated 5 Å radius of the substrate) for docked MPP^+ in the selected hOCT1 model. The identified amino acid residues were found in several different TMDs that came together in the central area forming a large distinct cavity of the transporter—TMD 1: Trp16; TMD 5: Ile238, Gln241, Met242, Phe244, Thr245, Val246; TMD 7: Trp354, Asp357, Ser358, Tyr361, Gln362; TMD 8: Glu386, Ile387, Ala390; TMD 10: Ile444, Gln447, Ile449, Cys473 (Figure 4.5). Within the proposed binding pocket, five amino acids were identified (Gln241, Thr245, Phe244, Tyr361, and Gln447) as potential candidates critical for transporter-MPP^+ binding interactions. Hydrophobic interactions were found between MPP^+ and amino acid residues Gln241, Thr245, and Glu447, and one of the aromatic rings of MPP^+ was recognized as forming edge-face-pi and pi-stacking interactions with Phe244 and Tyr361, respectively (Figure 4.6 and Table 4.3).

To further evaluate the generated *in silico* hOCT1 model, known substrates with disparate structures were optimized and docked into the population of 100 models to determine the presence of alternative and/or additional critical amino acid residues in the binding pocket(s). The process involved with selecting the most favorable model for MPP^+, was repeated for each docked substrate. Amino acids identified with the greatest overlap across the different docked compounds were Phe244, Asp357, Tyr361, and Gln447 (Figure 4.7 and Table 4.3). There were several amino acids identified that were also unique to particular compounds including Thr245 for MPP^+; Trp16, Asn156, Phe159, and Asp474 for cimetidine; Gln20 for epinephrine; Leu23 for quinine; Ser358 for serotonin; and Ile449 for TPA.

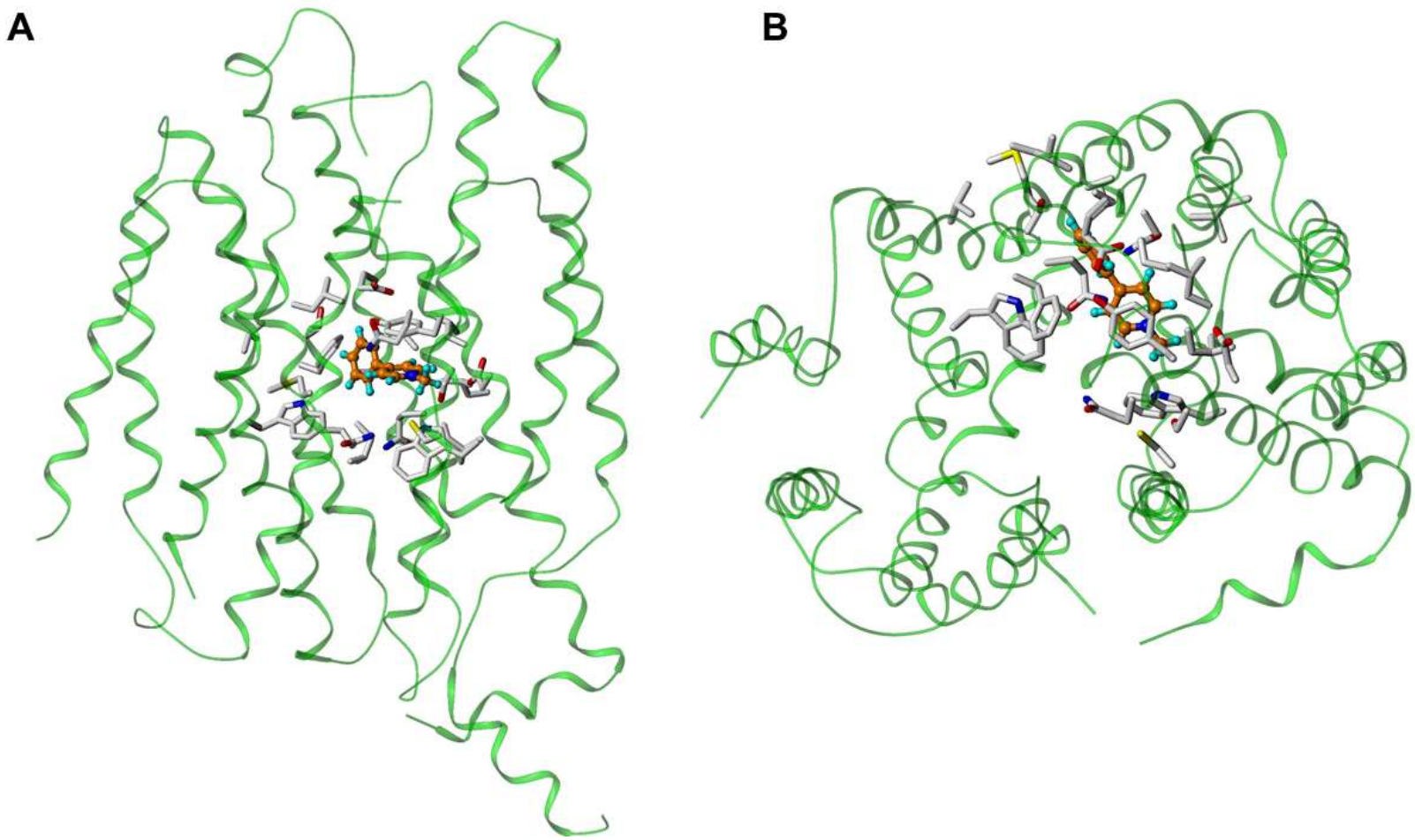


Figure 4.5 3-D rendering of putative binding pocket of hOCT1 with docked MPP^+.

Amino acid side chains (white) comprising the binding pocket surrounding the substrate MPP^+ (orange) is shown viewed from (A) profile and (B) top-down angles.

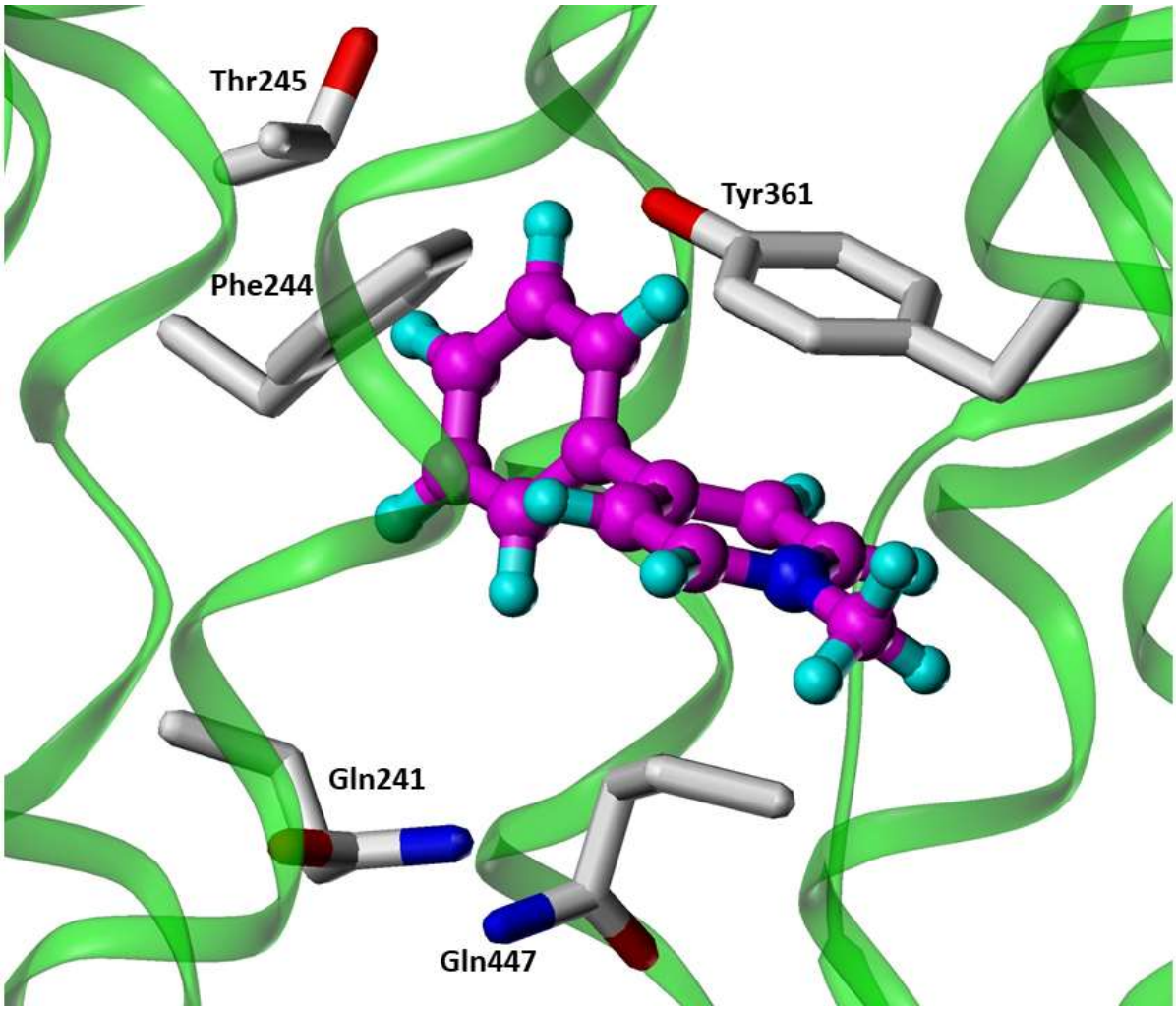


Figure 4.6 Structure of hOCT1 with MPP^+ docked.

The docked substrate (MPP^+, orange) and the amino acids (white side chains) is shown localized in the predicted substrate binding pocket of hOCT1.

Table 4.3 hOCT1 docking interaction summary.

Substrate	Amino Acid	Sequence position	Bond Interaction	TMD
MPP^+	Gln	241	Hydrophobic	5
	Phe	244	Edge Face pi	5
	Thr	245	Hydrophobic	5
	Tyr	361	Pi-stack	7
	Gln	447	Hydrophobic	10
Cimetidine	Trp	16	Hydrophobic	1
	Asn	156	H-bond	2
	Phe	159	Pi-stacking	2
	Trp	217	Hydrophobic	4
	Phe	244	Hydrophobic	5
	Asp	357	H-bond (salt bridge)	7
	Tyr	361	Pi-stacking	7
	Gln	362	H-bond	7
	Asp	474	H-bond (salt bridge)	11
Epinephrine	Gln	20	H-bond	1
	Phe	244	Edge-face pi	5
	Asp	357	H-bond	7
	Tyr	361	Pi-stacking	7
	Gln	447	Hydrophobic	10
	Cys	450	Hydrophobic	10
Metformin	Phe	244	Edge-face pi	5

	Trp	354	Hydrophobic	7
	Asp	357	H-bond (salt bridge)	7
	Tyr	361	Pi-stack	7
	Gln	447	Hydrophobic	10
	Cys	473	Hydrophobic	10
Quinine	Leu	23	Hydrophobic	1
	Trp	217	Hydrophobic (weak)	4
	Phe	244	Hydrophobic	5
	Asp	357	H-bond	7
	Tyr	361	Pi-stacking	7
	Gln	447	H-bond	10
	Cys	473	Hydrophobic	10
Serotonin	Gln	241	H-bond	5
	Phe	244	Hydrophobic	5
	Asp	357	H-bond	7
	Ser	358	Hydrophobic	7
	Tyr	361	Pi-stack	7
	Gln	362	H-bond	7
	Ile	444	Hydrophobic	10
	Cys	473	H-bond	10
TPA	Phe	244	Hydrophobic	5
	Asp	357	Ionic w/quaternary N	7
	Tyr	361	Hydrophobic	7

Ile	444	Hydrophobic	10
Gln	447	Hydrophobic	10
Ile	449	Hydrophobic	10
Cys	450	Hydrophobic	10

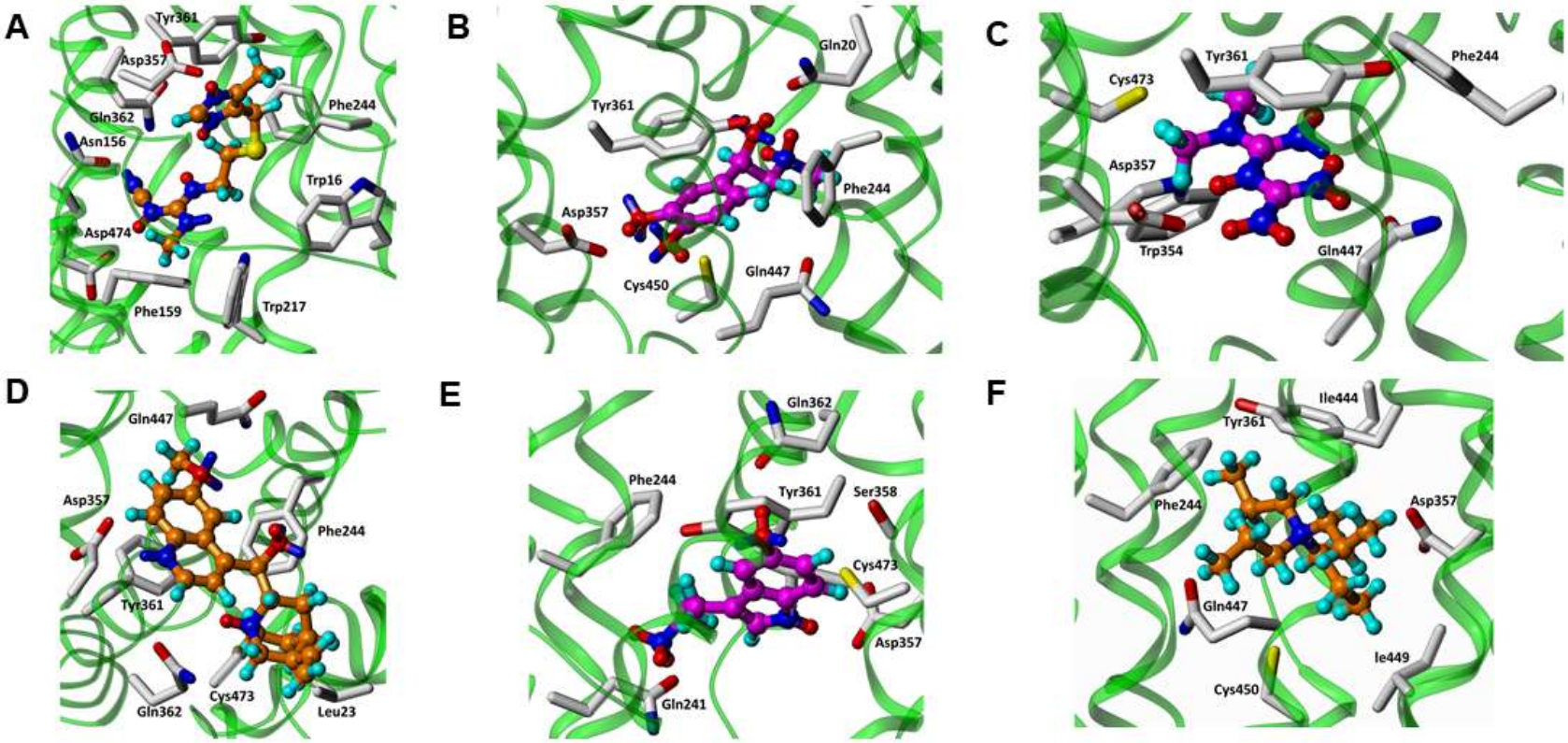


Figure 4.7 Known hOCT1 substrates docked into hOCT1 homology model.

Known hOCT1 substrates (purple or orange) (A) cimetidine, (B) epinephrine, (C) metformin, (D) quinine, (E) serotonin, and (F) TPA, were docked into their respective favorable hOCT1 models. Proposed interactions of interactions are summarized in Table 4.3.

4.C.3 Substitution of hOCT1 amino acid residues in putative binding pocket

We investigated the role of the predicted amino acids in hOCT1-MPP^+ interactions through conservative and non-conservative amino acid substitutions introduced into the hOCT1 coding sequence to evaluate potential changes in hOCT1 function and affinity for MPP^+. The pcDNA3/hOCT1 plasmid vector map is shown in Figure 4.8. The rationale for deciding each conservative and non-conservative amino acid substitution was based on a scheme developed by Bordo *et al.* which categorizes roughly equivalent amino acid residues based on their physicochemical properties of their side chains (Figure 4.9) [157]. Substitutions for residues deemed critical were Gln241Glu, Phe244Tyr, Thr245Ser, Tyr361Phe, and Gln447Glu (conservative); and Gln241Lys, Phe244Ser, Thr245Lys, Tyr361Ala, and Gln447Lys (non-conservative) (Tables 4.4, 4.5, and 4.6). Several attempts were made to generate the hOCT1 Tyr361Phe mutant. However, each time, the desired mutation was present as a tandem repeat, *i.e.*, the entire target region incorporated into the mutation generating primers was duplicated in the final product. We were unable to resolve how or why this occurred. All successfully constructed hOCT1 mutants were confirmed by DNA sequencing prior to generating stable cell lines. Figure 4.10, depicts a representative DNA-oligonucleotide duplex and sequencing chromatogram in which CAA, coding for Gln447 in wildtype hOCT1, was changed to GAA, coding for the hOCT1 mutant Gln447Glu.

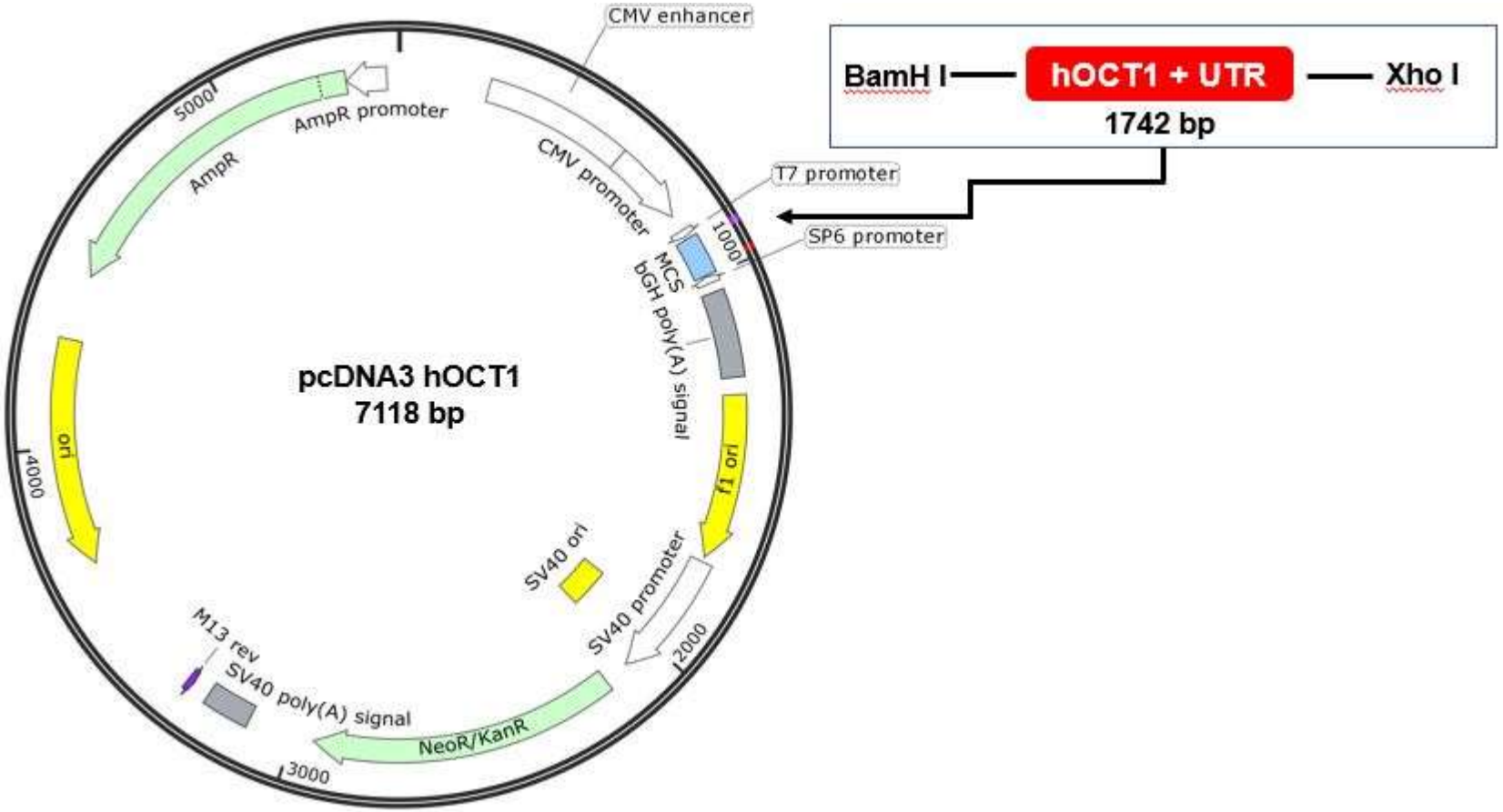


Figure 4.8 pcDNA3/hOCT1 vector map.

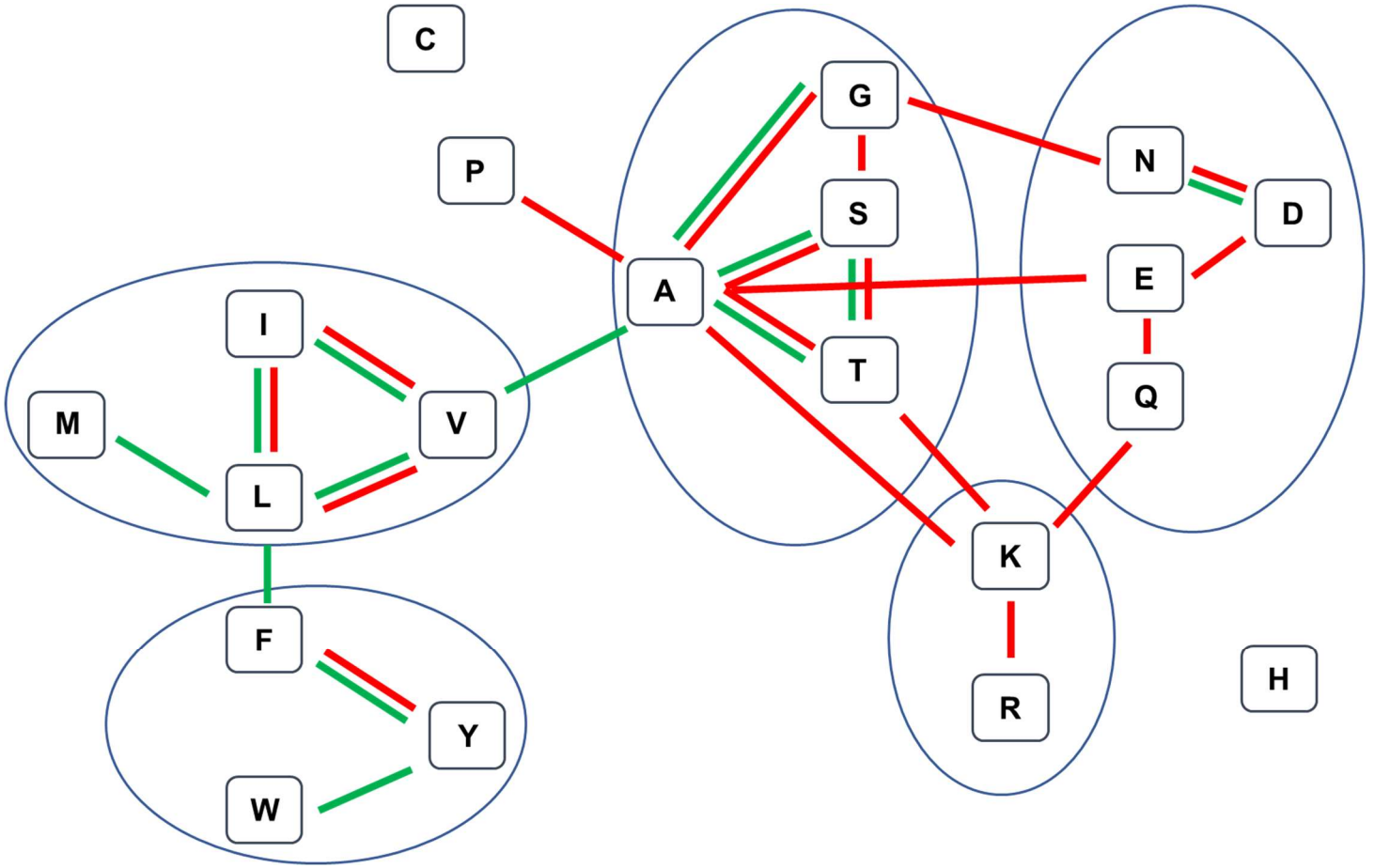


Figure 4.9 Suggested guidance for amino acid residue conservative substitution.

Roughly equivalent amino acid residues categorized based on physiochemical properties into five subgroups.

Diagram is an adapted figure from reference [157]

Table 4.4 Summary of hOCT1 residue substitutions.

	Substitution	
Residue	**Conservative**	**Non-Conservative**
Gln241	Glu	Lys
Phe244	Tyr	Ser
Thr245	Ser	Lys
Tyr361	Phe[a]	Ala
Gln447	Glu	Lys

[a] Mutant was not able to be generated

Table 4.5 hOCT1-MPP$^+$ interaction based conservative substitutions.

Amino Acid	Sequence position	Codon	Mutant Codon	Substitution
Gln	241	CAG	GAG	Gln → Glu
Phe	244	TTC	TAC	Phe →Tyr
Thr	245	ACG	TCG	Thr → Ser
Tyr	361	TAT	TTT	Tyr → Phe[a]
Gln	447	CAA	GAA	Gln → Glu

[a] mutant was not able to be generated

Table 4.6 hOCT1-MPP$^+$ interaction based non-conservative substitutions.

Amino Acid	Sequence position	Codon	Mutant Codon	Substitution
Gln	241	CAG	AAG	Gln → Lys
Phe	244	TTC	TCC	Phe →Ser
Thr	245	ACG	AAG	Thr →Lys
Tyr	361	TAT	GCT	Tyr → Ala
Gln	447	CAA	AAA	Gln → Lys

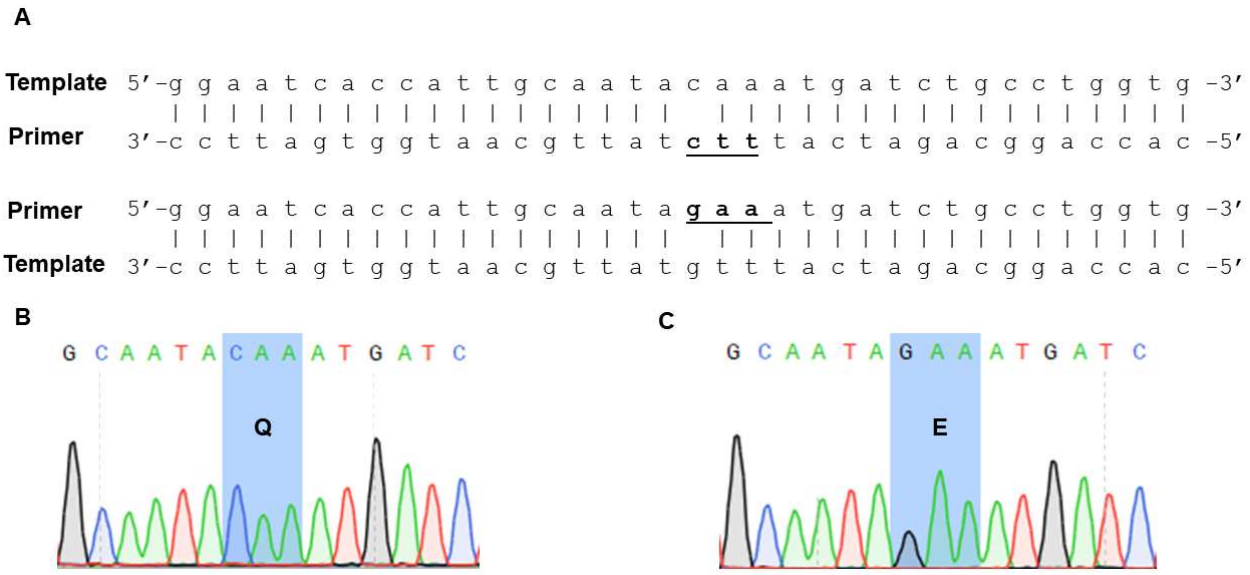


Figure 4.10 Representative sequencing chromatogram for hOCT1 mutants.

(A) DNA template-primer duplex for hOCT1 Q447E. Chromatogram for (B) hOCT1 wildtype and (C) hOCT1 Q447E are shown with triplet codon corresponding to mutation site highlighted

4.C.4 Critical amino acid confirmation through kinetic assays

In functional screening assays evaluating [^{3}H] MPP^+ transport (Figure 4.11), wild-type hOCT1 demonstrated a 5-fold higher uptake of MPP^+ compared to mock expressing (pcDNA3) background control cells (11.7 ± 4.9 pmol mg protein^{-1} 10 min^{-1} vs. 2.4 ± 0.02 pmol mg protein^{-1} 10 min^{-1}). Quinine (200 μM), a known inhibitor for OCTs, virtually abolished hOCT1 mediated MPP^+ transport. Four non-conservative mutants, hOCT1 Glu241Lys, Thr245Lys, Tyr361Ala, and Gln447Lys, resulted in a complete loss of MPP^+ transport activity (Figure 4.11). All other mutants retained some level of transport activity and were subjected to saturation analysis in order to estimate K_m (Figure 4.12, Table 4.7).

The affinity of MPP^+ determined for wildtype hOCT1 was comparable to values in prior studies (K_m = 16.3 ± 3) [158]. When comparing the K_m estimates for hOCT1 mutants against wildtype hOCT1, the non-conservative substitution Phe244Ser and the conservative substitution Thr245Ser resulted in a significant decrease in affinity for MPP^+. The mutants Gln241Glu, Phe244Tyr, and Gln447Glu, all demonstrated no significant change in affinity for MPP^+.

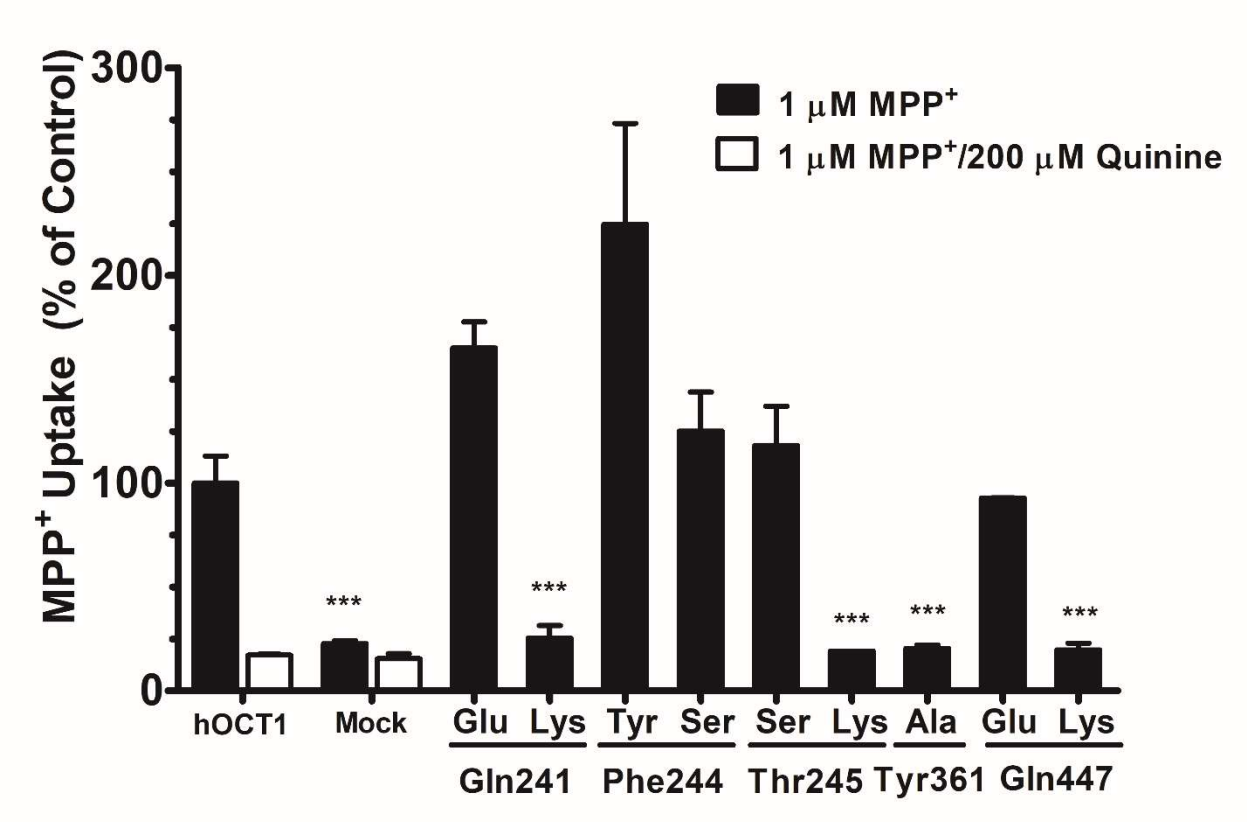


Figure 4.11 Functional screen of CHO-hOCT1 wild type and mutant expressing cell lines.

CHO cells were treated with transport buffer containing 1 μM [^{3}H] MPP^+ (0.25 μCi/mL) in the absence or presence of inhibitor (quinine) for 10 min. Conservative and non-conservative mutations appear above original amino acid position. Data shown as duplicate values ± SD. ** denotes $p<0.01$; *** denotes $p<0.001$; compared against wild type control by one-way ANOVA followed by post-hoc Dunnett's t-test.

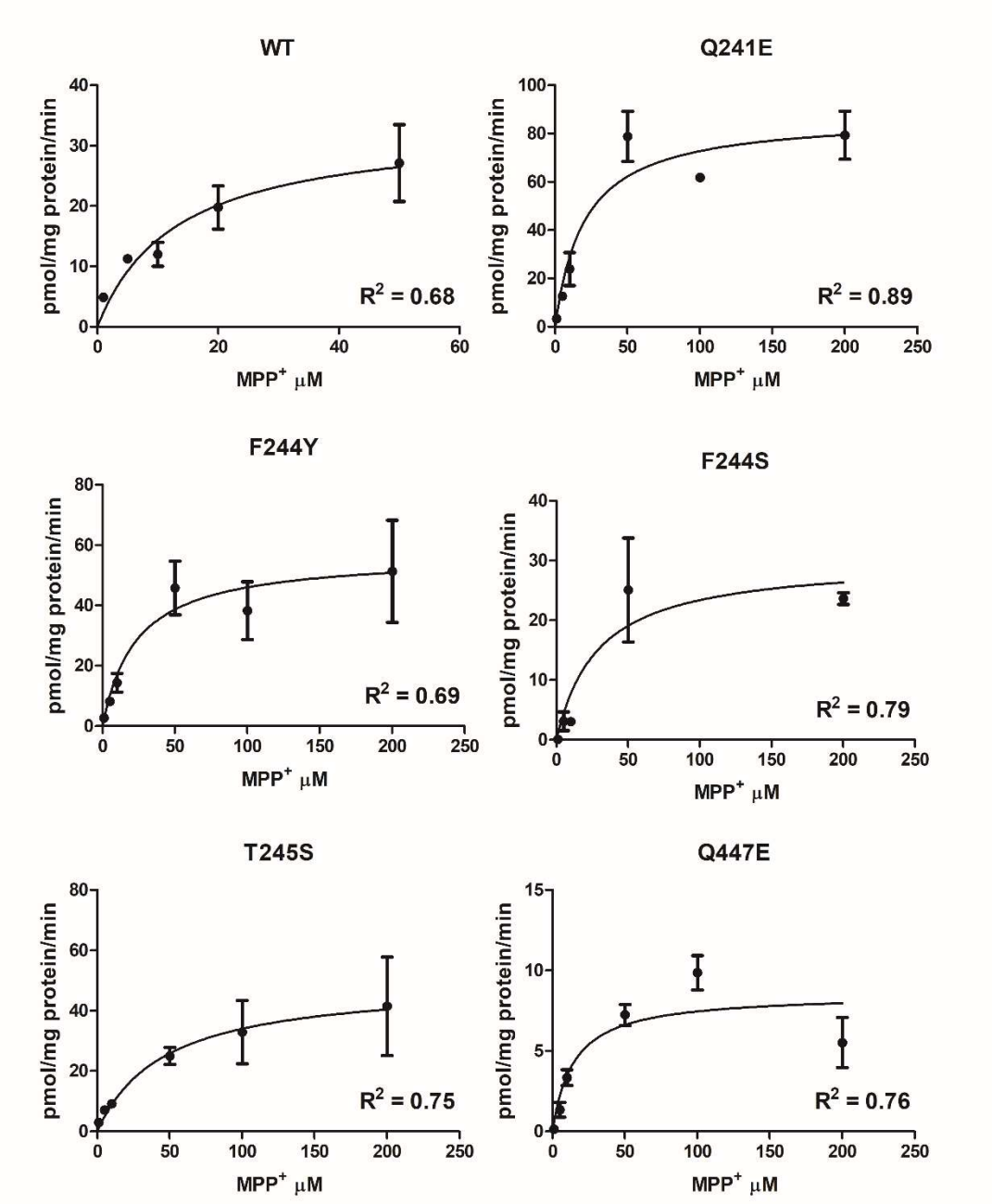


Figure 4.12 Representative dose response curves for wild type and mutant hOCT1.

Michaelis-Menten kinetics of [^{3}H] MPP$^+$ transport (1–200 μM) for hOCT1 and hOCT1 mutants in stably transfected CHO cells.

.

Table 4.7 Summary of K_m estimates for hOCT1 constructs.

hOCT1 Transporter	K_m (μM)
WT	16.3 ± 2.5
Gln241Glu	18.2 ± 1.2
Phe244Tyr	24 ± 0.32
Phe244Ser	33.4 ± 5*
Thr245Ser	37.4 ± 6.4*
Gln447Glu	14.3 ± 2.6

Mean K_m estimates acquired from triplicate experiments ± SE.
* denotes $p < 0.05$ compared against wild type control by one-way ANOVA followed by post-hoc Dunnett's t-test.

4.C.5 Genomic integration of non-functional hOCT1 mutant constructs

To eliminate failed genomic DNA integration as an explanation for the lack of transport activity in non-functional hOCT1 mutants, genomic DNA was extracted and PCR amplified using the primers T7 and hOCT1 REV, that flanked 5' and 3' ends of the hOCT1 coding sequence of the pcDNA3 plasmid (hOCT1 amplicon ~1.7 kb). PCR products of the expected size (~1.7 kb) were obtained for wildtype hOCT1 and all hOCT1 mutants (Gln241Lys, Tyr361Ala, Thr245Lys, and Gln447Lys), while no product was observed for negative controls (water and pcDNA3) demonstrating that all hOCT1 plasmids had been successfully integrated (Figure 4.13).

4.C.6 Membrane targeting of hOCT1-GFP fusion construct

The full length hOCT1 cDNA fragment was gel isolated and ligated into vector pEGFP-C1 forming the plasmid pEGFP-C1/hOCT1 containing hOCT1 fused in frame to the carboxyl terminal of GFP (Figure 4.14). CHO cells expressing the hOCT1-GFP fusion construct showed strong fluorescence within the cytosol and lack of signal in the nucleus (Figure 4.15). This pattern is consistent with an intact GFP fusion construct versus expression of "free" GFP. However, no noticeable fluorescence at the plasma membrane was observed. Control transfections (lipofectamine only) showed no fluorescent signal (data not shown). In order to have a reference of the membrane localization of OCTs, MDCK cells stably transfected with a rat Oct2-GFP fusion construct from a previous study were grown and observed [159] (Figure 4.16).

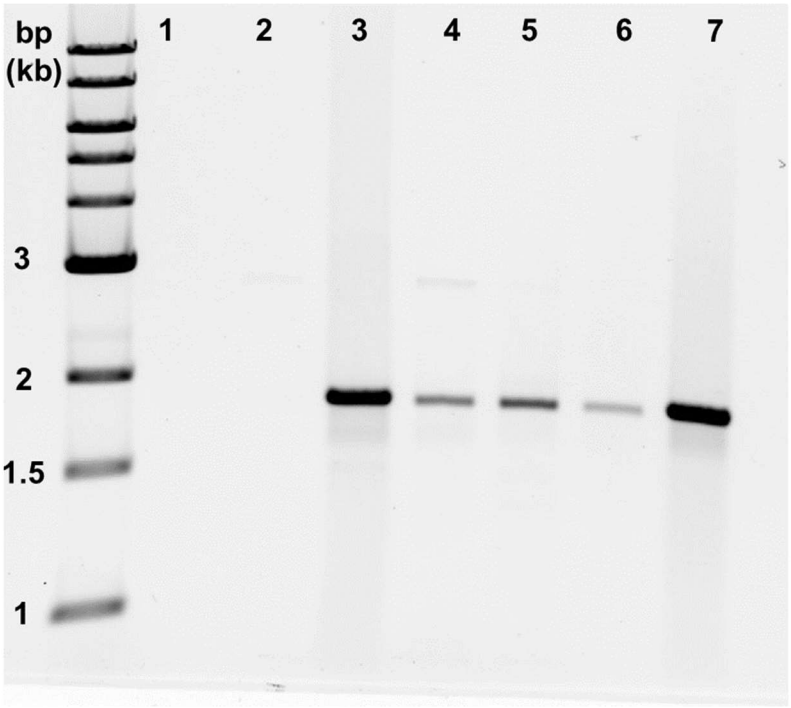


Figure 4.13 PCR analysis of genomic DNA isolated from hOCT1 cell lines.

Confirmation of successful genomic integration of mutant hOCT2 constructs that lacked transport activity. Lanes: (1) water, (2) pcDNA3, (3) hOCT1, (4) hOCT1 Gln241Lys, (5) hOCT1 Thr245Lys, (6) hOCT1 Tyr361Ala, (7) hOCT1 Gln447Lys

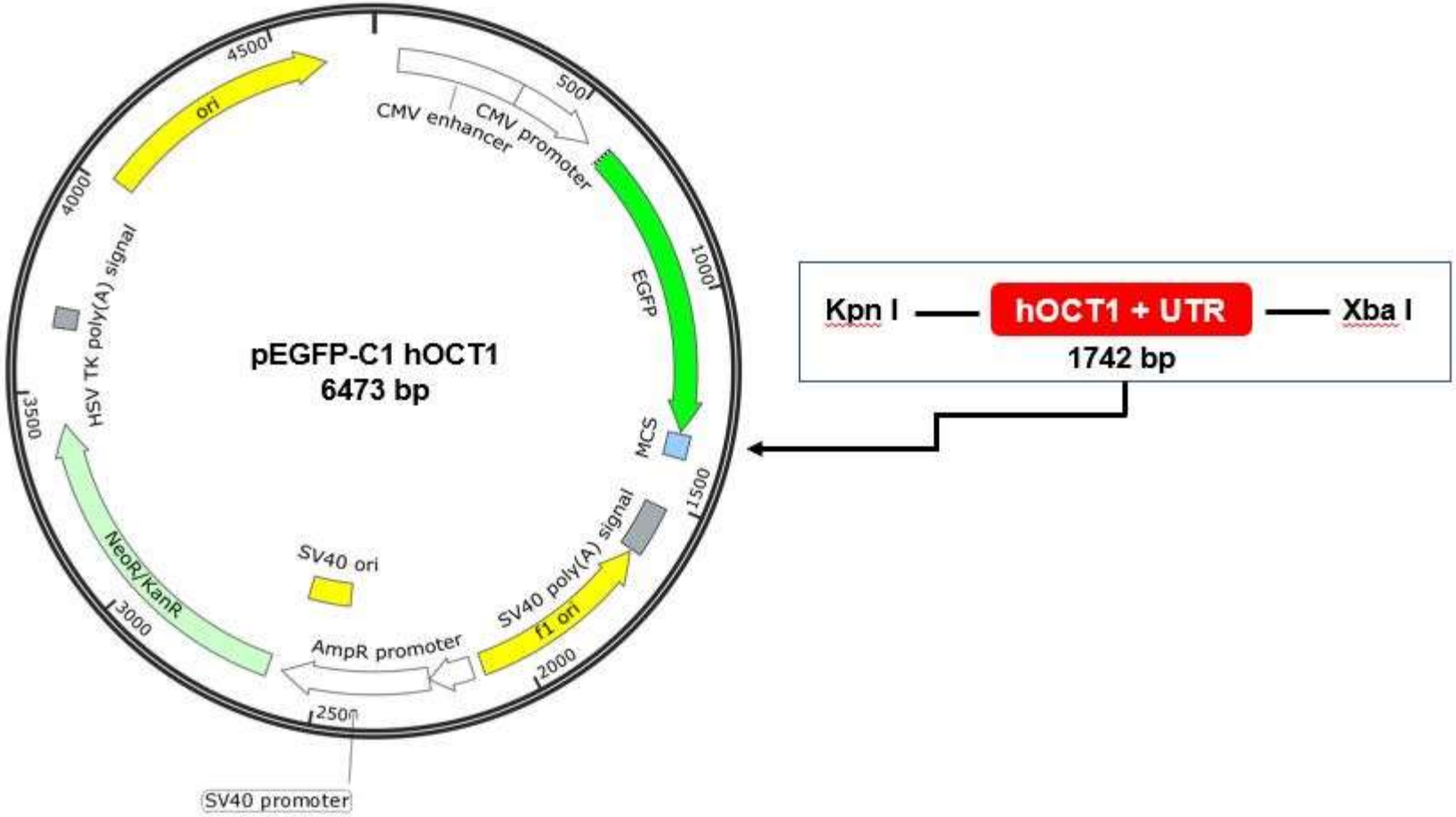


Figure 4.14 pEGFP-C1/hOCT1 fusion protein vector map.

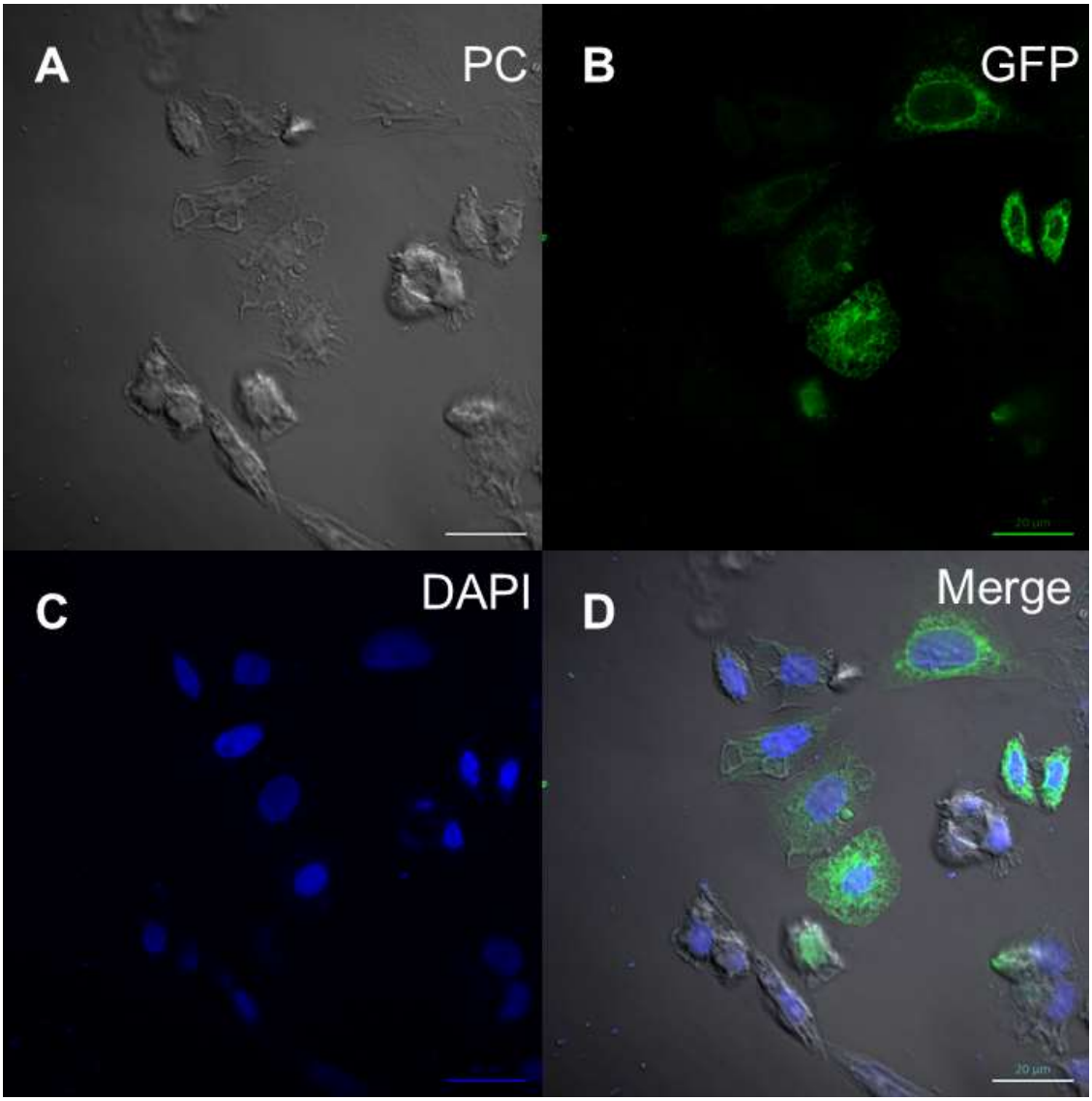


Figure 4.15 Expression patterns of pEGFP-C1/hOCT1.

CHO cells transfected with pEGFP-C1/hOCT1 were fixed, permeabilized, and mounted at 24 hours post transfection then viewed under confocal microscopy: (A) phase contrast, (B) GFP, (C) DAPI, and (D) merge. Scale bar = 20 μm

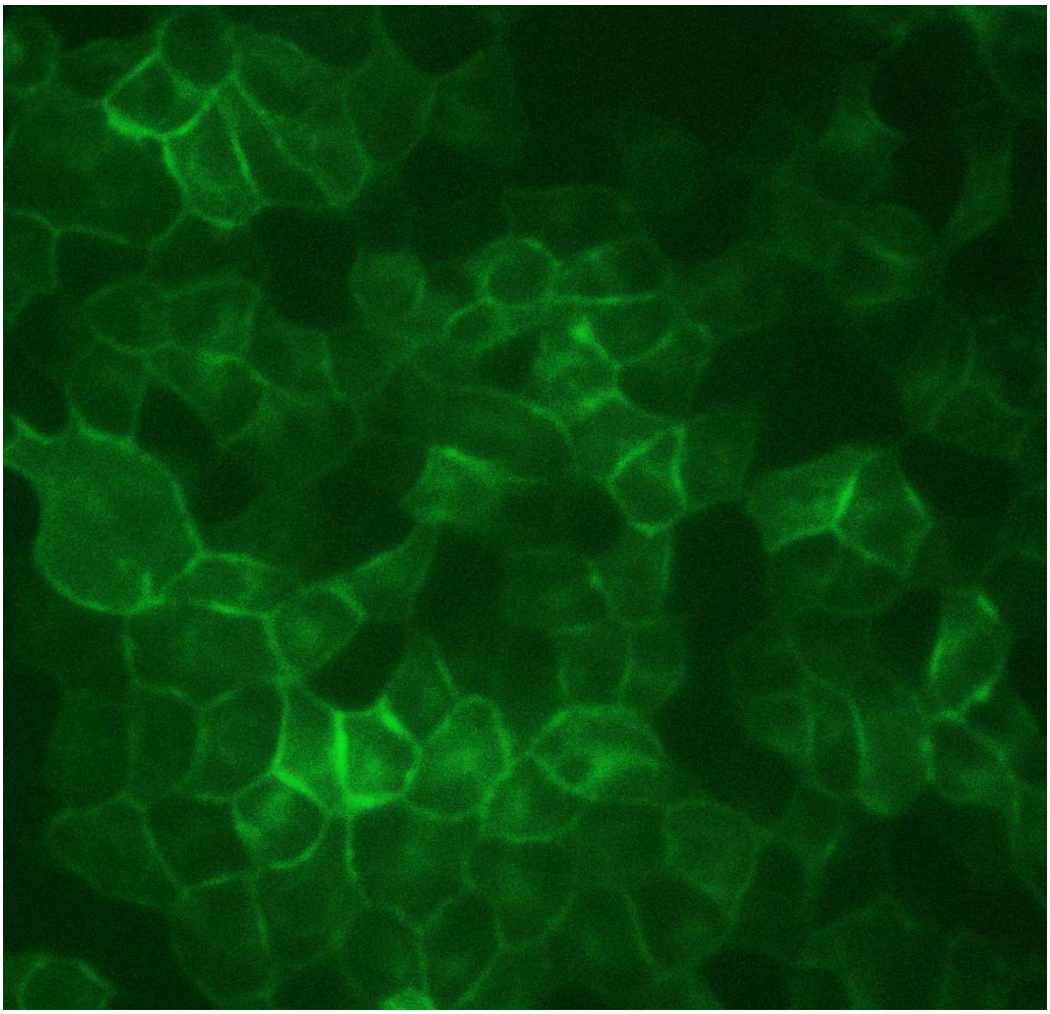


Figure 4.16 Expression of pEGFP-C3/rOct2 in MDCK cells.

MDCK cells stably transfected with pEGFP-C3/rOct2 were thawed, grown in culture for 48 hours, then observed by fluorescence microscopy (40x magnification). Observed cells were used in a study performed in reference [159]

4.D DISCUSSION

The polyspecific nature of the OCTs make them prime targets for potentially unwarranted effects of drug-drug interactions. Any insight on the physiochemical nature of the substrate interactions for these transporters will undoubtedly serve to guide the prediction of such occurrences. The importance of understanding OCT-substrate interactions has recently garnered more attention. Several important studies have identified probable residues for OCT substrate interaction through the use of homology models based on the crystallized structures of the prokaryotic MFS transporters LacY or GlpT [143,146,148,153]. Their initial findings were helpful in establishing the usefulness of this relatively novel technique for the understanding of OCT transport, however, may be limited due to low sequence identities shared between the templates used and mammalian OCTs (~15%).

Therefore, in the current study, homology models of the tertiary structure of hOCT1 were generated using the known crystal structure of PiPT serving as the template. PiPT, also a member of the MFS, was chosen as the designated template due to a number of factors including its relative sequence homology to the hOCTs (~21% identical, 40% similar), eukaryotic origin (*Piriformospora indica*), and the fact that it was crystallized in the occluded state. The occluded conformation grants the transporter maximum binding interaction sites for bound ligands. After docking MPP^+ into the generated hOCT1 models, amino acid residues were identified that formed the putative binding pocket (within a 5 Å radius surrounding the substrate) (Figure 4.6). This approach required that several assumptions be made during the *in silico* model building process including that adequate structural similarity exists between the crystallized tertiary structure of PiPT and hOCT1

and that the presence of water molecules in the occluded binding pocket was negligible and therefore not considered during the docking analysis. All models were generated based on PiPT and the hOCT1 protein sequence with transmembrane domains globally energy minimized. Amino acid residues deemed “critical” for hOCT1-MPP^+ binding interactions were identified *in silico* based on substrate proximity and interaction type (Table 4.3).

Within the proposed binding pocket, hydrophobic interactions were identified between MPP^+ and amino acid residues Gln241, Thr245, and Glu447, and one of the aromatic rings of MPP^+ was found to be involved in edge-face pi and pi-stacking interactions with Phe244 and Tyr361, respectively. Subsequently, stably transfected CHO cells expressing hOCT1 mutants were established and utilized for a series of *in vitro* kinetic assays to confirm their role in substrate binding. From the functional screening study, transport activity of MPP^+ was absent in the non-conservative substitution of Gln241, Thr245, Tyr361, and Gln447 (Figure 4.11). All conservative substituted mutants, and one non-conservative substitution retained transport function (Phe244). The MPP^+ docked hOCT1 model predicted strong interactions for Phe244 and Tyr361 (edge-face pi and pi-pi stacking, respectively). The retained transport function for both mutants of Phe244 contradicted the model’s prediction. Loss of transport function by the conservative Tyr361Ala mutation suggested that this residue may be a critical site for substrate binding. This result correlates with the MPP^+ docking data where Tyr361 was predicted to participate in the strongest substrate interactions (pi-pi stacking). However, in contrast to hOCT2, we were unable to isolate the conservative hOCT1 Tyr361Phe mutant. Thus, whether or not a similar possibility as observed for hOCT2 exists for hOCT1

for the aromatic hydroxyl group to mediate additional important interactions with other residues within the binding pocket beyond pi-pi stacking with MPP^+ and, thus, playing a significant role in forming the structure of the binding pocket, is unknown. Evaluating the transport function for the conservative substituted mutant of Tyr361 (mutant was unable to be constructed) would provide stronger support as a critical residue for MPP^+ interaction. For hOCT1 mutants retaining MPP^+ transport function, Phe244Ser and Thr245Ser displayed significantly decreased substrate affinity (Table 4.7). In turn, it is plausible to suggest that Phe244Ser and Thr245Ser are important sites for MPP^+ interaction. Future studies involving the generation of a Phe244Ser/Thr245Ser double mutant could provide additional evidence to support their importance for substrate interaction. These preliminary findings suggest that Glu241, Phe244, Thr245, Tyr361, and Gln447 are the leading candidate residues that may be involved in hOCT1-MPP^+ interactions. Among these, Thr245 holds the strongest case since its conservative substituted mutant had significantly attenuated affinity and its non-conservative mutant demonstrated a complete loss of activity for the transport of MPP^+.

The complete loss of MPP^+ transport activity by hOCT1 mutants (Gln241Lys, Thr245Lys, Tyr361Ala, and GLn447Lys) may be due to several of the following factors. The amino acid could be largely responsible for MPP^+ interactions such that when mutated will lead to the loss of transport and/or a change in the overall conformation of the binding pocket. Alternatively, there could have been issues during the transfection process leading to the absence of cDNA integration into the genome. Another possibility is that the amino acid may be critical for the structural integrity or trafficking of the transporter within the cell. If this were the case, mutations at this residue could lead to

protein misfolding that is subsequently degraded rather than integrating into the cellular membrane following its translation.

Genomic integration of intact cDNA for hOCT1 mutants was confirmed by PCR and gel electrophoresis (Figure 4.13) thus ruling out failed transfection. In order to confirm that inactive mutant hOCT1 transporters were translated and inserted into the plasma membranes of transfected mammalian cell lines, a hOCT1-GFP fusion construct was made by fusing the coding sequence of hOCT1 to the C-terminus of GFP and transfected into CHO cells. Plasma membrane targeting was achieved in earlier studies using a similarly constructed GFP fusion construct for rat Oat1 and rat Oct2 transfected into MDCK cells [159,160]. In the current study, however, plasma membrane targeting was not observed in CHO cells transiently transfected with the wildtype hOCT1-GFP fusion construct. Instead a consistent pattern of fluorescence in the cytosol was noticed. The discrepancy in what was observed compared to the prior studies perhaps may be due to differences associated with the cell line used (MDCK vs CHO cells). A future study involving the transfection of our pEGFP-hOCT1 fusion construct into MDCK cells should be considered.

For the analysis of docking known substrates with a diverse array of structural features into hOCT1 homology models, amino acids identified were unique to some substrates and shared for others (Table 4.3). For example, Glu 447 was among the group of residues that was shared across a diverse group of substrates which included MPP^+, epinephrine, metformin, quinine, and TPA. The conserved residue in rabbit Oct2 (also at position 447) was identified as a critical site for mediating TEA transport which was subsequently confirmed in a rabbit Oct2 homology model on GlpT [153]. Under

physiological conditions, the acidic side chain present in Glu477 may be anchoring the transport of positively charged compounds. Cys451, identified in a previous study as a residue important for mediating choline transport by rabbit Oct1 and verified through homology models based on the solved structure of LacY [144], was also identified in the present study (Cys450) for interacting with epinephrine and TPA. This observation is consistent chemically since both choline and TPA both contain a quaternary amine. TPA was also predicted to interact with Cys473 in the hOCT1 homology model in the current study. In a different study, the conserved residue, Cys474, in hOCT2 was demonstrated to mediate TEA transport and verified by a hOCT2 homology model generated based on the crystallized tertiary structure of GlpT [146]. Both TEA and TPA also share a similar quaternary nitrogen backbone in their chemical structures which may explain their shared interaction with cysteine in this particular binding region in hOCT transporters. From these observations, our model suggests that there may be one binding pocket along the central cavity of hOCT1. Within this binding pocket, there may be a core set of amino acids that interact with most substrates, in conjunction with additional substrate-specific amino acids that that accommodate structurally diverse substrates. Additional *in vitro* work involving transporter mutagenesis experiments and subsequent kinetic analysis for each substrate would be necessary to support the preliminary *in silico* findings.

From the *in silico* hOCT1 modeling and subsequent *in vitro* kinetic work in the current study, TMDs 5, 7, and 10 were the regions that contained the amino acids predicted to interact with MPP^+. Other OCT-substrate interaction studies identified important residues in TMDs 4, 10, and 11 [124,125,143,146,148,153]. Several factors should be considered that could help delineate these apparent disparate observations.

OCT models generated from different species of rodents were evaluated in the earlier interaction studies, thus species differences could account for the variations of identified residues. Interaction studies were conducted on different substrates. The current work generated hOCT1 models which were docked with MPP^+, while the other studies on rat and rabbit docked TEA and choline. As determined in the analysis involving docking known hOCT1 substrates, amino acid residues critical for interaction may be unique to each compound. Given the diverse substrate specificity of hOCT1, this result was not unexpected. In prior homology model studies, rodent Oct1 was modeled based on the tertiary structures of LacY and GlpT. The differences in observations may have been anticipated since the models constructed in the present study were generated by PiPT, a transporter with higher sequence identity with the mammalian OCTs. And finally, there is the fact LacY and GlpT were crystallized in the inward conformation which differs from the occluded state structure solved for PiPT. As such, amino acids that are accessible to interacting substrates during the *in silico* docking steps may vary.

In summary, a homology model for hOCT1 based on the solved structure of PiPT was successfully constructed. Through the docking of MPP^+ into the generated homology models, important residues associated with substrate binding interactions as well as the putative binding pocket were identified. Identified amino acids were further investigated in subsequent *in vitro* mutagenesis studies and kinetic analysis. The findings of the current study suggest that many substrates share both overlapping and unique interaction sites. Although differences in the identified important residues were recognized through comparisons with other similar studies, there were a few that were shared. Future work, particularly confirming successful targeting of the membrane for non-functional hOCT1

mutants, will be required to strengthen the current claims. Findings from the current study certainly lays down the foundation for future work that could ultimately offer important direction for optimizing drug design as well as mitigating the rates of OCT related drug-drug interactions.

CHAPTER 5

COMPARISON OF SUBSTRATE BINDING INTERACTIONS BETWEEN HUMAN ORGANIC CATION TRANSPORTERS 1, 2, AND 3

In human, organic cation transporters play a critical role in mediating the transport of a vast array of endogenous and exogenous compounds across barrier epithelia of the major distribution and eliminating organ systems; namely the intestine, liver, and kidney [1]. As such, OCTs, in particular OCT1, 2, and 3, have garnered additional attention from investigators hoping to better understand their roles in drug disposition and elimination. To date, due to the lack of a solved crystal structure, very little is known about the three-dimensional structure of human OCTs or substrate/protein interactions involved in their transport. Some early efforts involving the use of secondary structure information to determine important binding sites of the rat Oct1 and 2 have been conducted [124,125]. Since then, newer strategies involving computational homology modeling have been conducted to assist in forming more robust predictions as well as helping guide mutagenesis experiments [128,132]. In the current study, potentially critical amino acid residues important for transporter-substrate interactions were identified for human OCT1 and OCT2 through *in silico* molecular modeling techniques, paired with *in vitro* mutagenesis and kinetic transporter experiments.

Tertiary homology models for hOCT1 and hOCT2 were successfully generated using the recently crystallized MFS transporter, PiPT, as template. The generated models were *in silico* docked with the prototypical OCT substrate MPP^+. The most favorable

docked MPP^+ model was selected based on a series of computational validation methods and subsequently used to predict several potentially important sites for substrate-transporter interaction. This information was used to guide *in vitro* mutagenesis studies and kinetic experiments. This experimental strategy was carefully implemented for the elucidation of residues in both hOCT1 and hOCT2.

From the results obtained from the functional screening assay, four non-conservative mutations of hOCT1 (Glu241Lys, Thr245Lys, Tyr361Ala, and Gln447Lys) resulted in a complete loss of MPP^+ transport activity (Figure 4.11). For hOCT2, this was the case for two non-conservative mutants, hOCT2 Glu242Lys and Tyr362Ala, and one conservative mutant hOCT2 Tyr362Phe (Figure 3.11). In a different study conducted in hOCT3, two conservative mutants, (Trp358Phe and Asp475Glu) and two non-conservative mutants (Val40Ala and Trp358Ala) demonstrated a loss of MPP^+ transport activity [164]. Across OCT1-3, the only residue overlap for these sets of experiments was observed for hOCT1 and hOCT2 (Tyr361/Tyr362 and Gln241/Gln242). The Tyr residue at these positions in particular were both predicted to participate in the strongest interactions with MPP^+ in their respective homology models (pi-pi stacking) which correlates with this functional result acquired *in vitro*. Alternatively, the loss of MPP^+ transport activity for the conservative hOCT2 mutant, Tyr362Phe, suggests that the hydroxyl group in Tyr362 may be interacting with other residues and thus could be a major contributor to the tertiary structure of the binding pocket. Similar observations were not able to be made at the conserved site in hOCT1 (Tyr361) since the generation of the Tyr361Phe mutant was unsuccessful. The most critically involved amino acid in hOCT3-MPP^+ interactions was Trp358, where both conservative and non-conservative

substitutions yielded a loss of substrate transport [164]. Taken together, these results suggest that hOCT1 and hOCT2 share a similar binding pocket with one another, whereas, the binding pocket for hOCT3 appears unique.

For mutants that retained transport activity, saturation analysis was conducted to evaluate potential changes in transporter affinity for MPP^+. When compared with wildtype (K_m = 16.3 ± 2.5), hOCT1 mutants that were observed to have a significant decrease in transporter affinity was the non-conservative substitution Phe244Ser and the conservative substitution Thr245Ser (K_m = 33.4 ± 5 and 37.4 ± 6.4, respectively) (Table 4.7). In hOCT2, only the non-conservative substitution Tyr245Ala resulted in a significant change in affinity for MPP^+ (K_m = 36.5 ± 5) (Table 3.7). In hOCT3, the conservative mutant Val40Leu and non-conservative mutants Phe36Ala, Glu451Ala, and the double mutant Val40Leu/Glu451Ala showed a significant change in substrate affinity [164]. The double mutant in hOCT3 confirmed Val40 and Glu451 importance in binding interactions since the affinity was lowered significantly more when both mutations were changed compared to each mutant changed individually.

The homology models for hOCT1, 2, and 3 were further evaluated by docking known substrates with disparate structures into each population of 100 models to determine the presence of alternative and/or additional critical amino acid residues in the binding pocket(s). Epinephrine, metformin, serotonin, and TPA were docked into all three OCT models. Additional compounds, cimetidine and quinine, were docked into hOCT1 and hOCT2. Several amino acids, which made up the “core binding residues” based on their high frequency of overlap across the different docked compounds for each transporter were identified: hOCT1: Phe244, Asp357, Tyr361, and GLn447 (Table 5.1);

hOCT2: Tyr245, Ser358, Tyr362, and Glu448 (Table 5.2); and hOCT3: Val40, Met248, Trp358, and Asp478 (Table 5.3). Amongst this list across hOCT1-3, aspartic acids and glutamic acids, particularly in TMDs 10 and 11, seem to be important for substrate interactions. These amino acids with acidic side chains, under physiologic conditions (pH 7.4) are likely to anchor cations as they translocate across the membrane through the transporter.

Table 5.1 hOCT1 substrate docking summary[a].

Residue	MPP^+	Cimetidine	Epinephrine	Metformin	Quinine	5-HT	TPA
Trp16		x					
Gln20			x				
Leu23					x		
Asn156		x					
Phe159		x					
Trp217		x			x		
Gln241	x					x	
Phe244	x	x	x	x	x	x	x
Thr245	x						
Trp354				x			
Asp357		x	x	x	x	x	x
Ser358						x	
Tyr361	x	x	x	x	x	x	x
Gln362		x				x	
Ile444						x	x
Gln447	x		x	x	x		x
Ile449							x
Cys450			x				x
Cys473				x	x	x	
Asp474		x					

[a] Data acquired from Figure 4.7 and Table 4.3

Table 5.2 hOCT2 substrate docking summary[a].

Residue	MPP^+	Cimetidine	Epinephrine	Metformin	Quinine	5-HT	TPA
Phe24					**x**		**x**
Asn157		**x**			**x**		
Phe160					**x**		**x**
Gln242	**x**				**x**		
Tyr245	**x**	**x**	**x**		**x**	**x**	**x**
Thr246	**x**						
Ser358		**x**	**x**	**x**		**x**	
Tyr362	**x**	**x**	**x**	**x**	**x**	**x**	
Gln363						**x**	
Glu387						**x**	
Glu448	**x**	**x**	**x**	**x**		**x**	
Cys451						**x**	
Cys474							**x**
Asp475		**x**					

[a] Data acquired from Figure 3.7 and Table 3.3

Table 5.3 hOCT3 substrate docking summary[a].

Residue	MPP^+	Epinephrine	Metformin	5-HT	TPA
Phe36	**x**	**x**			
Val40	**x**	**x**		**x**	
Asn162		**x**		**x**	
Met248		**x**	**x**	**x**	
Trp358	**x**		**x**		**x**
Gln366		**x**			
Glu451	**x**				
Ser474			**x**		
Cys477		**x**			
Asp478	**x**	**x**	**x**	**x**	

[a] Data acquired from reference [164]

It was previously reported that transport activity was completely abolished by an Asp478 mutation in hOCT3 [164]. Through sequence alignment, the homologous site in hOCT2 was identified as Asp475. The analogous conservative substitution of hOCT2 Asp475 was generated and stably expressed in CHO cells for functional screening studies. In stark contrast to the hOCT3 results, the conserved mutant in hOCT2 showed no difference from wild-type hOCT2 in transport activity of MPP^+ (data not shown). This finding was supported by our hOCT2 *in silico* model wherein Asp475 was located outside of the binding pocket and not predicted to interact with MPP^+. The difference in transporter function and affinity observed between hOCT3 Asp478Glu and hOCT2 Asp475Glu suggests that the critical residues for MPP^+-transporter interaction may vary depending on the OCT paralog even for the same substrate and supports the contention that the binding pocket in hOCT3 is distinct from that for hOCT1 and hOCT2. Despite a high degree of sequence similarity (70%) and identity (51%) between hOCT2 and hOCT3, the conserved aspartic acid residue (position 475 in hOCT2 and position 478 in hOCT3) previously demonstrated to be essential for MPP^+ interaction with hOCT3 appears to exert no influence on MPP^+ interaction with hOCT2.

The whole story detailing the most accurate depiction of the nature of the physiochemical interactions for hOCT1, 2, and 3 is far from complete. The utilization of homology models with the most closely related available transporter templates is currently the leading strategy in achieving the overarching goal of the elucidation of the amino acids critical for protein-ligand interaction. A comprehensive list of future work is necessary for reaching stronger conclusions on the current hOCT interaction studies. This includes additional studies to resolve the issue related to evaluating transporter targeting to plasma

membrane. Acquiring this information will significantly dictate the validity of the claims made for the hOCT non-functional mutants. Given the lack of specificity of commercial antibodies tested and the inconclusive results of the GFP fusion construct studies, an alternative approach could be the addition of a polypeptide tag with a known commercial antibody (*e.g.* FLAG, c-Myc, 6x His) to the hOCT proteins. The establishment of double mutants for hOCT1 and 2 will be helpful in providing additional valuable kinetic information for functioning single mutants showing attenuated affinity. This analysis will in turn determine any potential changes in double-mutant affinity for MPP^+ which could offer further insight to the significance for specific residues involved with transporter-substrate interaction. Finally, the additional amino acid residues that were identified in the analysis of docking known structurally disparate hOCT substrates will need to be further investigated. This can be conducted through the generation of stably transfect mutants based on the additional residues identified and subsequent kinetic transport analysis of the structurally disparate substrates.

The data collected from the current study in addition to the proposed future experiments will bring forward new information regarding the substrate binding site of hOCT1-3 of which will provide the necessary clues for their underlying mechanism of transport. The identified amino acid residues that contribute to substrate binding may offer useful insight to the transporter-substrate recognition by other members of the SLC22 family owing to their similarities in sequence homology. In the end, unveiling the critical residues for hOCT1-3 will steer the future of drug design by improving safety/efficacy as well as strengthening our predictions that eventually could lead to reductions in the rates of harmful drug-drug interactions.

LITERATURE CITED

[1] Lai RE, Jay CE, Sweet DH. Organic solute carrier 22 (SLC22) family: Potential for interactions with food, herbal/dietary supplements, endogenous compounds, and drugs. J food drug Anal 2018;26:S45-S60.

[2] HUGO. Human genome organization gene nomencalture committee. http://www.genenames.org/cgi-bin/genefamilies/set/752). Accessed February 28, 2018.

[3] Koepsell H. The SLC22 family with transporters of organic cations, anions and zwitterions. Mol Aspects Med 2013;34:413-435.

[4] Jonker JW, Schinkel AH. Pharmacological and physiological functions of the polyspecific organic cation transporters: OCT1, 2, and 3 (SLC22A1-3). J Pharmacol Exp Ther 2004;308:2-9.

[5] Keller T, Egenberger B, Gorboulev V, Bernhard F, Uzelac Z, Gorbunov D, Wirth C, Koppatz S, Dötsch V, Hunte C, Sitte HH, Koepsell H. The large extracellular loop of organic cation transporter 1 influences substrate affinity and is pivotal for oligomerization. J Biol Chem 2011;286:37874-37886.

[6] Koepsell H, Lips K, Volk C. Polyspecific organic cation transporters: structure, function, physiological roles, and biopharmaceutical implications. Pharm Res 2007;24:1227-1251.

[7] Minuesa G, Volk C, Molina-Arcas M, Gorboulev V, Erkizia I, Arndt P, Clotet B, Pastor-Anglada M, Koepsell H, Martinez-Picado J. Transport of lamivudine [(-)- -L-2',3'-dideoxy-3'-thiacytidine] and high-affinity interaction of nucleoside reverse transcriptase inhibitors with human organic cation transporters 1, 2, and 3. J Pharmacol Exp Ther 2009;329:252-261.

[8] Nies AT, Koepsell H, Damme K, Schwab M. Organic cation transporters (OCTs, MATEs), in vitro and in vivo evidence for the importance in drug therapy. Handb Exp Pharmacol 2011:105-167.

[9] Sweet DH. Organic anion transporter (Slc22a) family members as mediators of toxicity. Toxicol Appl Pharmacol 2005;204:198-215.

[10] Sweet D. Renal organic cation and anion transport: From physiology to genes. In: McQueen CA, ed. *Comprehensive Toxicology*. 2nd ed. Oxford: Academic Press; 2010:23-53.

[11] Sweet DH. Organic anion transporter (Slc22a) family members as mediators of toxicity. Toxicol Appl Pharmacol 2005;204:198-215.

[12] VanWert AL, Gionfriddo MR, Sweet DH. Organic anion transporters: Discovery, pharmacology, regulation and roles in pathophysiology. Biopharm Drug Dispos 2010;31:1-71.

[13] Wang L, Sweet DH. Renal organic anion transporters (SLC22 family): Expression, regulation, roles in toxicity, and impact on injury and disease. AAPS J 2013;15:53-69.

[14] Farthing CA, Sweet DH. Expression and function of organic cation and anion transporters (SLC22 family) in the CNS. Curr Pharm Des 2014;20:1472-1486.

[15] Gorboulev V, Ulzheimer JC, Akhoundova a, Ulzheimer-Teuber I, Karbach U, Quester S, Baumann C, Lang F, Busch a E, Koepsell H. Cloning and characterization of two human polyspecific organic cation transporters. DNA Cell Biol 1997;16:871-881.

[16] Green RM, Lo K, Sterritt C, Beier DR. Cloning and functional expression of a mouse liver organic cation transporter. Hepatology 1999;29:1556-1562.

[17] Gründemann D, Gorboulev V, Gambaryan S, Veyhl M, Koepsell H. Drug excretion mediated by a new prototype of polyspecific transporter. Nature 1994;372:549-552.

[18] Zhang L, Dresser MJ, Gray AT, Yost SC, Terashita S, Giacomini KM. Cloning and functional expression of a human liver organic cation transporter. Mol Pharmacol 1997;51:913-921.

[19] Meyer-Wentrup F, Karbach U, Gorboulev V, Arndt P, Koepsell H. Membrane localization of the electrogenic cation transporter rOCT1 in rat liver. Biochem Biophys Res Commun 1998;248:673-678.

[20] Urakami Y, Okuda M, Masuda S, Saito H, Inui K-I. Functional characteristics and membrane localization of rat multispecific organic cation transporters, OCT1 and OCT2, mediating tubular secretion of cationic drugs. J Pharmacol Exp Ther 1998;287:800-805.

[21] Mooslehner KA, Allen ND. Cloning of the mouse organic cation transporter 2 gene, Slc22a2, from an enhancer-trap transgene integration locus. Mamm Genome 1999;10:218-224.

[22] Sweet DH, Walsh RH, Pritchard JB. Expression cloning and characterization of a renal organic cation transporter from rat. FASEB J 1996;11:A278.

[23] Sweet DH, Miller DS, Pritchard JB. Ventricular choline transport: A role for organic cation transporter 2 expressed in choroid plexus. J Biol Chem 2001;276:41611-41619.

[24] Alnouti Y, Petrick JS, Klaassen CD. Tissue distribution and ontogeny of organic cation transporters in mice. Drug Metab Dispos 2006;34:477-482.

[25] Prasad B, Johnson K, Billington S, Lee C, Chung GW, Brown CDA, Kelly EJ, Himmelfarb J, Unadkat JD. Abundance of drug transporters in the human kidney cortex as quantified by quantitative targeted proteomics. Drug Metab Dispos 2016;44:1920-1924.

[26] Sweet DH, Pritchard JB. rOCT2 is a basolateral potential-driven carrier, not an organic cation/proton exchanger. Am J Physiol 1999;277:F890-F898.

[27] Sugawara-Yokoo M, Urakami Y, Koyama H, Fujikura K, Masuda S, Saito H, Naruse T, Inui K, Takata K. Differential localization of organic cation transporters rOCT1 and rOCT2 in the basolateral membrane of rat kidney proximal tubules. Histochem Biol 2000;114:175-180.

[28] Sweet DH, Miller DS, Pritchard JB. Basolateral localization of organic cation transporter 2 in intact renal proximal tubules. Am J Physiol Renal Physiol 2000;279:F826-834.

[29] Kekuda R, Prasad PD, Wu X, Wang H, Fei YJ, Leibach FH, Ganapathy V. Cloning and functional characterization of a potential-sensitive, polyspecific organic cation transporter (OCT3) most abundantly expressed in placenta. J Biol Chem 1998;273:15971-15979.

[30] Verhaagh S, Schweifer N, Barlow DP, Zwart R. Cloning of the mouse and human solute carrier 22a3 (Slc22a3/SLC22A3) identifies a conserved cluster of three organic cation transporters on mouse chromosome 17 and human 6q26-q27. Genomics 1999;55:209-218.

[31] Wu X, Huang W, Ganapathy ME, Wang H, Kekuda R, Conway SJ, Leibach FH, Ganapathy V. Structure, function, and regional distribution of the organic cation transporter OCT3 in the kidney. Am J Physiol Renal Physiol 2000;279:F449-458.

[32] Sekine T, Watanabe N, Hosoyamada M, Kanai Y, Endou H. Expression cloning and characterization of a novel multispecific organic anion transporter. J Biol Chem 1997;272:18526-18529.

[33] Sweet DH, Wolff NA, Pritchard JB. Expression cloning and characterization of ROAT1. The basolateral organic anion transporter in rat kidney. J Biol Chem 1997;272:30088-30095.

[34] Cihlar T, Lin DC, Pritchard JB, Fuller MD, Mendel DB, Sweet DH. The antiviral nucleotide analogs cidofovir and adefovir are novel substrates for human and rat renal organic anion transporter 1. Mol Pharmacol 1999;56:570-580.

[35] Lopez-Nieto CE, You G, Bush KT, Barros EJG, Beier DR, Nigam SK. Molecular cloning and characterization of NKT, a gene product related to the organic cation transporter family that is almost exclusively expressed in the kidney. J Biol Chem 1997;272:6471-6478.

[36] Reid G, Wolff NA, Dautzenberg FM, Burckhandt G. Cloning of a human renal p-aminohippurate transporter, hROAT1. Kidney Blood Press Res 1998;21:233-237.

[37] Kojima R, Sekine T, Kawachi M, Cha SH, Suzuki Y, Endou H. Immunolocalization of multispecific organic anion transporters, OAT1, OAT2, and OAT3, in rat kidney. J Am Soc Nephrol 2002;13:848-857.

[38] Motohashi H, Sakurai Y, Saito H, Masuda S, Urakami Y, Goto M, Fukatsu A, Ogawa O, Inui K. Gene expression levels and immunolocalization of organic ion transporters in the human kidney. J Am Soc Nephrol 2002;13:866-874.

[39] Sweet DH, Miller DS, Pritchard JB. Localization of an organic anion transporter-

GFP fusion construct (rROAT1-GFP) in intact proximal tubules. Am J Physiol 1999;276:F864-73.

[40] Simonson GD, Vincent AC, Roberg KJ, Huang Y, Iwanij V. Molecular cloning and characterization of a novel liver-specific transport protein. J Cell Sci 1994;107:1065-1072.

[41] Enomoto A, Takeda M, Shimoda M, Narikawa S, Kobayashi Y, Kobayashi Y, Yamamoto T, Sekine T, Cha SH, Niwa T, Endou H. Interaction of human organic anion transporters 2 and 4 with organic anion transport inhibitors. J Pharmacol Exp Ther 2002;301:797-802.

[42] Kobayashi Y, Ohshiro N, Shibusawa A, Sasaki T, Tokuyama S, Sekine T, Endou H, Yamamoto T. Isolation, characterization and differential gene expression of multispecific organic anion transporter 2 in mice. Mol Pharmacol 2002;62:7-14.

[43] Buist SCN, Cherrington NJ, Choudhuri S, Hartley DP, Klaassen CD. Gender-specific and developmental influences on the expression of rat organic anion transporters. J Pharmacol Exp Ther 2002;301:145-151.

[44] Kobayashi Y, Hirokawa N, Ohshiro N, Sekine T, Sasaki T, Tokuyama S, Endou H, Yamamoto T. Differential gene expression of organic anion transporters in male and female rats. Biochem Biophys Res Commun 2002;290:482-487.

[45] Sekine T, Cha SH, Tsuda M, Apiwattanakul N, Nakajima N, Kanai Y, Endou H. Identification of multispecific organic anion transporter 2 expressed predominantly in the liver. FEBS Lett 1998;429:179-182.

[46] Kusuhara H, Sekine T, Utsunomiya-Tate N, Tsuda M, Kojima R, Cha SH, Sugiyama Y, Kanai Y, Endou H. Molecular cloning and characterization of a new multispecific organic anion transporter from rat brain. J Biol Chem 1999;274:13675-13680.

[47] Cha SH, Sekine T, Fukushima JI, Kanai Y, Kobayashi Y, Goya T, Endou H. Identification and characterization of human organic anion transporter 3 expressing predominantly in the kidney. Mol Pharmacol 2001;59:1277-1286.

[48] Sweet DH, Miller DS, Pritchard JB, Fujiwara Y, Beier DR, Nigam SK. Impaired organic anion transport in kidney and choroid plexus of organic anion transporter 3 (Oat3 (Slc22a8)) knockout mice. J Biol Chem 2002;277:26934-26943.

[49] Sweet DH, Chan LMS, Walden R, Yang X-P, Miller DS, Pritchard JB. Organic anion transporter 3 (Slc22a8) is a dicarboxylate exchanger indirectly coupled to the Na+ gradient. Am J Physiol Renal Physiol 2003;284:F763-769.

[50] Cha SH, Sekine T, Kusuhara H, Yu E, Kim JY, Kim DK, Sugiyama Y, Kanai Y, Endou H. Molecular cloning and characterization of multispecific organic anion transporter 4 expressed in the placenta. J Biol Chem 2000;275:4507-4512.

[51] Babu E, Takeda M, Narikawa S, Kobayashi Y, Enomoto A, Tojo A, Cha SH, Sekine T, Sakthisekaran D, Endou H. Role of human organic anion transporter 4 in the transport of ochratoxin A. Biochim Biophys Acta 2002;1590:64-75.

[52] Ekaratanawong S, Anzai N, Jutabha P, Miyazaki H, Noshiro R, Takeda M, Kanai Y, Sophasan S, Endou H. Human organic anion transporter 4 is a renal apical organic anion / dicarboxylate exchanger in the proximal tubules. J Pharmacol Sci 2004;94:297-304.

[53] Hagos Y, Stein D, Ugele B, Burckhardt G, Bahn A. Human renal organic anion transporter 4 operates as an asymmetric urate transporter. J Am Soc Nephrol 2007;18:430-439.

[54] Mori K, Ogawa Y, Ebihara K, Aoki T, Tamura N, Sugawara A, Kuwahara T, Ozaki S, Mukoyama M, Tashiro K, Tanaka I, Nakao K. Kidney-specific expression of a novel mouse organic cation transporter-like protein. FEBS Lett 1997;417:371-374.

[55] Enomoto A, Kimura H, Chairoungdua A, Shigeta Y, Jutabha P, Ho Cha S, Hosoyamada M, Takeda M, Sekine T, Igarashi T, Matsuo H, Kikuchi Y, Oda T, Ichida K, Hosoya T, Shimokata K, Niwa T, Kanai Y, Endou H. Molecular identification of a renal urate–anion exchanger that regulates blood urate levels. Nature 2002;417:447-452.

[56] Hosoyamada M, Ichida K, Enomoto A. Function and localization of urate transporter 1 in mouse kidney. J Am Soc Nephrol 2004;15:261-268.

[57] Torres AM, Mac Laughlin M, Muller A, Brandoni A, Anzai N, Endou H. Altered renal elimination of organic anions in rats with chronic renal failure. Biochim Biophys Acta - Mol Basis Dis 2005;1740:29-37.

[58] Matsuzaki T, Watanabe H, Yoshitome K, Morisaki T, Hamada A, Nonoguchi H, Kohda Y, Tomita K, Inui K, Saito H. Downregulation of organic anion transporters in rat kidney under ischemia/reperfusion-induced acute [corrected] renal failure. Kidney Int 2007;71:539-547.

[59] Matsuzaki T, Morisaki T, Sugimoto W, Yokoo K, Sato D, Nonoguchi H, Tomita K, Terada T, Inui K, Hamada A, Saito H. Altered pharmacokinetics of cationic drugs caused by down-regulation of renal rat organic cation transporter 2 (Slc22a2) and rat multidrug and toxin extrusion 1 (Slc47a1) in ischemia/reperfusion-induced acute kidney injury. Drug Metab Dispos 2008;36:649-654.

[60] Naud J, Michaud J, Beauchemin S, Hébert M-J, Roger M, Lefrancois S, Leblond FA, Pichette V. Effects of chronic renal failure on kidney drug transporters and cytochrome P450 in rats. Drug Metab Dispos 2011;39:1363-1369.

[61] Schneider R, Sauvant C, Betz B, Otremba M, Fischer D, Holzinger H, Wanner C, Galle J, Gekle M. Downregulation of organic anion transporters OAT1 and OAT3 correlates with impaired secretion of para-aminohippurate after ischemic acute renal failure in rats. http://www.physiology.org/doi/pdf/10.1152/ajprenal.00473.2006. Accessed February 27, 2018.

[62] Brandoni A, Torres AM. Altered Renal Expression of Relevant Clinical Drug Transporters in Different Models of Acute Uremia in Rats. Role of Urea Levels. Cell Physiol Biochem 2015;36:907-916.

[63] Ma L, Zhao L, Hu H, Qin Y, Bian Y, Jiang H, Zhou H, Yu L, Zeng S. Interaction of five anthraquinones from rhubarb with human organic anion transporter 1 (SLC22A6) and 3 (SLC22A8) and drug-drug interaction in rats. J Ethnopharmacol 2014;153:864-871.

[64] Filipski KK, Loos WJ, Verweij J, Sparreboom A. Interaction of cisplatin with the human organic cation transporter 2. Clin Cancer Res 2008;14:3875-3880.

[65] Deguchi T, Kusuhara H, Takadate A, Endou H, Otagiri M, Sugiyama Y. Characterization of uremic toxin transport by organic anion transporters in the kidney. Kidney Int 2004;65:162-174.

[66] Mulato AS, Ho ES, Cihlar T. Nonsteroidal anti-inflammatory drugs efficiently reduce the transport and cytotoxicity of adefovir mediated by the human renal organic anion transporter 1. J Pharmacol Exp Ther 2000;295:10-15.

[67] Pan X, Wang L, Gründemann D, Sweet DH. Interaction of ethambutol with human organic cation transporters of the SLC22 family indicates potential for drug-drug interactions during antituberculosis therapy. Antimicrob Agents Chemother 2013;57:5053-5059.

[68] Wang L, Sweet DH. Potential for food-drug interactions by dietary phenolic acids on human organic anion transporters 1 (SLC22A6), 3 (SLC22A8), and 4 (SLC22A11). Biochem Pharmacol 2012;84:1088-1095.

[69] Wang L, Sweet DH. Competitive inhibition of human organic anion transporters 1 (SLC22A6), 3 (SLC22A8) and 4 (SLC22A11) by major components of the medicinal herb Salvia miltiorrhiza (Danshen). Drug Metab Pharmacokinet 2013;28:220-228.

[70] Misaka S, Knop J, Singer K, Hoier E, Keiser M, Müller F, Glaeser H, König J, Fromm MF. The nonmetabolized β-Blocker nadolol is a substrate of OCT1, OCT2, MATE1, MATE2-K, and P-glycoprotein, but not of OATP1B1 and OATP1B3. Mol Pharm 2016;13:512-519.

[71] Watanabe H, Sakaguchi Y, Sugimoto R, Kaneko K ichi, Iwata H, Kotani S, Nakajima M, Ishima Y, Otagiri M, Maruyama T. Human organic anion transporters function as a high-capacity transporter for p-cresyl sulfate, a uremic toxin. Clin Exp Nephrol 2014;18:814-820.

[72] Wang L, Pan X, Sweet DH. The anthraquinone drug rhein potently interferes with organic anion transporter-mediated renal elimination. Biochem Pharmacol 2013;86:991-996.

[73] Windass AS, Lowes S, Wang Y, Brown CD. The contribution of organic anion transporters OAT1 and OAT3 to the renal uptake of rosuvastatin. J Pharmacol Exp Ther 2007;322:1221-1227.

[74] Li Z, Wang K, Zheng J, Cheung FSG, Chan T, Zhu L, Zhou F. Interactions of the active components of Punica granatum (pomegranate) with the essential renal and hepatic human solute carrier transporters. Pharm Biol 2014;52:1510-1517.

[75] Yang C, Wang S, Guo X, Sun J, Liu L, Wu L. Simultaneous determination of seven

anthraquinones in rat plasma by ultra high performance liquid chromatography-tandem mass spectrometry and pharmacokinetic study after oral administration of semen cassiae extract. J Ethnopharmacol 2015;169:305-313.

[76] Nakamura T, Takahashi M, Niigata R, Yamashita K, Kume M, Hirai M, Yasui H. Changes in blood concentrations of trace metals in cancer patients receiving cisplatin-based chemotherapy. Biomed Reports 2016;5:737-744.

[77] Mabuchi H, Nakahashi H. Determination of 3-carboxy-4-methyl-5-propyl-2-furanpropanoic acid, a major endogenous ligand substance in uremic serum, by high-performance liquid chromatography with ultraviolet detection. J Chromatogr B Biomed Sci Appl 1987;415:110-117.

[78] Bedada SK, Neerati P. Evaluation of the effect of quercetin treatment on CYP2C9 enzyme activity of diclofenac in healthy human volunteers. Phyther Res 2018;32:305-311.

[79] Nuernberg B, Koehler G, Brune K. Pharmacokinetics of diflunisal in patients. Clin Pharmacokinet 1991;20:81-89.

[80] Peloquin CA, Bulpitt AE, Jaresko GS, Jelliffe RW, Childs JM, Nix DE. Pharmacokinetics of ethambutol under fasting conditions, with food, and with antacids. Antimicrob Agents Chemother 1999;43:568-572.

[81] Zhu M, Burman WJ, Starke JR, Stambaugh JJ, Steiner P, Bulpitt AE, Ashkin D, Auclair B, Berning SE, Jelliffe RW, Jaresko GS, Peloquin CA. Pharmacokinetics of ethambutol in children and adults with tuberculosis. Int J Tuberc Lung Dis 2004;8:1360-1367.

[82] Barakat NS. Enhanced oral bioavailability of etodolac by self-emulsifying systems: in-vitro and in-vivo evaluation. J Pharm Pharmacol 2010;62:173-180.

[83] Yilmaz B, Erdem AF. Determination of flurbiprofen in human plasma by high-performance liquid chromatography. J Chromatogr Sci 2015;53:1443-1448.

[84] Xu W, Deng J, Qian Y, Hou XT, Zhu Z, Zhao M, Shang E, Qian D, Zeng H, Pang H, Duan J. Simultaneous determination of kaempferol, quercetin, mangiferin, gallic acid, p-hydroxybenzoic acid and chlorpheniramine maleate in rat plasma after oral administration of Mang-Guo-Zhi-Ke tablets by UHPLC-MS/MS and its application to pharmacokinetics. Biomed Chromatogr December 2017:e4155.

[85] Koenigsknecht MJ, Baker JR, Wen B, Frances A, Zhang H, Yu A, Zhao T, Tsume Y, Pai MP, Bleske BE, Zhang X, Lionberger R, Lee A, Amidon GL, Hasler WL, Sun D. In vivo dissolution and systemic absorption of immediate release ibuprofen in human gastrointestinal tract under fed and fasted conditions. Mol Pharm 2017;14:4295-4304.

[86] Olugemo K, Solorio D, Sheridan C, Young CL. Pharmacokinetics and safety of low-dose submicron indomethacin 20 and 40 mg compared with indomethacin 50 mg. Postgrad Med 2015;127:223-231.

[87] European Uremic Toxin (EUTox) Workgroup. European uremic solutes database.

http://www.uremic-toxins.org/DataBase.html. Accessed February 28, 2018.

[88] Lorier M, Magallanes L, Ibarra M, Guevara N, Vázquez M, Fagiolino P. Stereoselective pharmacokinetics of ketoprofen after oral administration of modified-release formulations in caucasian healthy subjects. Eur J Drug Metab Pharmacokinet 2016;41:787-793.

[89] Zhao D, Han D-E, Li N, Lu Y, Li T-T, Yang S, He J-K, Chen X-J. Simultaneous determination of six phenolic constituents of Danshen injection in rat plasma by LC-ESI-MS and its application to a pharmacokinetic study. Eur J Mass Spectrom 2011;17:395.

[90] Misaka S, Miyazaki N, Yatabe MS, Ono T, Shikama Y, Fukushima T, Kimura J. Pharmacokinetic and pharmacodynamic interaction of nadolol with itraconazole, rifampicin and grapefruit juice in healthy volunteers. J Clin Pharmacol 2013;53:738-745.

[91] Yilmaz B, Sahin H, Erdem AF. Determination of naproxen in human plasma by GC-MS. J Sep Sci 2014;37:997-1003.

[92] Pantuck EJ, Kuntzman R, Conney AH. Decreased concentration of phenacetin in plasma of cigarette smokers. Science 1972;175:1248-1250.

[93] Calvo AM, Prado MT de O, Dionisio TJ, Marques MP, Brozoski DT, Lanchote VL, Faria FAC, Santos CF. Effective method for the detection of piroxicam in human plasma using HPLC. Braz Oral Res 2016;30.

[94] Zhang Y, Zhang Z, Song R. The influence of compatibility of rhubarb and radix scutellariae on the pharmacokinetics of anthraquinones and flavonoids in rat plasma. Eur J Drug Metab Pharmacokinet 2017:1-10.

[95] Zhang X, Zheng W, Xu H, Huang X, Ren P, Zou H, Liu G, Wang J, Ma X. Pharmacokinetic study of representative anti-oxidative compounds from Denshen-Chuanxiong-Honghua following oral administration in rats. J Chromatogr B Anal Technol Biomed Life Sci 2017;1052:82-90.

[96] Zaid AN, Al Ramahi R, Cortesi R, Mousa A, Jaradat N, Ghazal N, Bustami R. Investigation of the bioequivalence of rosuvastatin 20 mg tablets after a single oral administration in mediterranean Arabs using a validated LC-MS/MS method. Sci Pharm 2016;84:536-546.

[97] Wang SP, Liu L, Wang LL, Jiang P, Xiang L, Zhang WD, Liu RH. Simultaneous determination of six hydrophilic components in rat plasma after oral administration of Jitai tablet by liquid chromatography-electrospray ionization-tandem mass spectrometry: Application to a pharmacokinetic study. J Chromatogr B Anal Technol Biomed Life Sci 2013;912:75-84.

[98] Li Z-H, Zhu H, Cai X-P, He D-D, Hua J-L, Ju J-M, Lv H, Ma L, Li W-L. Simultaneous determination of five triterpene acids in rat plasma by liquid chromatography-mass spectrometry and its application in pharmacokinetic study after oral administration of Folium Eriobotryae effective fraction. Biomed Chromatogr 2015;29:1791-1797.

[99] Ohtsuki S, Schaefer O, Kawakami H, Inoue T, Liehner S, Sato A, Ishiguro N, Kishimoto W, Ludwig-Schwellinger E, Ebner T, Terasaki T. Simultaneous absolute protein quantification of transporters, cytochrome P450s and UDP-glucuronosyltransferases as a novel approach for the characterization of individual human liver: comparison with mRNA levels and activities. Drug Metab Dispos 2011;40:83-92.

[100] Wang L, Prasad B, Salphati L, Chu X, Gupta A, Hop CECA, Evers R, Unadkat JD. Interspecies variability in expression of hepatobiliary transporters across human, dog, monkey, and rat as determined by quantitative proteomics. Drug Metab Dispos 2015;43:367-374.

[101] Gröer C, Brück S, Lai Y, Paulick A, Busemann A, Heidecke CD, Siegmund W, Oswald S. LC-MS/MS-based quantification of clinically relevant intestinal uptake and efflux transporter proteins. J Pharm Biomed Anal 2013;85:253-261.

[102] Koepsell H. Role of organic cation transporters in drug–drug interaction. Expert Opin Drug Metab Toxicol 2015;11:1619-1633.

[103] Somogyi A, Stockley C, Keal J, Rolan P, Bochner F. Reduction of metformin renal tubular secretion by cimetidine in man. Br J Clin Pharmacol 1987;23:545-551. http://www.ncbi.nlm.nih.gov/pubmed/3593625. Accessed June 24, 2018.

[104] Grün B, Kiessling MK, Burhenne J, Riedel K-D, Weiss J, Rauch G, Haefeli WE, Czock D. Trimethoprim-metformin interaction and its genetic modulation by OCT2 and MATE1 transporters. Br J Clin Pharmacol 2013;76:787-796.

[105] Ding Y, Jia Y, Song Y, Lu C, Li Y, Chen M, Wang M, Wen A. The effect of lansoprazole, an OCT inhibitor, on metformin pharmacokinetics in healthy subjects. Eur J Clin Pharmacol 2014;70:141-146.

[106] Matsuzaki T, Morisaki T, Sugimoto W, Yokoo K, Sato D, Nonoguchi H, Tomita K, Terada T, Inui K -i., Hamada A, Saito H. Altered pharmacokinetics of cationic drugs caused by down-regulation of renal rat organic cation transporter 2 (Slc22a2) and rat multidrug and toxin extrusion 1 (Slc47a1) in ischemia/reperfusion-induced acute kidney injury. Drug Metab Dispos 2008;36:649-654.

[107] Kim H-J, Park DJ, Kim JH, Jeong EY, Jung MH, Kim T-H, Yang JI, Lee G-W, Chung HJ, Chang S-H. Glutamine protects against cisplatin-induced nephrotoxicity by decreasing cisplatin accumulation. J Pharmacol Sci 2015;127:117-126.

[108] Chen L, Takizawa M, Chen E, Schlessinger A, Segenthelar J, Choi JH, Sali A, Kubo M, Nakamura S, Iwamoto Y, Iwasaki N, Giacomini KM. Genetic polymorphisms in organic cation transporter 1 (OCT1) in Chinese and Japanese populations exhibit altered function. J Pharmacol Exp Ther 2010;335:42-50.

[109] Zhou Y, Ye W, Wang Y, Jiang Z, Meng X, Xiao Q, Zhao Q, Yan J. Genetic variants of OCT1 influence glycemic response to metformin in Han Chinese patients with type-2 diabetes mellitus in Shanghai. Int J Clin Exp Pathol 2015;8:9533-9542. http://www.ncbi.nlm.nih.gov/pubmed/26464716. Accessed July 11, 2018.

[110] Chen EC, Liang X, Yee SW, Geier EG, Stocker SL, Chen L, Giacomini KM. Targeted disruption of organic cation transporter 3 attenuates the pharmacologic response to metformin. Mol Pharmacol 2015;88:75-83.

[111] Shirasaka Y, Lee N, Zha W, Wagner D, Wang J. Involvement of organic cation transporter 3 (Oct3/Slc22a3) in the bioavailability and pharmacokinetics of antidiabetic metformin in mice. Drug Metab Pharmacokinet 2016;31:385-388.

[112] FDA. In Vitro Metabolism- and Transporter- Mediated Drug-Drug Interaction Studies Guidance for Industry. FDA Guidance. http://www.fda.gov/Drugs/GuidanceComplianceRegulatoryInformation/Guidances/default.htm. Published 2017.

[113] EMA. Guideline on the investigation of drug interactions. Guidance Document.

[114] Christensen MMH, Brasch-Andersen C, Green H, Nielsen F, Damkier P, Beck-Nielsen H, Brosen K. The pharmacogenetics of metformin and its impact on plasma metformin steady-state levels and glycosylated hemoglobin A1c. Pharmacogenet Genomics 2011;21:837-850.

[115] Shu Y, Brown C, Castro R, Shi R, Lin E, Owen R, Sheardown S, Yue L, Burchard E, Brett C, Giacomini K. Effect of genetic variation in the organic cation transporter 1, OCT1, on metformin pharmacokinetics. Clin Pharmacol Ther 2008;83:273-280.

[116] Matthaei J, Kuron D, Faltraco F, Knoch T, Dos Santos Pereira J, Abu Abed M, Prukop T, Brockmöller J, Tzvetkov M. OCT1 mediates hepatic uptake of sumatriptan and loss-of-function *OCT1* polymorphisms affect sumatriptan pharmacokinetics. Clin Pharmacol Ther 2016;99:633-641.

[117] Tzvetkov M V, Saadatmand AR, Lötsch J, Tegeder I, Stingl JC, Brockmöller J. Genetically Polymorphic OCT1: Another Piece in the Puzzle of the Variable Pharmacokinetics and Pharmacodynamics of the Opioidergic Drug Tramadol. Clin Pharmacol Ther 2011;90:143-150.

[118] Tzvetkov M V, Saadatmand AR, Bokelmann K, Meineke I, Kaiser R, Brockmöller J. Effects of OCT1 polymorphisms on the cellular uptake, plasma concentrations and efficacy of the 5-HT3 antagonists tropisetron and ondansetron. Pharmacogenomics J 2012;12:22-29.

[119] Yee SW, Brackman DJ, Ennis EA, Sugiyama Y, Kamdem LK, Blanchard R, Galetin A, Zhang L, Giacomini KM. Influence of transporter polymorphisms on drug disposition and response: a perspective from the international transporter consortium. Clin Pharmacol Ther May 2018.

[120] Koepsell H, Endou H. The SLC22 drug transporter family. Pflugers Arch Eur J Physiol 2004;447:666-676.

[121] Schlessinger A, Khuri N, Giacomini KM, Sali A. Molecular modeling and ligand docking for solute carrier (SLC) transporters. Curr Top Med Chem 2013;13:843-856. http://www.ncbi.nlm.nih.gov/pubmed/23578028. Accessed July 11, 2018.

[122] Cavasotto CN, Phatak SS. Homology modeling in drug discovery: current trends

and applications. Drug Discov Today 2009;14:676-683.

[123] Colas C, Ung PM-U, Schlessinger A. SLC transporters: structure, function, and drug discovery. Medchemcomm 2016;7:1069-1081.

[124] Gorboulev V, Volk C, Arndt P, Akhoundova A, Koepsell H. Selectivity of the polyspecific cation transporter rOCT1 is changed by mutation of aspartate 475 to glutamate. Mol Pharmacol 1999;56:1254-1261. http://www.ncbi.nlm.nih.gov/pubmed/10570053. Accessed July 14, 2018.

[125] Gorboulev V, Shatskaya N, Volk C, Koepsell H. Subtype-specific affinity for corticosterone of rat organic cation transporters rOCT1 and rOCT2 depends on three amino acids within the substrate binding region. Mol Pharmacol 2005;67:1612-1619.

[126] Volk C, Gorboulev V, Budiman T, Nagel G, Koepsell H. Different affinities of inhibitors to the outwardly and inwardly directed substrate binding site of organic cation transporter 2. Mol Pharmacol 2003;64:1037-1047.

[127] Gorboulev V, Shatskaya N, Volk C, Koepsell H. Subtype-specific affinity for corticosterone of rat organic cation transporters rOCT1 and rOCT2 depends on three amino acids within the substrate binding region. Mol Pharmacol 2005;67:1612-1619.

[128] Ramachandran S, Dokholyan N V. Homology modeling: generating structural models to understand protein function and mechanism. In: Springer, Boston, MA; 2012:97-116.

[129] Serohijos AWR, Hegedus T, Aleksandrov AA, He L, Cui L, Dokholyan N V., Riordan JR. Phenylalanine-508 mediates a cytoplasmic-membrane domain contact in the CFTR 3D structure crucial to assembly and channel function. Proc Natl Acad Sci 2008;105:3256-3261.

[130] Chothia C, Lesk AM. The relation between the divergence of sequence and structure in proteins. EMBO J 1986;5:823-826. http://www.ncbi.nlm.nih.gov/pubmed/3709526. Accessed July 14, 2018.

[131] Bioinformatics RC f. S. Protein Data Bank. www.rcsb.org/pdb/home. Accessed July 1, 2018.

[132] Vyas V, Ukawala R, Chintha C, Ghate M. Homology modeling a fast tool for drug discovery: Current perspectives. Indian J Pharm Sci 2012;74:1.

[133] Hilbert M, Böhm G, Jaenicke R. Structural relationships of homologous proteins as a fundamental principle in homology modeling. Proteins Struct Funct Genet 1993;17:138-151.

[134] Hillisch A, Pineda LF, Hilgenfeld R. Utility of homology models in the drug discovery process. Drug Discov Today 2004;9:659-669.

[135] Martí-Renom MA, Stuart AC, Fiser A, Sánchez R, Melo F, Šali A. Comparative Protein Structure Modeling of Genes and Genomes. Annu Rev Biophys Biomol

Struct 2000;29:291-325.

[136] Carlsson J, Coleman RG, Setola V, Irwin JJ, Fan H, Schlessinger A, Sali A, Roth BL, Shoichet BK. Ligand discovery from a dopamine D3 receptor homology model and crystal structure. Nat Chem Biol 2011;7:769-778.

[137] Schlessinger A, Matsson P, Shima JE, Pieper U, Yee SW, Kelly L, Apeltsin L, Stroud RM, Ferrin TE, Giacomini KM, Sali A. Comparison of human solute carriers. Protein Sci 2010;19:NA-NA.

[138] Dublin U. ClustalX. www.clustal.org/clustal2. Accessed July 1, 2018.

[139] Sali A. MODELLER. 2016.

[140] Laskowski RA, MacArthur MW, Moss DS, Thornton JM, IUCr. PROCHECK: a program to check the stereochemical quality of protein structures. J Appl Crystallogr 1993;26:283-291.

[141] Shen M, Sali A. Statistical potential for assessment and prediction of protein structures. Protein Sci 2006;15:2507-2524.

[142] Schlessinger A, Yee SW, Sali A, Giacomini KM. SLC Classification: An Update. Clin Pharmacol Ther 2013;94:19-23.

[143] Popp C, Gorboulev V, Müller TD, Gorbunov D, Shatskaya N, Koepsell H. Amino acids critical for substrate affinity of rat organic cation transporter 1 line the substrate binding region in a model derived from the tertiary structure of lactose permease. Mol Pharmacol 2005;67:1600-1611.

[144] Sturm A, Gorboulev V, Gorbunov D, Keller T, Volk C, Schmitt BM, Schlachtbauer P, Ciarimboli G, Koepsell H. Identification of cysteines in rat organic cation transporters rOCT1 (C322, C451) and rOCT2 (C451) critical for transport activity and substrate affinity. Am J Physiol Renal Physiol 2007;293:F767-79.

[145] Zhang X, Shirahatti N V, Mahadevan D, Wright SH. A conserved glutamate residue in transmembrane helix 10 influences substrate specificity of rabbit OCT2 (SLC22A2). J Biol Chem 2005;280:34813-34822.

[146] Pelis RM, Zhang X, Dangprapai Y, Wright SH. Cysteine accessibility in the hydrophilic cleft of human organic cation transporter 2. J Biol Chem 2006;281:35272-35280.

[147] Huang Y, Lemieux MJ, Song J, Auer M, Wang D-N. Structure and Mechanism of the Glycerol-3-Phosphate Transporter from Escherichia coli. Science (80-) 2003;301:616-620.

[148] Sturm A, Gorboulev V, Gorbunov D, Keller T, Volk C, Schmitt BM, Schlachtbauer P, Ciarimboli G, Koepsell H. Identification of cysteines in rat organic cation transporters rOCT1 (C322, C451) and rOCT2 (C451) critical for transport activity and substrate affinity. Am J Physiol Physiol 2007;293:F767-F779.

[149] Pedersen BP, Kumar H, Waight AB, Risenmay AJ, Roe-Zurz Z, Chau BH,

Schlessinger A, Bonomi M, Harries W, Sali A, Johri AK, Stroud RM. Crystal structure of a eukaryotic phosphate transporter. Nature 2013;496:533-536.

[150] Yadav V, Kumar M, Deep DK, Kumar H, Sharma R, Tripathi T, Tuteja N, Saxena AK, Johri AK. A phosphate transporter from the root endophytic fungus Piriformospora indica plays a role in phosphate transport to the host plant. J Biol Chem 2010;285:26532-26544.

[151] Abramson J, Smirnova I, Kasho V, Verner G, Kaback HR, Iwata S. Structure and mechanism of the lactose permease of Escherichia coli. Science (80-) 2003;301:610-615.

[152] Sweet DH. Renal organic cation and anion transport. In: *From Physiology to Genes*. 2nd ed. Oxford: Academic Press; 2010:23-53.

[153] Zhang X, Shirahatti N V., Mahadevan D, Wright SH. A conserved glutamate residue in transmembrane helix 10 influences substrate specificity of rabbit OCT2 (SLC22A2). J Biol Chem 2005;280:34813-34822.

[154] Quaigen T. QIAprep ® Miniprep Handbook For Purification of Molecular Biology Grade DNA Sample & Assay Technologies.; 2015.

[155] UniProt Database. www.uniprot.org. Published 2018. Accessed July 1, 2018.

[156] VanWert AL, Sweet DH. Impaired clearance of methotrexate in organic anion transporter 3 (Slc22a8) knockout mice: A gender specific impact of reduced folates. Pharm Res 2008;25:453-462.

[157] Bordo D, Argos P. Suggestions for safe residue substitutions in site-directed mutagenesis. J Mol Biol 1991;217:721-729.

[158] Koepsell H, Lips K, Volk C. Polyspecific Organic Cation Transporters: Structure, Function, Physiological Roles, and Biopharmaceutical Implications. Pharm Res 2007;24:1227-1251.

[159] Sweet DH, Miller DS, Pritchard JB. Basolateral localization of organic cation transporter 2 in intact renal proximal tubules. Am J Physiol Physiol 2000;279:F826-F834.

[160] Sweet DH, Miller DS, Pritchard JB. Localization of an organic anion transporter-GFP fusion construct (rROAT1-GFP) in intact proximal tubules. Am J Physiol 1999;276:F864-73. www.physiology.org/journal/ajprenal. Accessed July 25, 2018.

[161] Tzvetkov M V., Matthaei J, Pojar S, Faltraco F, Vogler S, Prukop T, Seitz T, Brockmöller J. Increased systemic exposure and stronger cardiovascular and metabolic adverse reactions to fenoterol in individuals with heritable OCT1 deficiency. Clin Pharmacol Ther 2018;103:868-878.

[162] Stamer UM, Musshoff F, Stüber F, Brockmöller J, Steffens M, Tzvetkov M V. Loss-of-function polymorphisms in the organic cation transporter OCT1 are associated with reduced postoperative tramadol consumption. Pain 2016;157:2467-2475.

[163] Zamek-Gliszczynski MJ, Giacomini KM, Zhang L. Emerging clinical importance of hepatic organic cation transporter 1 (OCT1) in drug pharmacokinetics, dynamics, pharmacogenetic variability, and drug interactions. Clin Pharmacol Ther 2018;103:758-760.

[164] Liu H. 2017.Three dimensional homology modeling of organic cation transporter 3 to identify structural elements mediating transport-substrate interactions. PhD Dissertation, Virginia Commonwealth University, Richmond, Virginia.

VITA

Raymond Eugene Lai was born on October 27, 1986 in Fairfax, Virginia and currently resides in Richmond, Virginia. He received his Bachelor of Science degree in Biology from the College of William and Mary, Williamsburg, Virginia, in 2009, Master of Science degree in Biology and Doctorate in Pharmacy from Virginia Commonwealth University, Richmond, Virginia, in 2011 and 2015, respectively.

PUBLICATIONS & CONFERENCE ABSTRACTS

1. **Raymond E. Lai**, Christopher E. Jay, Douglas H. Sweet. Organic solute carrier 22 (SLC22) family: Potential for interactions with food, herbal/dietary supplements, endogenous compounds, and drugs. 2018. *Journal of Food and Drug Analysis*. 2: S45-S60

2. **Raymond E. Lai**, Philip D. Mosier, Douglas H. Sweet. Elucidation of Substrate-Binding Interactions Within Human Organic Cation Transporters 2 (SLC22A2) Through Homology Modeling. AAPS Annual Meeting, San Diego, CA (Fall 2017)

3. Xiaolei Pan, **Raymond E. Lai**, Richard A. Glennon, Douglas H. Sweet. Potent Inhibition of human Organic Cation Transporters 1,2, and 3 by Synthetic Cathinones. AAPS Annual Meeting, San Antonio, TX. (Spring 2014)

4. **Raymond E. Lai**, Mi Jung Lim, David Goffman, Mary Bradbury. Alternative Agents for Phentolamine (OraVerse). Fairfax Pharmacy Update Newsletter, December 2014.

5. **Raymond E. Lai**, Xiaolei Pan, Rajesh Karunturi, Umesh R. Desai, Douglas H. Sweet. Inhibition of Human Organic Anion Transporter Function by Sulfated Non-Saccharide Glycosaminoglycan Mimetics. VCU Research and Career Day, Richmond, VA (Fall 2013)

6. **Raymond E. Lai**, Aditi Mulgaonkar, Douglas H. Sweet. Organic Cation Transporter 3 as a Potential Mediator of Renal Aminoglycoside Toxicity. VCU Research and Career Day, Richmond, VA. (Fall 2012)

7. Thomas J. Flynn, Martine S. Fergusan, **Raymond E. Lai**. Interactive Effects of Sex Hormones and Pro-Inflammatory Cytokines on Cultured Human Hepatocytes. FDA CFSAN Meeting, White Oak, MD (Summer 2008)

HONORS AND AWARDS

AAPS Workshop on Drug Transporters in ADME Poster Podium Winner	Spring 2018
AAPS Workshop on Drug Transporters in ADME Travel Grant	Spring 2018
VCU Graduate School Travel Grant	Fall 2017
Joseph P. Schwartz Award for scholarship, research, and service	Fall 2017
VCU Research and Career Day Best Poster- Runner up	Fall 2017
Charles T. Rector & Thomas W. Rorrer Graduate Travel Scholarship	Fall 2017
VCU School of Pharmacy Scholarship	Spring 2015
VCU School of Pharmacy Professionalism Award Nominee	Spring 2014
VCU School of Pharmacy Scholarship	Spring 2014
VCU PharmD/PhD Summer Fellowship	Summer 2013
Phi Lambda Sigma- Beta Nu Chapter Member Inductee	Spring 2013
VCU PharmD/PhD Summer Fellowship	Summer 2012